

# ELECTRICAL IMAGING FOR GEOHAZARD AND ENVIRONMENTAL MONITORING

GUEST Editors: VINCENZO LAPENNA, SABATINO PISCITELLI, AND PANTELIS SOUPIOS



---



# **Electrical Imaging for Geohazard and Environmental Monitoring**

International Journal of Geophysics

---

## **Electrical Imaging for Geohazard and Environmental Monitoring**

Guest Editors: Vincenzo Lapenna, Sabatino Piscitelli, and Pantelis Soupios



---

Copyright © 2012 Hindawi Publishing Corporation. All rights reserved.

This is a special issue published in "International Journal of Geophysics." All articles are open access articles distributed under the Creative Commons Attribution License, which permits unrestricted use, distribution, and reproduction in any medium, provided the original work is properly cited.

## **Editorial Board**

Jean-Pierre Burg, Switzerland  
John F. Cassidy, Canada  
Ping Chang, USA  
Yun-tai Chen, China  
S. Crampin, UK  
Robin Crockett, UK  
Jack Petrovich Dvorkin, USA  
Gary Egbert, USA

Marek Grad, Poland  
Hans-Gert Kahle, Switzerland  
Masao Kanamitsu, USA  
Shuichi Kodaira, Japan  
Zdenek Martinec, Czech Republic  
Philip Meredith, UK  
Steve Milan, UK  
C. Papazachos, Greece

Joerg Schleicher, Brazil  
Sheng-Rong Song, Taiwan  
P. Talwani, USA  
Rudolf A. Treumann, Germany  
Bjørn Ursin, Norway  
Petr Vaníček, Canada  
Michael S. Zhdanov, USA  
Sergej Zilitinkevich, Finland

## Contents

**Electrical Imaging for Geohazard and Environmental Monitoring**, Vincenzo Lapenna, Sabatino Piscitelli, and Pantelis Soupios  
Volume 2012, Article ID 786060, 1 page

**A Prototype System for Time-Lapse Electrical Resistivity Tomographies**, Raffaele Luongo, Angela Perrone, Sabatino Piscitelli, and Vincenzo Lapenna  
Volume 2012, Article ID 176895, 12 pages

**Geoelectrical Tomography as an Operative Tool for Emergency Management of Landslide: An Application in Basilicata Region, Italy**, G. Colangelo and A. Perrone  
Volume 2012, Article ID 593268, 5 pages

**Geoelectrical Surveys for Characterization of the Coastal Saltwater Intrusion in Metapontum Forest Reserve (Southern Italy)**, Antonio Satriani, Antonio Loperte, Vito Imbrenda, and Vincenzo Lapenna  
Volume 2012, Article ID 238478, 8 pages

**Geoelectrical Tomography Investigating and Modeling of Fractures Network around Bittit Spring (Middle Atlas, Morocco)**, Kh. Qarqori, M. Rouai, F. Moreau, G. Saracco, O. Dauteuil, D. Hermitte, M. Boualoul, and C. Le Carlier de Veslud  
Volume 2012, Article ID 489634, 13 pages

**Experimental Studies on the Changes in Resistivity and Its Anisotropy Using Electrical Resistivity Tomography**, Tao Zhu, Jian-Guo Zhou, and Jin-Qi Hao  
Volume 2012, Article ID 142069, 10 pages

## Editorial

# Electrical Imaging for Geohazard and Environmental Monitoring

Vincenzo Lapenna,<sup>1</sup> Sabatino Piscitelli,<sup>1</sup> and Pantelis Soupios<sup>2</sup>

<sup>1</sup> Institute of Methodologies for Environmental Analysis, National Research Council of Italy, 85050 Tito (PZ), Italy

<sup>2</sup> Department of Natural Resources and Environment, Technological Educational Institute of Crete (TEI), Crete, Greece

Correspondence should be addressed to Vincenzo Lapenna, lapenna@imaa.cnr.it

Received 13 February 2012; Accepted 13 February 2012

Copyright © 2012 Vincenzo Lapenna et al. This is an open access article distributed under the Creative Commons Attribution License, which permits unrestricted use, distribution, and reproduction in any medium, provided the original work is properly cited.

This special issue represents a contribute to disseminate the results of novel applications of the electrical resistivity imaging. Recently, innovative algorithms for tomographic data inversion and modern technologies for the field surveying have rapidly transformed the electrical imaging in a non-invasive, cost-effective, and powerful tool for geohazard and environmental monitoring. To date, the scientific interest for the electrical imaging is constantly growing and the novel approaches based on 3D and time-lapse 4D tomographic methods are disclosing the way for new and interesting applications, as well as the time-continuous mapping and monitoring of water content in a landslide body and the monitoring of weakly resistivity changes related to fluid migration processes close to seismic faults.

The papers published in this special issue mainly concern the study of hydrogeological problems typical of Mediterranean countries (i.e., landslide phenomena, saltwater intrusion) and the design of experiments for better evaluate the spatial and time-dependent changes of subsurface resistivity. Of course, these topics are not completely representative of all application fields of the electrical imaging.

In the paper of the special issue titled “*Geoelectrical tomography investigating and modeling of fractures network around Bittit spring (Middle Atlas, Morocco)*,” Qarqori and other coauthors describe the main results of a geoelectrical survey carried out for monitoring a strategic aquifer in the northern part of Morocco. The study gives a significant contribute for defining the water flow in karst environment and through subvertical fractures.

The paper by T. Zhu et al., titled “*Experimental studies on the changes in resistivity and its anisotropy using electrical*

*resistivity tomography*,” deals with laboratory estimation on electrical anisotropy using electrical resistivity tomography on dry magnetite samples under uniaxial pressure.

The paper by A. Satriani et al., “*Geoelectrical surveys for characterisation of the coastal salt water intrusion in Metapontum Forest Reserve (Southern Italy)*,” presents the results of a case study using resistivity imaging integrated with water and soil analysis to investigate salt water intrusion in a coastal aquifer, identifying large areas affected by intensive soil salinization, and delineating the saltwater intrusion front.

In the paper “*Geoelectrical tomography as an operative tool for emergency management of landslide: an application in Basilicata Region, Italy*,” G. Colangelo and A. Perrone describe an electrical imaging survey, integrated with borehole data, to study a complex rototranslational slide, showing how the application of this indirect technique could be particularly useful for end users involved in the landslide risk management.

Finally, the paper “*A prototype system for time-lapse electrical resistivity tomographies*” by Luongo et al. concerns the first experimental results obtained with a new system for time-lapse resistivity monitoring of a landslide. The system seems to be suitable for water content monitoring in shallow layers.

Vincenzo Lapenna  
Sabatino Piscitelli  
Pantelis Soupios

## Research Article

# A Prototype System for Time-Lapse Electrical Resistivity Tomographies

Raffaele Luongo,<sup>1,2</sup> Angela Perrone,<sup>2</sup> Sabatino Piscitelli,<sup>2</sup> and Vincenzo Lapenna<sup>2</sup>

<sup>1</sup>DIFA, Università della Basilicata, Contrado Macchia Romana, 85100 Potenza, Italy

<sup>2</sup>IMAA-CNR, Contrada Santa Loja Zona Industriale, Tito Scalo, 85055 Potenza, Italy

Correspondence should be addressed to Raffaele Luongo, raffaele.luongo@imaa.cnr.it

Received 11 July 2011; Accepted 24 December 2011

Academic Editor: Pantelis Soupios

Copyright © 2012 Raffaele Luongo et al. This is an open access article distributed under the Creative Commons Attribution License, which permits unrestricted use, distribution, and reproduction in any medium, provided the original work is properly cited.

A prototype system for time-lapse acquisition of 2D electrical resistivity tomography (ERT) and time domain reflectometry (TDR) measurements was installed in a test site affected by a landslide in Basilicata region (southern Italy). The aim of the system is to monitor in real-time the rainwater infiltration into the soil and obtain information about the variation of the water content in the first layers of the subsoil and the possible influence of this variation on landslide activity. A rain gauge placed in the test site gives information on the rainfall intensity and frequency and suggests the acquisition time interval. The installed system and the preliminary results are presented in this paper.

## 1. Introduction

Landslides are complex geological phenomena depending on many factors. In order to study these factors, to understand the triggering mechanisms of the movement, and to monitor its dynamic evolution it is necessary to apply a multidisciplinary approach. The rainwater infiltration into the soil and the increase of pore water pressure in the vadose zone can be considered one of the main causes of shallow landslides triggering. Usually, the standard techniques used to measure the water content of the soil and the water table levels in areas of potential instability are the TDR method and the piezometric measurements, respectively. These techniques, while allowing to obtain direct information of the considered parameter, provide only 1D information. Considering that landslides are volumetric phenomena it is a clear need to experiment new investigation techniques which can provide at least 2D hydrological information. It would be better if this information could be continuous in time.

Recently, the literature reports many examples of application of indirect (geophysical) methods for the study and the estimate of water content in the first layers of the subsoil. Among these, the electrical resistivity tomography (ERT), usually applied to obtain information about the geometrical features of the landslides and estimate the thickness of the

slide material [1–8], has been tested to obtain information on the temporal and spatial patterns of water infiltration processes [9–15].

The aim of this work is to present a prototype system planned to obtain time-lapse 2D ERT and TDR measurements in a landslide area located in Basilicata region (southern Italy). The system was planned with the aim to estimate the variation of electrical resistivity and soil moisture values in a long period and to obtain information about the influence of precipitations and seasonal changes on them. Very preliminary results allowed us to verify the functioning and confidence of the system, to decide the acquisition time interval, and to obtain information on the yearly variation of resistivity values.

The system was developed in the frame of MORFEO (Monitoraggio e Rischio da Frana mediante dati EO) project funded by the Italian Agency Space (ASI) and finalized to the activities of the Italian Civil Protection Department (DPC) in the landslide risk management.

## 2. Test Site Description

The planned monitoring system was installed in a landslide area located in Picerno territory at the western side of

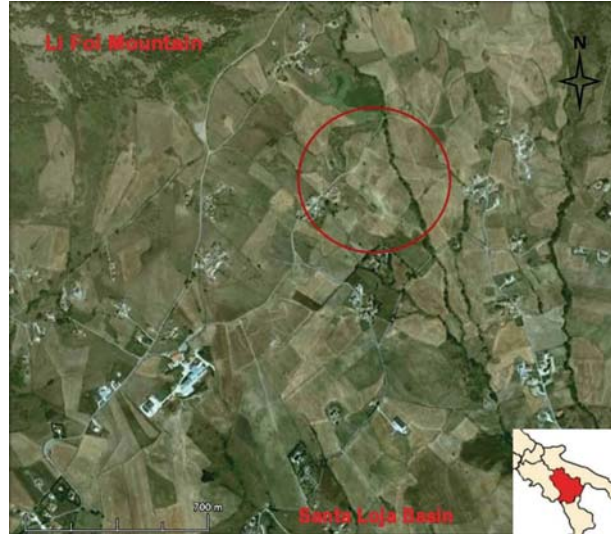


FIGURE 1: Study area location (from Google Earth, modified).

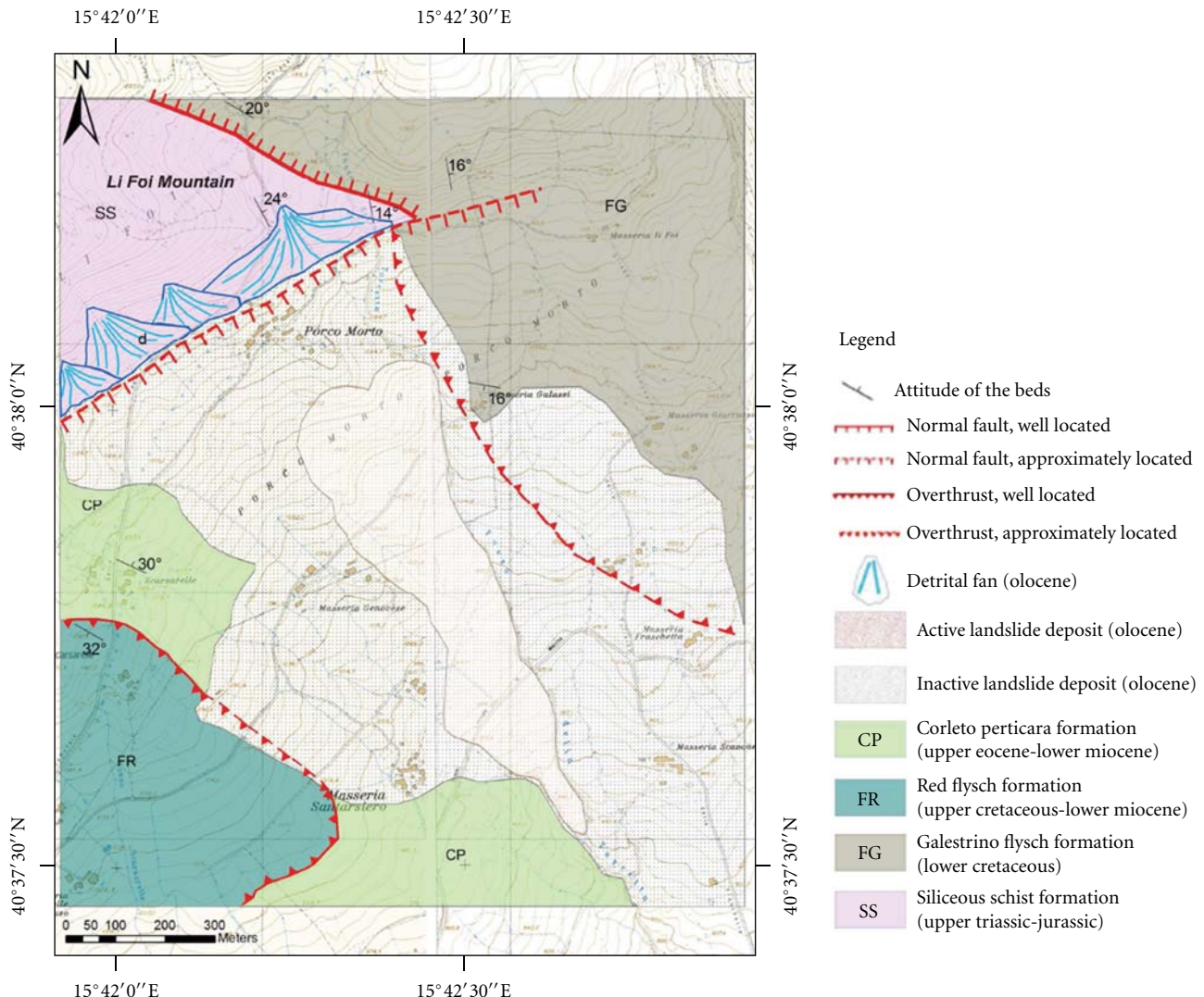


FIGURE 2: Geologic map of the area (from [1]).

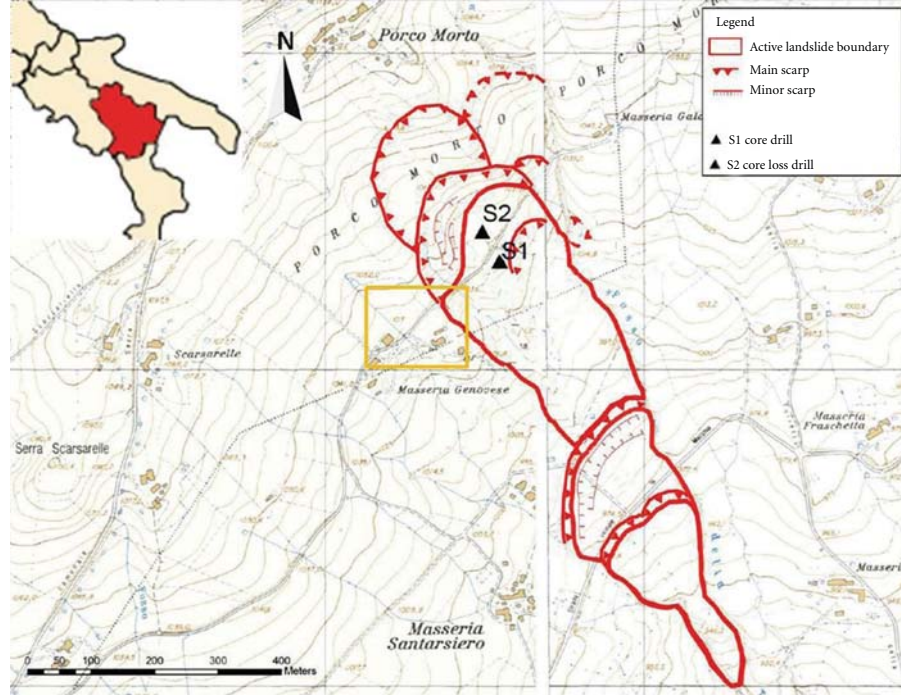


FIGURE 3: Geomorphologic map of the landslide (from [1] modified), yellow square includes the area where the system was installed.



FIGURE 4: Location of the acquisition profile (from Google Earth, modified).

Basilicata region (southern Italy), within the Apennine chain (Figure 1). The area has been frequently involved in reactivation phenomena, the most recent ones occurred on March 2006 after continuous and intense snowfalls.

Terrains affected by landslides belong to the Pignola, Abriola facies of the Lagonegro Unit. In particular, there are four main lithological formations outcropping on the slope that in order of sedimentation [16, 17] are (Figure 2):

- (i) Siliceous Schist (upper triassic-jurassic), outcropping along the slope of Mount LiFoi;
- (ii) Flysch Galestrino (lower cretaceous);
- (iii) Flysch Rosso (upper cretaceous-lower miocene);
- (iv) Corleto Perticara Formation (upper eocene-lower miocene).

The most recent terrains are characterized by the debris outcropping at the toe of Mount LiFoi.

The Siliceous Schist formation has a thick of 240 meters and is constituted by red and greenish shales with a typical rupture cleavage called “pencil cleavage.” In addition, there are red and green jaspers embedded with layers of radiolarites and flint. Lastly, manganese jaspers until they reach the Galestri formation.

The Flysch Galestrino formation is less thick than the Shist formation (about 200 m) and consists of alternating black claystones and siliceous marls, calcilutites and marly limestones, marls, and leaf clay.

The Flysch Rosso formation made of jasper, siliceous claystones, calcarenites, red and green marls is in eteropiec succession with Argille Varicolori and Corleto Perticara formations [18].

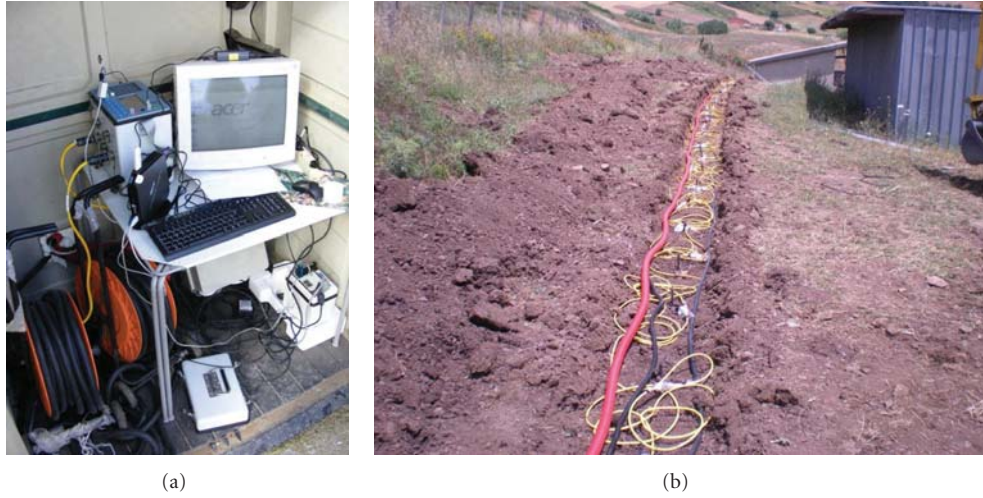


FIGURE 5: Systech Pro- and Mini-Trase equipment connect to the pc (a) and the 48-channel ERT monitoring system (b).

All lithological formations outcropping along the slope are in tectonic contact with each other. Therefore, the Siliceous Schist formation is in tectonic contact with the Flysch Galestrino and Corleto Perticara formations through normal faults which lowered the young ones in respect to the ancient.

The top of the slope in the study area is characterized by recent sedimentary debris due to a certain number of mass movements occurred in the last sixty years.

The landslide classified as a complex retrogressive rototranslational slide is 600 m long and 230 m wide with an altimetry range varying between 1072 m a.s.l., at the main crown, and 978 m a.s.l. at the toe (Figure 3).

The profile of measurement, placed in the upper part of the landslide close to its right lateral boundary, is 47 m long (Figure 4).

The investigation depth reached is about 8 m according to the hydrological characteristics of the area in which the maximum piezometric level is measured at 2 m from ground level.

### 3. Prototype System and Acquisition Procedure

The prototype system is composed of different units and was planned with the aim to monitor in real-time the electrical resistivity and soil moisture patterns in the first layer of the subsoil.

The two fundamental units of the system are the *geoelectrical monitoring system* and the *TDR system*.

The geoelectrical monitoring system consists of 48 steel electrodes and a 48-channel cable connected to a resistivimeter Systech Pro Switch 48 of the IRIS Instruments; the electrodes are buried in the soil at 0.5 meters depth, at the distance of 1 meter. The resistivimeter is linked to a pc used to store data and to manage the time when the acquisition starts, and the time interval between two consequential ones (Figure 5). The software used to control time-lapse acquisitions is Comsys Pro of the IRIS Instruments, operating by a script.

The TDR system is composed by 4 probes 20 cm length, buried at two different depths (1 m and 1.5 m) along the same profile of the geoelectric monitoring system. Two probes in correspondence of the 14th electrode and the other two in correspondence of 35th. All probes are connected to the Soil Moisture Equipment Corporation TRASE, which acquires and stores data. Also TDR system is connected to pc to be managed in remote control.

A weather station was installed in the area very close to the profile and linked to the pc. The station consists of a rain gauge to quantify the amount of rain falling in the area, a sensor to measure the air temperature and another one to determine speed and direction of the wind (Figure 6).

The electric current supply for the whole monitoring system is guaranteed by an uninterruptible power supply (U.P.S.).

The system was planned to be controlled in remote by an operator, who can decide day by day how to change acquisition parameters. After each acquisition the system sends an e-mail with attached the data file acquired to three different technicians involved in the check of the correct working of the system.

From September 2009 to January 2010, some ERTs were performed every week to test the system and its setting. For the acquisition three different electrode configuration were used: Wenner, Wenner-Schlumberger, and Dipole-Dipole, in order to choose the configuration that better emphasizes the features of the subsoil and the presence of the piezometric surface. At last, considering the better resolution of horizontal structures and the low noise recorded (better signal response), Wenner array was chosen. The system started to acquire and store data using “time-lapse” mode on 2 February 2010. At first, the number of acquisitions was fixed in four per day starting from 1.30 am (GMT + 1), with a time interval of 6 hours between two consecutive ones. This condition has lasted five months, till the end of June 2010. Then, the number of acquisitions was fixed in two per day, so



FIGURE 6: The weather station installed in the site.

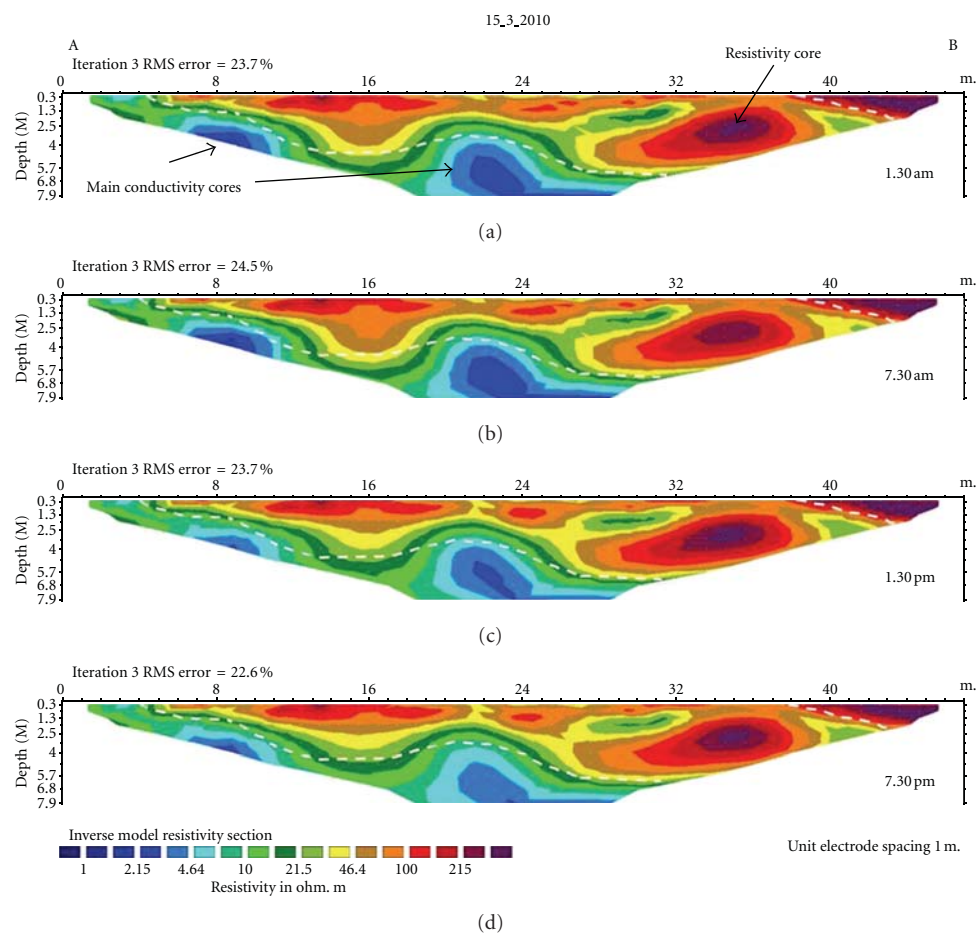


FIGURE 7: ERT related to the 15/03/2010 daily cycle of acquisition.

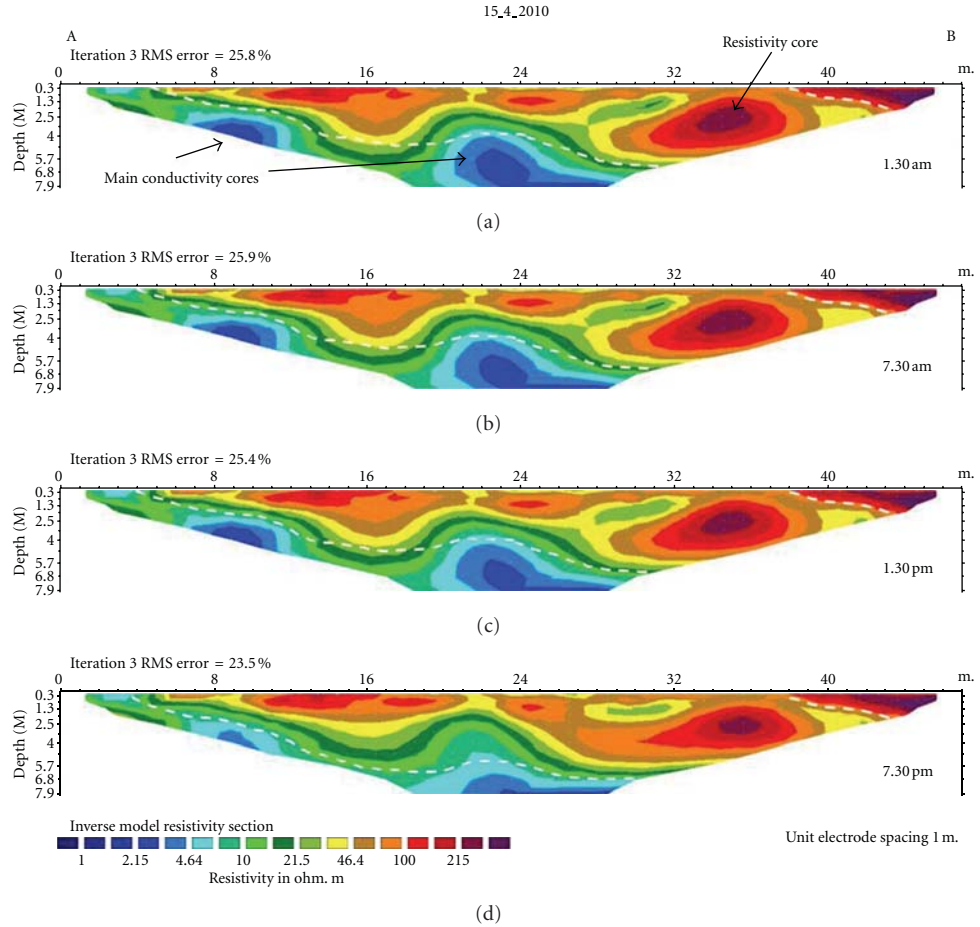


FIGURE 8: ERT related to the 15/04/2010 daily cycle of acquisition.

from 1th of July 2010 until now, system is acquiring with an interval of 12 hours, starting from 5 am (GMT + 1).

TDR acquisitions program is similar to the geoelectric one; it started with four acquisition per day, with a shift of one hour from the geoelectric survey. Then, from 1st of July 2010 it is acquiring soil moisture data at the same hour of geoelectric data, two times per day. Also for TDR survey it was decided to acquire with an interval of 12 hours, starting from 5 am (GMT + 1).

Weather station, instead, started to store data just from 2nd of February 2011, with interval of two hours. The number of acquisitions is 12 per day, so the amount of precipitations is extremely detailed. For the preliminary analysis we used the rainfall data acquired by another station located 3 kilometers far from the area of investigation.

#### 4. Preliminary Results

The results reported in this paper concern the first acquisition period from February 2010 to June 2010.

In the first five months, from the 2nd of February to the 30th of June, time-lapse tomographies were performed every days with a frequency of four acquisition per day. Exactly, the cycle of acquisition started 1.30 am (GMT+1) and ended

at 7.30 pm (GMT+1), with a time interval of 6 hours between two consecutive ones.

At the first, the system has been tested to verify its correct working. During February 2010 it was necessary to verify the correct functioning of the monitoring system in time-lapse mode and its stability in time. Hence, the main analysis of the resistivity data started from March 2010.

A preliminary analysis of the data has shown a considerable stability of the system and its correct working. No significant variations of the resistivity values were observed during a daily cycle of acquisition. This is also highlighted by the ERTs reported in Figures 7–10 showing the resistivity distribution in the subsoil of four daily cycles; more precisely acquisitions are referred to the 15th of March (Figure 7), the 15th of April (Figure 8), the 15th of May (Figure 9), and the 14th of June (Figure 10). Time interval between each acquisition is one month. The apparent resistivity data were inverted by using the RES2DINV software that uses an algorithm based on the smoothness constrained least square inversion implemented by using a quasi-Newton optimization technique, suggested by Loke and Barker [19].

All ERTs are characterized by the same distribution of resistivity and show a large range of values ( $2 < \rho < 300 \Omega\text{m}$ ), picked out by the presence of two main zones with different

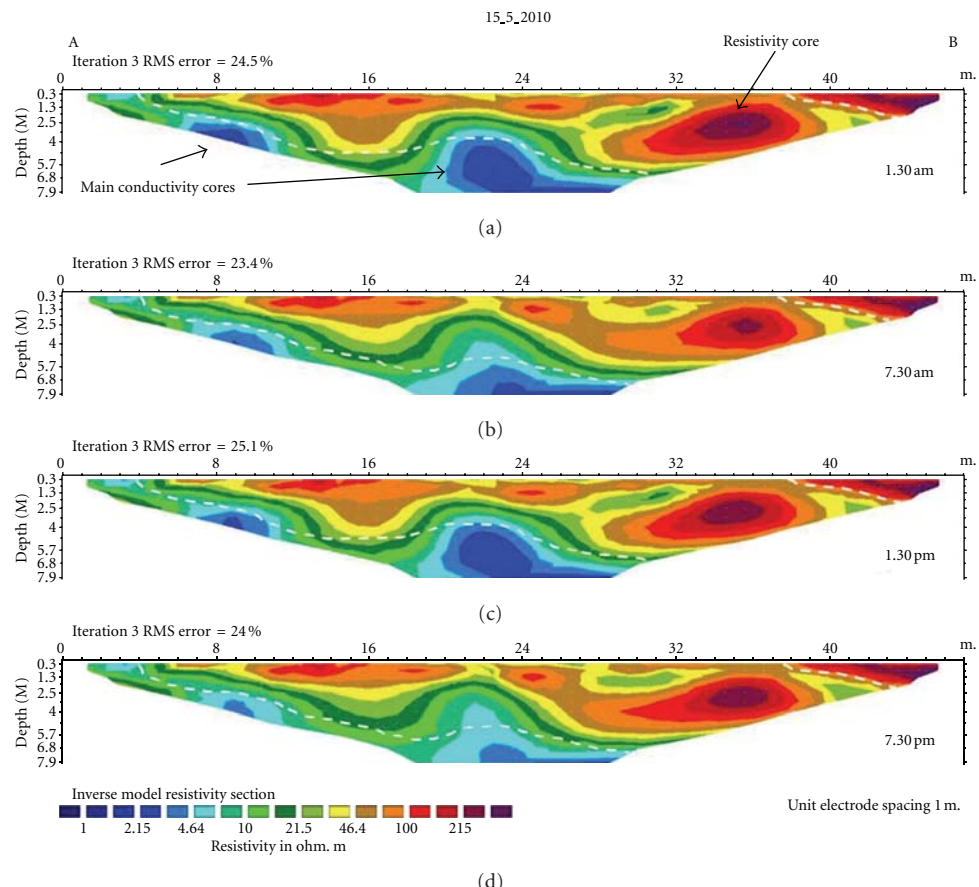


FIGURE 9: ERT related to the 15/05/2010 daily cycle of acquisition.

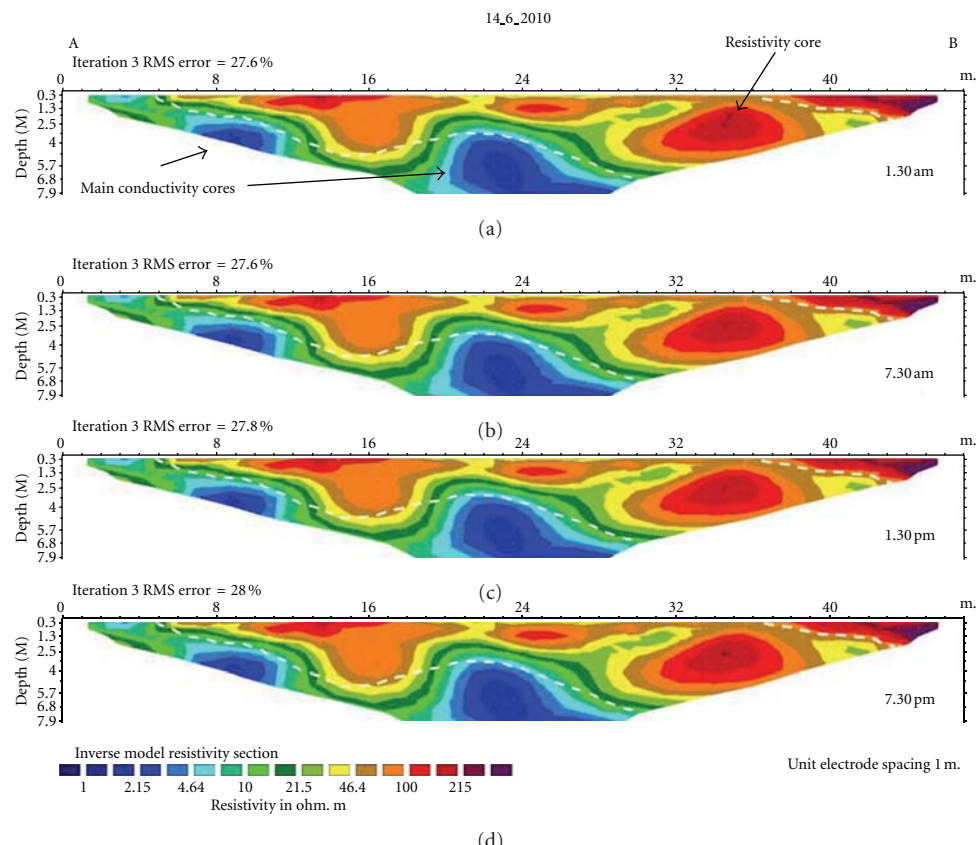


FIGURE 10: ERT related to the 14/06/2010 daily cycle of acquisition.

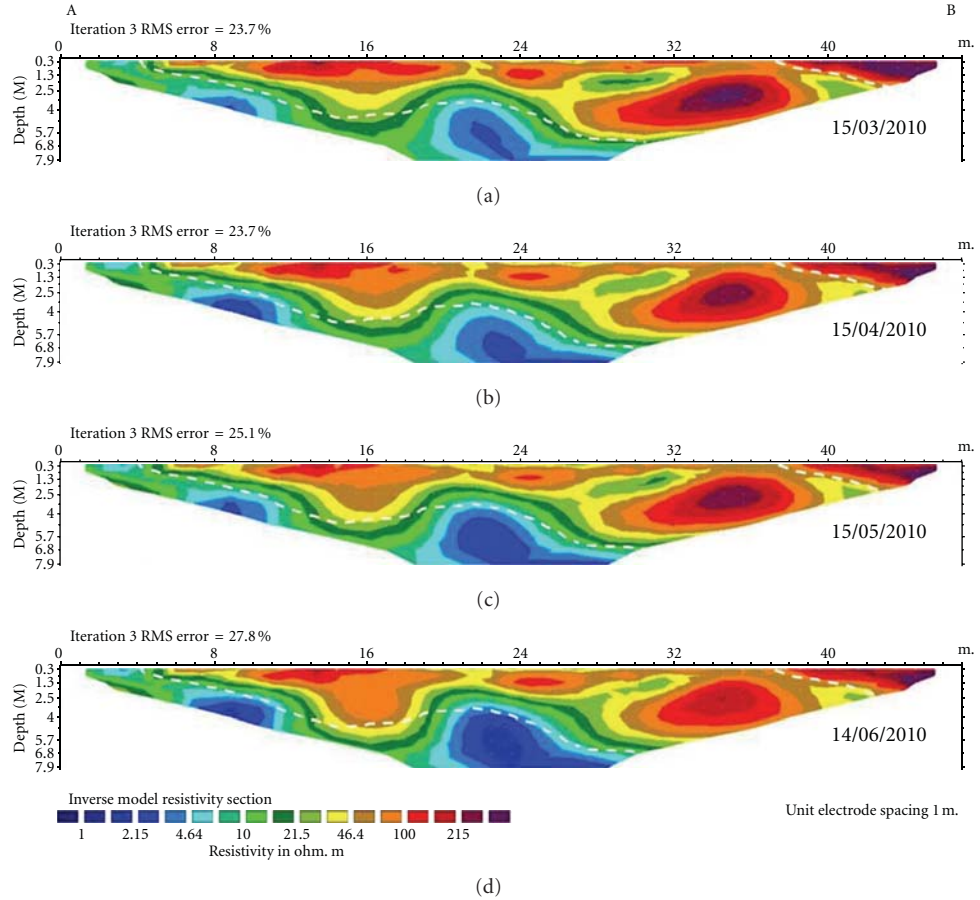


FIGURE 11: ERT performed in different days with an interval of one month; it is possible to observe the low change in resistivity during all the studied period.

resistivity values: a shallow zone, 2.5 m depth, with higher resistivity values ( $50 < \rho < 300 \Omega\text{m}$ ) distributed all along the profile, and a deeper one with the bulk of lower values ( $2 < \rho < 10 \Omega\text{m}$ ) concentrated in two main conductivity cores. A main central core with a thick of about 4 m and a smaller one in the left side of the tomographies, about 3 m deep. Moreover, by the extremity B of the tomography is evident a high conductivity layer, probably associated with the bedrock, while in the right side of the tomographies is present a large resistivity core.

Moreover, the low change in resistivity is also observed during the entire studied period (March 2010–June 2010). Figure 11 shows the comparison between the third acquisitions of each daily cycle: a general increase of conductivity in the central and right portions of the tomographies is evident, but the distribution of the resistivity values is similar for all the acquisitions.

In order to verify this resistivity distribution in the subsoil, a furthermore analysis was carried out to quantify the size of change ( $\Delta\rho$ ) during the entire period.

In particular, the resistivity differences between the first acquisition (15th of March 2010) and the last acquisition (14th of June 2010) have been calculated, with a time interval of four months. All analyses and pseudosections have been

performed by using the SURFER 8 of the Golden Software, Inc.

Variations has been calculated by (1) with respect to the acquisition of  $\rho_0$  at time  $T_0$  (15th of March 2010):

$$\Delta\rho = \frac{\rho_1 - \rho_0}{\rho_0}. \quad (1)$$

Figure 12 shows that the whole section is interested by negative resistivity differences, with values close to 0. This behavior seems to confirm that not important variations occurred during the entire period. Then, the same analysis was carried out in a shorter period, from the end of April 2010 ( $T_0 = 28/04/2010$ ) to the end of May 2010, interested by intense rainfall. This analysis has demonstrated that in a short period the resistivity changes are bigger and well distributed in the whole section (Figure 13).

Pseudosection of the differences shows a variation close to the zero in the shallow layers, except some small positive variations observed in the right side. The remaining portion of the pseudosection is affected by negative variations with a range included between 0 and  $-0.2 \Omega\text{m}$ , implying an unimportant increase of conductivity. Instead, resistivity differences calculated at  $T_2$  and  $T_3$  show an opposite behavior, with a more emphasized positive variation in the central core

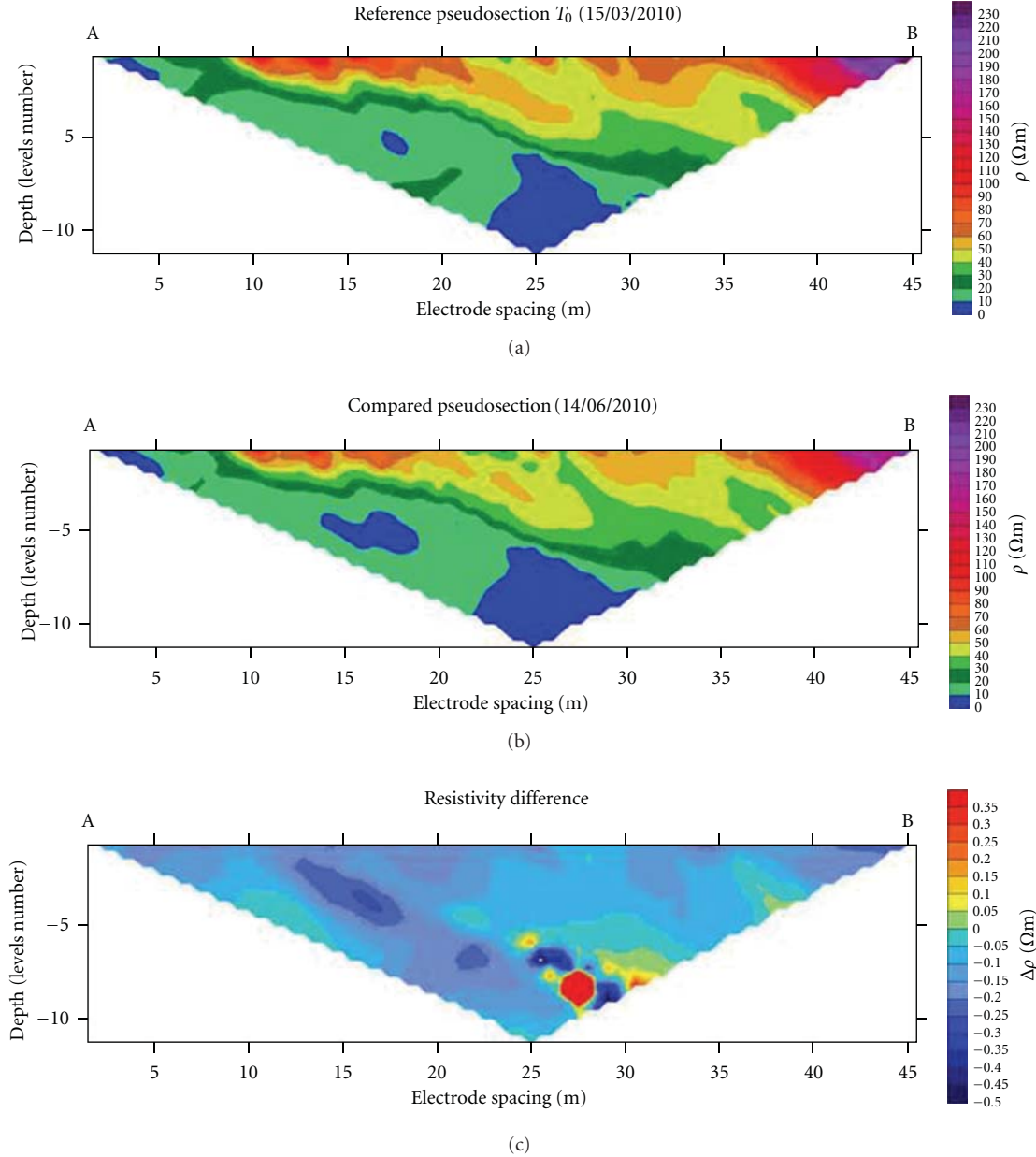


FIGURE 12: Resistivity differences calculated with respect to a fixed time  $T_0$  (15/03/2010). No important resistivity variations are observed.

of the pseudosections and negative variations in the shallow layers (Figure 13). Probably acquisition of 16th of May 2010 ( $T_2$ ) has been conditioned by the intense rainfall of two days before, explaining the shallow variation or resistivity. The electrical state of subsoil seems to remain the same also in the following day, as shown by the pseudo-section referred to the acquisition at time  $T_3$ ; even if not interested by rainfall, data acquired in the 27th of May 2010 has been probably conditioned by the distribution of rainfall occurred during the week before.

Whatever, starting from July 2010, the frequency of acquisition has been changed in order to emphasize the possible resistivity variations within a day.

## 5. Comparison between Soil Moisture and Resistivity

To verify if the resistivity variation is related to the variations of water content in the subsoil, the resistivity trend has been also compared to TDR data. In particular, resistivity and TDR data acquired at the same depth (1 m and 1.5 m) have been considered. In some cases, soil moisture has shown a behavior opposite to resistivity, confirming that resistivity variation in the subsoil is influenced by water content. To obtain a good agreement between resistivity and TDR data, acquisition frequency of TDR has been set as similar to the resistivity one, starting from 2 am (GMT + 1).

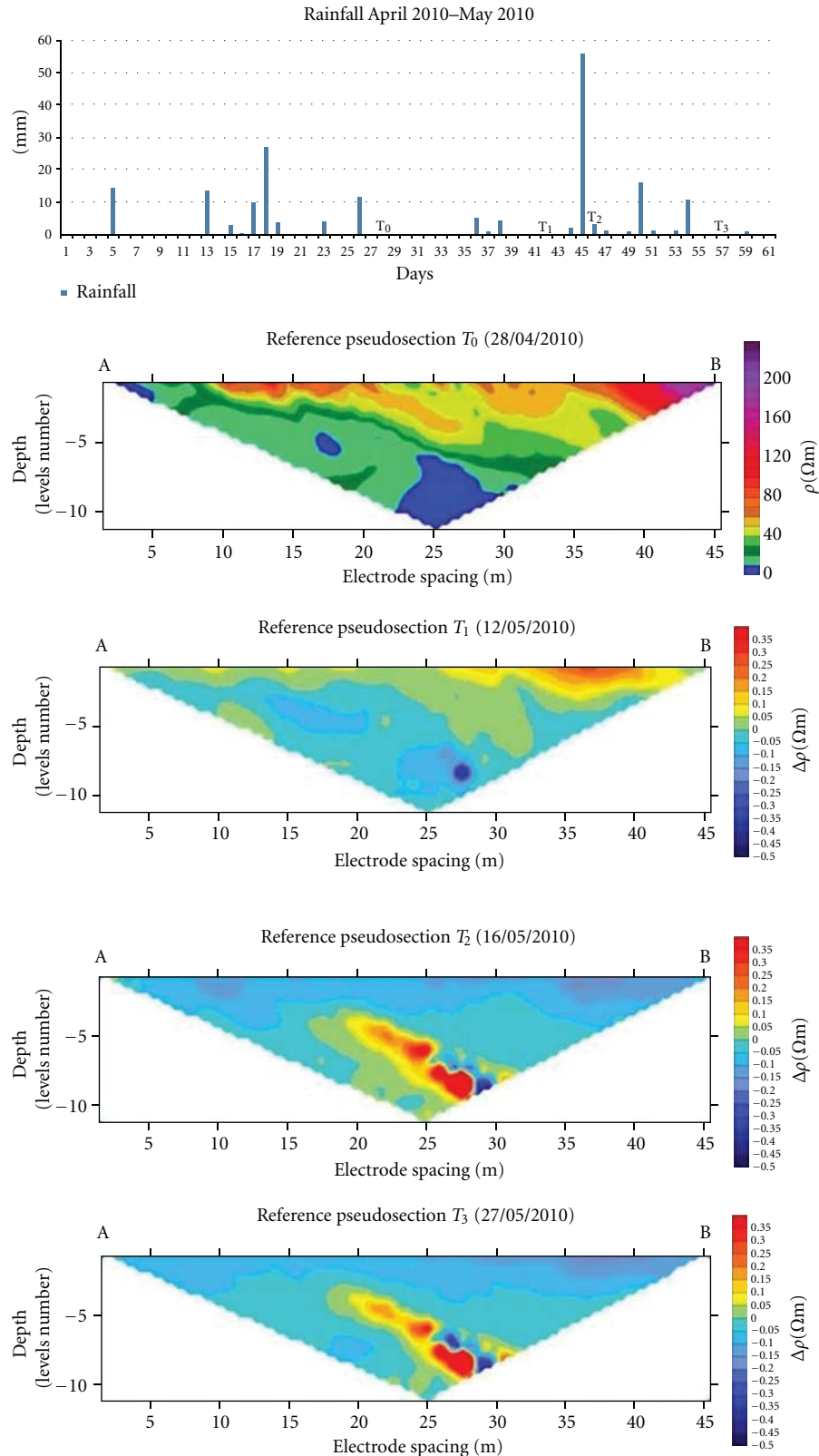


FIGURE 13: Resistivity differences calculated with respect to a fixed time  $T_0$  (28/04/2010). Differences are referred to three days of May 2010, chosen after intense rainfall.

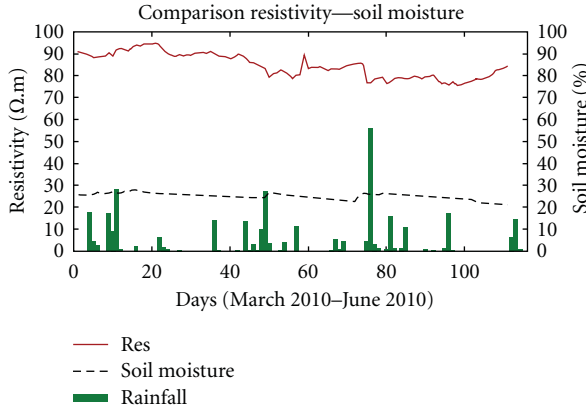


FIGURE 14: Comparison between Resistivity and TDR data acquired at 1 m depth, in correspondence of the 14 electrode.

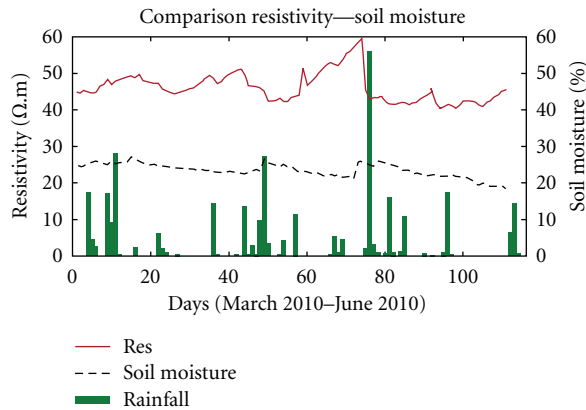


FIGURE 15: Comparison between Resistivity and TDR data acquired at 1 m depth, in correspondence of the 35 electrode.

Furthermore, also rainfall has been compared to TDR and resistivity, to understand how much the trend of the two parameters has been conditioned by it.

Figure 14 shows the comparison between resistivity and soil moisture values acquired at 1 m depth, equivalent to the 2nd level of the pseudo-section, in correspondence of the 14th electrode.

Fluctuations are present, interesting a range of values included between 75  $\Omega\text{m}$  and 91  $\Omega\text{m}$ . Instead, variations of soil moisture are smaller, included between 23% and 27%.

It is possible to observe that soil moisture and resistivity show a similar trend, even if in correspondence of some rain events an opposite behavior occurs. So it seems that the two parameters are not really conditioned by the rainfall during the four months, but just by intense spot precipitation periods.

Figure 15 is about the comparison between the two parameters acquired at 1 m depth, in correspondence of the 35th electrode. The trend of the two parameters is similar to the first example of Figure 13, but the opposite behavior of soil moisture with respect to the resistivity is more evident during the entire period.

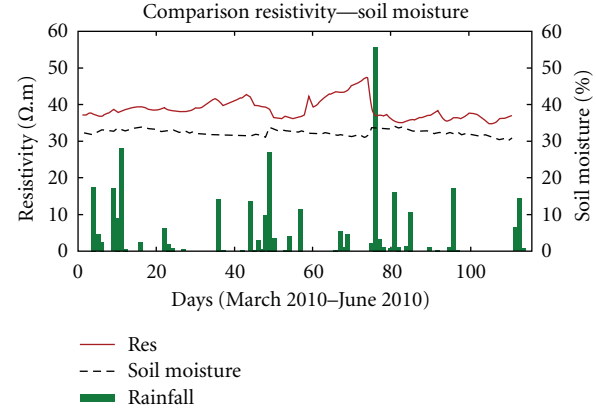


FIGURE 16: Comparison between Resistivity and TDR acquired at 1.5 m depth, in correspondence of the 35th electrode.

Also in this case the two parameters are not conditioned by rainfall during the four months but just in periods interested by intense rainfall.

The last case is about the comparison between two deeper points 1.5 m deep (3rd level of the calculated pseudosections), always in correspondence of the 35th electrode (Figure 16).

Range of resistivity is included between 38  $\Omega\text{m}$  and 50  $\Omega\text{m}$ , while soil moisture has a mean value of 30%. So, a general decrease of the resistivity values has been observed; at the same time, soil moisture percentage remains the same during the four months. A bigger number of events conditioned by the rainfall are highlighted. It has been observed that the two parameters evolve rapidly at the same time and that at this depth the variations of the two trends are more correlated than other shallower cases.

## 6. Conclusions

The prototype monitoring system has been developed in order to create a powerful tool to highlight the resistivity changes connected with the changes of water content in the first layers of the subsoil, within a landslide body. The real aim was to indirectly determine a preliminary estimate of the water content in an area affected by hydrogeological hazard.

Preliminary ERT have not shown great differences between the first and the last acquisition during the day, confirming the stability of the signal. Also the calculated resistivity differences between the first and the last acquisitions seem to confirm that resistivity is not subjected to big variation during the analyzed period, showing a negative distribution of values, close to 0. Instead, analysis in shorter period has demonstrated that the size of resistivity differences is bigger and well distributed in the whole subsoil section, perhaps conditioned by the intense rainfall period. Whatever, from the data trend analysis, the effect of precipitations is evident. TDR and resistivity trend comparison confirms that there is a decreasing of resistivity in correspondence of soil moisture growth, but this change seems to be stronger when intense precipitation periods occur.

Next step to confirm these preliminary results will be the statistical analysis of resistivity data along a period of 1 or 2 years, to understand if the fluctuation of values is strictly connected to the change of season. Besides, statistical results will be compared to the pluviometric data and to the soil moisture behavior, in order to obtain a more detailed description of the hydrogeological conditions of the area.

## References

- [1] C. De Baria, V. Lapenna, A. Perrone, C. Puglisi, and F. Sdao, “Digital photogrammetric analysis and electrical resistivity tomography for investigating the Picerno landslide (Basilicata region, southern Italy),” *Geomorphology*, vol. 133, no. 1-2, pp. 34–46, 2011.
- [2] V. A. Bogoslovsky and A. A. Ogilvy, “Geophysical methods for the investigation of landslides,” *Geophysics*, vol. 42, no. 3, pp. 562–571, 1977.
- [3] J. P. T. Caris and T. W. J. Van Asch, “Geophysical, geotechnical and hydrological investigations of a small landslide in the French Alps,” *Engineering Geology*, vol. 31, no. 3-4, pp. 249–276, 1991.
- [4] F. Ferrucci, M. Amelio, M. Sorriso-Valvo, and C. Tansi, “Seismic prospecting of a slope affected by deep-seated gravitational slope deformation: the Lago Sackung, Calabria, Italy,” *Engineering Geology*, vol. 57, no. 1-2, pp. 53–64, 2000.
- [5] V. Lapenna, P. Lorenzo, A. Perrone, S. Piscitelli, E. Rizzo, and F. Sdao, “2D electrical resistivity imaging of some complex landslides in the Lucanian Apennine chain, southern Italy,” *Geophysics*, vol. 70, no. 3, pp. B11–B18, 2005.
- [6] D. Jongmans and S. Garambois, “Geophysical investigation of landslides: a review,” *Bulletin de la Societe Geologique de France*, vol. 178, no. 2, pp. 101–112, 2007.
- [7] M. Pfaffhuber, S. Bastani, and M. Cornée, “Multi-method high resolution geophysical & geotechnical quick clay mapping A.A.” *Near Surface*. In press.
- [8] K. Sudha, M. Israel, S. Mittal, and J. Rai, “Soil characterization using electrical resistivity tomography and geotechnical investigations,” *Journal of Applied Geophysics*, vol. 67, no. 1, pp. 74–79, 2009.
- [9] D. Michot, Y. Benderitter, A. Dorigny, B. Nicoullaud, D. King, and A. Tabbagh, “Spatial and temporal monitoring of soil water content with an irrigated corn crop cover using surface electrical resistivity tomography,” *Water Resources Research*, vol. 39, no. 5, pp. SBH141–SBH1420, 2003.
- [10] D. H. Jayawickreme, R. L. van Dam, and D. W. Hyndman, “Subsurface imaging of vegetation, climate, and root-zone moisture interactions,” *Geophysical Research Letters*, vol. 35, no. 18, Article ID L18404, 5 pages, 2008.
- [11] R. De Franco, G. Biella, L. Tosi et al., “Monitoring the saltwater intrusion by time lapse electrical resistivity tomography: the Chioggia test site (Venice Lagoon, Italy),” *Journal of Applied Geophysics*, vol. 69, no. 3-4, pp. 117–130, 2009.
- [12] P. Brunet, R. Clément, and C. Bouvier, “Monitoring soil water content and deficit using electrical resistivity tomography (ERT)—a case study in the Cevennes area, France,” *Journal of Hydrology*, vol. 380, no. 1-2, pp. 146–153, 2010.
- [13] T. Arora and S. Ahmed, “Characterization of recharge through complex vadose zone of a granitic aquifer by time-lapse electrical resistivity tomography,” *Journal of Applied Geophysics*, vol. 73, no. 1, pp. 35–44, 2011.
- [14] J. Travelletti, P. Sailhac, J.-P. Malet, G. Grandjean, and J. Ponton, “Hydrological response of weathered clay-shale slopes: water infiltration monitoring with time-lapse electrical resistivity tomography,” *Hydrological Processes*. In press.
- [15] G. Cassiani, V. Bruno, A. Villa, N. Fusi, and A. M. Binley, “A saline trace test monitored via time-lapse surface electrical resistivity tomography,” *Journal of Applied Geophysics*, vol. 59, no. 3, pp. 244–259, 2006.
- [16] T. Pescatore, P. Renda, and M. Tramutoli, “Rapporti tra le unità lagonegresi e le unità Sicilidi nella media valle del Basento (Appennino lucano),” *Memoriali Società Geologica Italiana*, vol. 41, pp. 353–361, 1988.
- [17] S. Gallicchio, M. Marcucci, P. Pieri, I. Premoli Silva, L. Sabato, and G. Salvini, “Stratigraphical data from a Cretaceous claystones sequence of the “Argille Varicolori” in the Southern Apennines (Basilicata, Italy),” *Palaeopelagos*, vol. 6, pp. 261–272, 1996.
- [18] R. Sellii, “Il Paleogene nel quadro della geologia dell’Italia meridionale,” *Memorie della Società Geologica Italiana*, vol. 3, pp. 737–790, 1962.
- [19] M. H. Loke and R. D. Barker, “Rapid least-squares inversion of apparent resistivity pseudosections by a quasi-Newton method,” *Geophysical Prospecting*, vol. 44, no. 1, pp. 131–152, 1996.

## Research Article

# Geoelectrical Tomography as an Operative Tool for Emergency Management of Landslide: An Application in Basilicata Region, Italy

G. Colangelo<sup>1</sup> and A. Perrone<sup>2</sup>

<sup>1</sup>Department of Infrastructure and Civil Protection, Basilicata Region, C.so Garibaldi 139, 85100 Potenza, Italy

<sup>2</sup>Institute of Methodologies for Environmental Analysis, CNR, C.da S. Loja, 85050 Tito Scalo, Italy

Correspondence should be addressed to G. Colangelo, gerardo.colangelo@regione.basilicata.it

Received 18 July 2011; Revised 7 November 2011; Accepted 10 January 2012

Academic Editor: Sabatino Piscitelli

Copyright © 2012 G. Colangelo and A. Perrone. This is an open access article distributed under the Creative Commons Attribution License, which permits unrestricted use, distribution, and reproduction in any medium, provided the original work is properly cited.

During the landslide emergency many kinds of data, even if preliminary, can help to better understand the complexity of the investigated phenomenon and to give a valid contribution to the successive damage valuation. The electrical resistivity tomography (ERT) method was applied for investigating the deep characteristics of a landslide body that occurred in March 2006 close to Potenza town in Basilicata region (southern Italy): the landslide slid on a road near some farmers' houses which had to be evacuated. The information obtained by the application of this indirect technique appeared to be particularly useful for end users involved in the risk management. The high resolution of the 2D ERT technique allowed the detection of possible sliding surfaces and the characterization of high water content areas in which the increase of the saturation degree and of pore pressures could cause a weakening of the slopes and a reactivation of the movement. Due to the comparison between ERT results and stratigraphical data from boreholes carried out in the area it was possible to decide on the adoption of other evacuation decrees.

## 1. Introduction

The investigated area is located in Basilicata region, one of the southern Italian areas more involved in heavy meteorological conditions [1]. On March 2006, the intense precipitations have increased the saturation degree and the pore pressures of the terrains. The snow blanket has made heavy the slope changing the equilibrium of the strengths involved in the stability of a slope. These climatic conditions have deteriorated the physical and mechanic characteristics of the terrains outcropping in the region. As consequence of all these alterations, the reactivation of many dormant landslides, which affected the slopes of the region in the past, occurred. The main typologies of reactivation have been earth-flow, translational, or rotational slides.

The new slides have involved buildings and infrastructures on the slopes. The risk for people and assets needed the intervention of the end users involved in the risk management and, in particular, the inspection of Regional Department of Infrastructure and Civil Protection (RDICP).

In many involved areas and for many families evacuation decrees have been issued in order to ensure the safety of the people and allow the damage valuation. The study of such complex phenomena required a multidisciplinary approach based on the integration of all the direct and indirect data acquired in the area. An important contribution has been provided by the geophysical data and, in particular, by the 2D ERT that have been carried out in the areas affected by the reactivations some days after the landslide event.

The use of 2D ERT method for investigating landslides is now well tested. Many examples of the ERT application are reported in literature. In many cases the results of its application allowed to reconstruct the geometry of landslide body, to outline the sliding surface, and to locate areas characterized by high water content [2–7].

By using the Mobile Laboratory for chemical-physical and geophysical measurements of the Institute of Methodologies for Environmental Analysis (IMAA) of CNR, some ERTs have been performed in the more damaged areas of the Basilicata region (southern Italy). In particular, the present



FIGURE 1: Location of the study area in Basilicata region.

paper describes the test case of a complex rototranslational slide occurred close to Potenza town in the Picerno village territory during the winter of 2006.

Immediately after the event occurred two ERT, one with transversal direction and the other one with longitudinal direction to the landslide body, were performed in order to try to give an answer to some important questions for the RDICP like what are the geometrical characteristics of the landslide? How many houses and infrastructures could be involved in the evolution of the phenomena? Is it necessary to issue an evacuation decree for others families?

## 2. Geological Setting of the Landslide Area

The investigated area is characterized by the presence of a diffuse slope instability. On March 2006, due to the meteorological conditions, many reactivations occurred in the area like the one considered in this paper. In order to define the geological and geomorphological features of the area, aerial photogrammetric analysis and in-field observations have been performed.

From a geological point of view, Basilicata region is located along the axial zone of the southern Apennine chain that is mainly composed of sedimentary cover of platform and deep water environments, scraped off from the former Mesozoic Ligurian ocean, the western passive margin of the Adriatic plate, and the Neogene-Pleistocene foredeep deposits of the active margin. From west to east, the main Mesozoic domains are as follows: (1) the internal oceanic to transitional Liguride-Sicilide basinal domains (internal nappes), (2) the Apennine carbonate platform, (3) the Lagonegro-Molise basins, and (4) the Apulian carbonate platform [8].

The study area (Figure 1) is located in the west of the Basilicata region and on the southeastern slope of Li Foi Mountain (1355 m a.s.l.) near the S. Loja Basin along the axial zone of the Lucanian Apennine. The area is characterized by the outcropping of terrains belonging to the Pignola-Abriola facies (calcareous-silica-marly series) of the Lagonegro Unit II [9]. This facies is composed of the Siliceous Schist (Upper Triassic-Jurassic), the Galestro Flysch (Lower Cretaceous), the Red Flysch (Upper Cretaceous-Lower Miocene), and the Corleto Perticara Formation

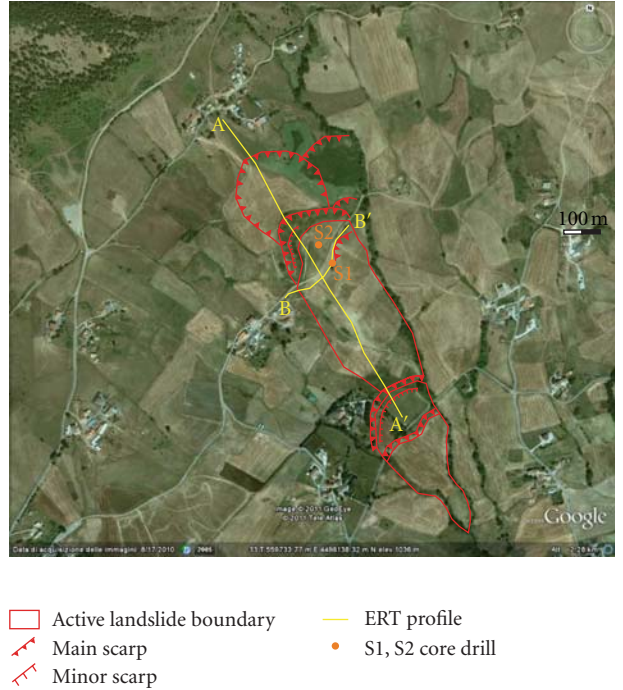


FIGURE 2: Geomorphological map of the area (aerial photo by Google Earth) with location of geophysical and geotechnical soundings.

(Upper Eocene-Lower Miocene) [10, 11]. The landslide occurred in 2006 involved the terrains belonging to the Corleto Perticara Formation mainly constituted by calcarenites, calcilutites, and whitish marly limestone.

From a geomorphological point of view the area is characterized by a moderate slope angle of 13–16% with an altimetry range varying between 1072 m a.s.l. at the main crown and 970 m a.s.l. at the toe. The landslide can be classified as a complex retrogressive rototranslational slide and is 600 m long and 230 m wide (Figure 2). Due to the movement, counter slope terraces filled with stagnant water formed. Transversal and radial cracks are still evident in the accumulation zone of the landslide that involved infrastructures and buildings some of whose had to be evacuated [12].

## 3. ERT and Analysis of the Results

ERT is a geoelectrical method widely applied to obtain 2D and 3D high-resolution images of the resistivity subsurface patterns in areas of complex geology [13]. During the field survey, ERT can be carried out by using different electrode configurations (dipole-dipole, Wenner, etc.) placed at the surface to send the electric currents into the ground and to measure the generated voltage signals. Technically, during an electrical resistivity measurement, the electric current is injected into the ground via two electrodes and the potential drop is measured between two other electrodes in line with current ones. The values of the apparent resistivity acquired along a horizontal axis are assigned at a defined depth and position. In a second step, it is necessary to transform

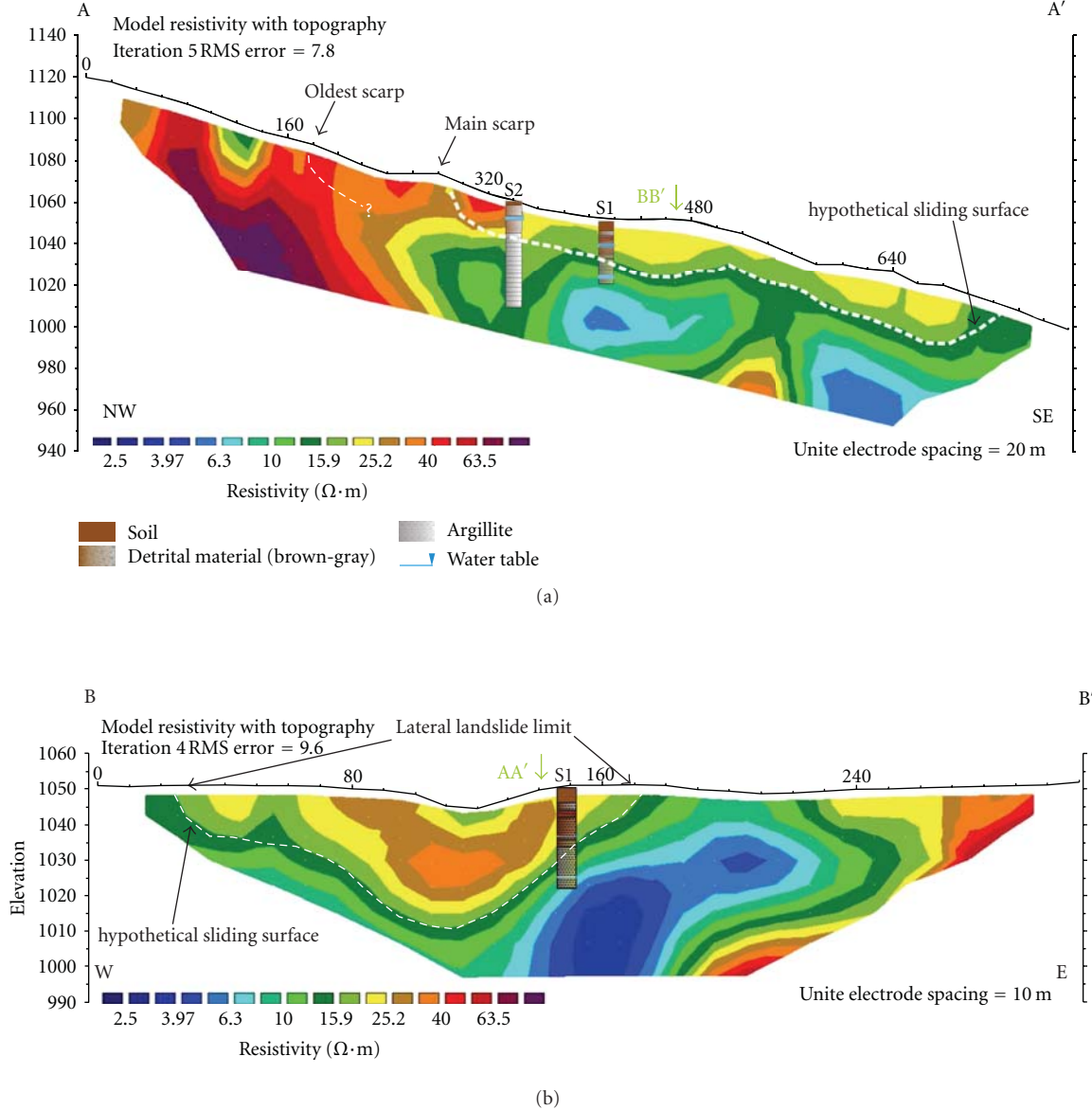


FIGURE 3: (a) Comparison between AA' ERT, carried out with longitudinal direction to the landslide body, and S1 and S2 stratigraphical data; (b) comparison between BB' ERT and S1 stratigraphical data. The horizontal resistivity contrast, highlighted with white dashed line in both the ERT, corresponds to the contact between detrital material (slide material) and argillite material.

the apparent resistivity values obtained during the field survey into real resistivities of the subsoil and the pseudodepths into true depths.

In this work, the algorithm proposed by Loke and Barker [14] for the automatic 2D inversion of apparent resistivity data was used. The inversion routine is based on the smoothness constrained least-squares inversion [15] implemented by a quasi-Newton optimisation technique. The subsurface is divided in rectangular blocks, whose number corresponds to the number of measurement points. The optimisation method adjusts the 2D resistivity model trying to reduce iteratively the difference between the calculated and measured apparent resistivity values. The root mean squared (RMS) error gives a measure of this difference.

The knowledge of local geology associated with the high spatial resolution of the measurements gives us an interpretative tool to explain the ERT obtained for the case study of this work.

ERTs have been carried out with direction longitudinal (AA') and transversal (BB') to the axis of the landslide (Figure 2) by using a multielectrode system with 32 electrodes and the dipole-dipole array. Both the ERTs were topographically correct in order to reduce possible mistakes and improve the interpretation of the model.

The longitudinal profile (length 780 m) was carried out by using an electrode spacing of 20 m, reaching an investigation depth of about 55–60 m. The AA' ERT (Figure 3(a)), obtained along this profile, is characterized

by a semivertical discontinuity, located at 280 m from the origin of the profile, which separates relatively high resistivity material ( $20 < \rho < 80 \Omega \cdot \text{m}$ ) from conductive one ( $4-20 \Omega \cdot \text{m}$ ). This discontinuity represents the main scarp of the landslide here investigated. The remainder of the ERT is characterized by a vertical resistivity variation with a first resistivity ( $20 < \rho < 50 \Omega \cdot \text{m}$ ) layer (about 25 m thick) which covered a more conductivity material ( $0 < \rho < 20 \Omega \cdot \text{m}$ ). The relatively high resistive layer could be associated with the slide material involved in the reactivation.

The high resistivity material characterizing the north-western side of the ERT highlights the presence of the bedrock. At a distance of 180 m from the origin of the profile it is also possible to see the presence of another vertical discontinuity that could be associated with the old scarp of a deep ancient landslide now totally eroded and not visible at the surface.

The transversal profile (length 320 m) has been carried out by using an electrode spacing of 10 m, reaching an investigation depth of about 45–50 m.

The BB' ERT (Figure 3(b)), obtained along this profile shows a first resistivity ( $20 < \rho < 50 \Omega \cdot \text{m}$ ) layer (about 30 thick), which covered a more conductivity material ( $0 < \rho < 20 \Omega \cdot \text{m}$ ). The contrast between conductive and resistive material could be associated with the presence of a sliding surface. The higher conductive nucleus ( $\rho < 10 \Omega \cdot \text{m}$ ), located at a distance ranging from 160 to 240 m from the origin of the profile, could be associated with an area characterized by high water content.

The ERTs were compared with stratigraphical data from direct boreholes (S1 and S2) carried out in the area by the RDICP (see Figure 2 for the location). In particular, the first 15–16 m of the S1 borehole (a 27 m deep core drilling) can be considered landslide material composed of detrital clay marl deposits with pebbles, interbedded with marly limestone. Below 16 m more consolidated clay can be found down to the bottom of the borehole. Two water tables are found in the S1 borehole at about 14 and 25 m, respectively [12].

The comparison between direct and indirect data (Figures 3(a) and 3(b)) allowed the better definition of the 2D landslide geometry and the correlation between resistivity values, reported in the ERT, and specific lithological characteristics of the slope. The comparison also made possible the detection of high water content areas for which the technicians of RDICP have planned and realized the first drainage works.

#### 4. Discussion and Conclusion

ERT technique was used for emergency management of a landslide that occurred in Basilicata Region close to Potenza town on March 2006. ERT has been applied with the aim to obtain information about the deep characteristics of the landslide body. In particular, two ERTs were carried out with longitudinal and transversal direction to the landslide body, respectively. The results, also compared with stratigraphical data, highlighted the presence of two layers with different resistivity. The sliding surface has been associated with

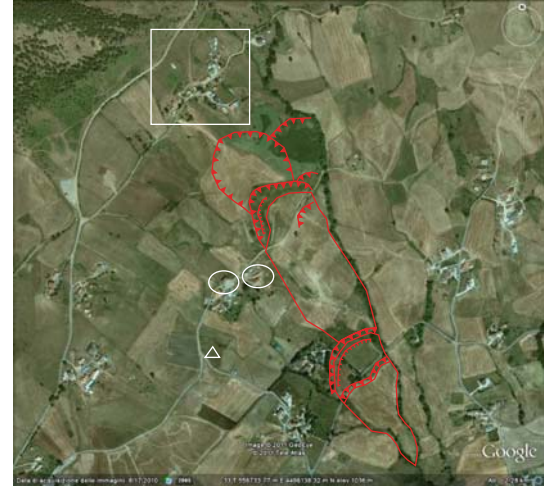


FIGURE 4: Aerial photo (modified by Google Earth) reporting the location of evacuated families (circles), temporary accommodation (triangle), warning area (square), and geotechnical instrumentations (stars).

the “layer” corresponding to resistivity contrast and area with high water content has been located. The information obtained by the application of this indirect technique appeared to be particularly useful for the end users involved in the risks management. Indeed, during the first phase of the emergency the main problem was the safety of the people and the relative evacuation of the area. In this case, the houses were principally concentrated on middle and upper part of the slope. RDICP technicians in collaboration with local administration had evacuated only the houses located in the middle part of the slope, in correspondence of the landslide body individuated on longitudinal and transversal ERT. A temporary accommodations for these families was found in a container located in a external part of the landslide (Figure 4).

Thanks to the longitudinal ERT, in which the bedrock was detected, it was possible to exclude the retrogressive evolution of the investigated phenomenon so, thanks to this information, to decide that it was not necessary to issue an evacuation decree for the families living in the upper part of the slope. In any case, geotechnical instrumentations (piezometers and inclinometers) and GPS markers were installed inside and outside of the landslide area in order to obtain additional information about the dynamic evolution of the gravitational movement affected the slope (Figure 4).

Moreover, the thickness of the landslide evaluated on both longitudinal and transversal ERTs at a depth of about 20–30 m, helped the RDICP to define the slope stabilization plan to adopt during the second phase of the emergency. Indeed, on landslide body only superficial diffuse drainage systems (Figure 5(a)) for the total length of the landslide and naturalistic engineering works to restore the local route (Figure 5(b)) were carried out and any deep works (networks of micropiles, piles, etc.) were realized.

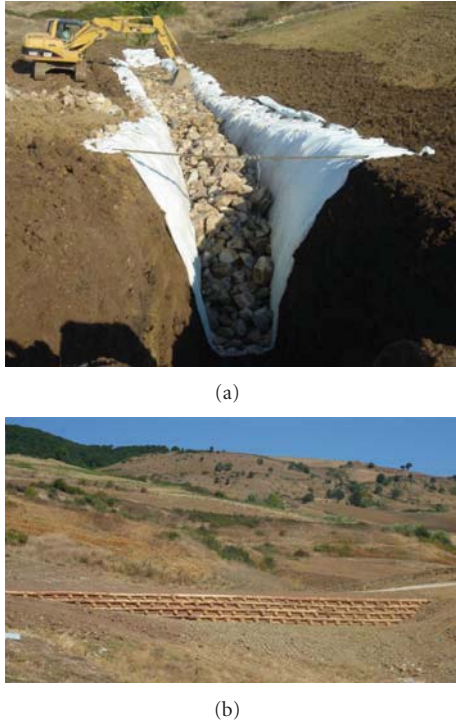


FIGURE 5: (a) Drainage systems effectuated during the second phase of the emergency with 4.0 m depth, and 1.2 km length; (b) Naturalistic engineering works using light and native material (chestnut tree and broom).

## Acknowledgment

Thanks are due to G. Calvello for the support during the project and Impresa Curcio of Picerno, Italy for the availability during the different phases of the work.

## References

- [1] Gli indicatori del clima in Italia nel 2005, I Anno, APAT, <http://www.sinanet.isprambiente.it/>.
- [2] A. Demoulin, A. Pissart, and C. Schroeder, "On the origin of late Quaternary paleolandslides in the Liege (E Belgium) area," *International Journal of Earth Sciences*, vol. 92, pp. 795–805, 2003.
- [3] A. Bichler, P. Bobrowsky, P. Best et al., "Three-dimensional mapping of a landslide using a multi-geophysical approach: the Quesnel Forks landslide," *Landslide*, vol. 1, pp. 29–40, 2004.
- [4] A. Perrone, A. Iannuzzi, V. Lapenna et al., "High-resolution electrical imaging of the Varco d'Izzo earthflow (southern Italy)," *Journal of Applied Geophysics*, vol. 56, no. 1, pp. 17–29, 2004.
- [5] V. Lapenna, P. Lorenzo, A. Perrone, S. Piscitelli, E. Rizzo, and F. Sdao, "2D electrical resistivity imaging of some complex landslides in the Lucanian Apennine chain, southern Italy," *Geophysics*, vol. 70, no. 3, pp. B11–B18, 2005.
- [6] O. Meric, S. Garambois, D. Jongmans, M. Wathelet, J. L. Chatelain, and J. M. Vengeon, "Application of geophysical methods for the investigation of the large gravitational mass movement of Séchilienne, France," *Canadian Geotechnical Journal*, vol. 42, no. 4, pp. 1105–1115, 2005.
- [7] A. Godio, C. Strobbia, and G. De Bacco, "Geophysical characterisation of a rockslide in an alpine region," *Engineering Geology*, vol. 83, no. 1-3, pp. 273–286, 2006.
- [8] D. Scrocca, E. Carminati, and C. Doglioni, "Deep structure of the southern Apennines, Italy: thin-skinned or thick-skinned?" *Tectonics*, vol. 24, no. 3, pp. 1–20, 2005.
- [9] P. Scandone, "Studi di geologia lucana: Carta dei terreni della serie calcareo-silicomarnosa e note illustrate," *Bollettino Società dei Naturalisti in Napoli*, vol. 81, pp. 225–300, 1972.
- [10] T. Pescatore, P. Renda, and M. Tramutoli, "Rapporti tra le unità lagonegresi e le unità Sicilidi nella media valle del Basento (Appennino lucano)," *Memoriali della Società Geologica Italiana*, vol. 41, pp. 353–361, 1988.
- [11] S. Gallicchio, M. Marcucci, P. Pieri, I. Premoli Silva, L. Sabato, and G. Salvini, "Stratigraphical data from a Cretaceous claystones sequence of the "Argille Varicolori" in the Southern Apennines (Basilicata, Italy)," *Palaeopelagos*, vol. 6, pp. 261–272, 1996.
- [12] C. de Bari, V. Lapenna, A. Perrone, C. Puglisi, and F. Sdao, "Digital photogrammetric analysis and electrical resistivity tomography for investigating the Picerno landslide (Basilicata region, southern Italy)," *Geomorphology*, vol. 133, no. 1-2, pp. 34–46, 2011.
- [13] D. H. Griffiths and R. D. Barker, "Two-dimensional resistivity imaging and modelling in areas of complex geology," *Journal of Applied Geophysics*, vol. 29, no. 3-4, pp. 211–226, 1993.
- [14] M. H. Loke and R. D. Barker, "Rapid least-squares inversion of apparent resistivity pseudosections by a quasi-Newton method," *Geophysical Prospecting*, vol. 44, no. 1, pp. 131–152, 1996.
- [15] Y. Sasaki, "Resolution of resistivity tomography inferred from numerical simulation," *Geophysical Prospecting*, vol. 40, no. 4, pp. 453–463, 1992.

## Research Article

# Geoelectrical Surveys for Characterization of the Coastal Saltwater Intrusion in Metapontum Forest Reserve (Southern Italy)

**Antonio Satriani, Antonio Loperte, Vito Imbrenda, and Vincenzo Lapenna**

*Institute of Methodologies for Environmental Analysis, CNR, 85050 Tito, Italy*

Correspondence should be addressed to Antonio Satriani, satriani@imaa.cnr.it

Received 25 May 2011; Revised 2 November 2011; Accepted 29 November 2011

Academic Editor: Sabatino Piscitelli

Copyright © 2012 Antonio Satriani et al. This is an open access article distributed under the Creative Commons Attribution License, which permits unrestricted use, distribution, and reproduction in any medium, provided the original work is properly cited.

A geoelectrical survey was carried out in the Metapontum Forest Reserve located along the Ionian coast of the Basilicata region (Southern Italy). In this work we used the method of two-dimensional electrical resistivity tomography for obtaining high-resolution electrical images in the investigated site. In particular, three electrical resistivity tomography, all orthogonal to the coastline, in the investigated area were carried out. To complete and integrate the geophysical data, soil and groundwater samplings, seventeen and five, respectively, were analyzed using chemical physical techniques. Geoelectrical survey, supported by laboratory analysis of soil and water samples have revealed the presence of a process of saltwater in coastal Forest Reserve of Metapontum, which have caused the decline of the existing pine forest with the consequent erosion and desertification problems. The results have disclosed the way to identify and discriminate large areas affected by intensive soil salinization and high resolution electrical images of the subsurface electrical resistivity plays a key role in delineating the saltwater intrusion front in coastal areas. Furthermore, our integrated study represents a contribution to the future programs for the protection, planning, and management of the terrestrial and marine resources in this coastal area.

## 1. Introduction

Coastal areas are of great environmental, economic, social, and cultural relevance. Therefore, the implementation of suitable monitoring and protection actions is fundamental for their preservation and for assuring future use of this resource. Such actions have to be based on an ecosystem perspective for preserving coastal environment integrity and functioning and for planning sustainable resource management of both marine and terrestrial components (EU Recommendation on Integrated Coastal Zone Management—ICZM—European Commission EC/413/2002).

Post [1] has defined coastal aquifers as the subsurface equivalents of coastal areas where continental fresh groundwater and seawater meet. Coastal plains are often contaminated by salt waters and the process associated to the marine water entering an aquifer is generally called seawater intrusion. Different approaches have been adopted to esti-

mate seawater intrusion. For example, many authors [2–5] have employed geochemical methods based on measures of electrical conductivity, of chloride concentration, and other cation and anion concentrations, parameters which generally highlight seawater contamination.

Nowadays great attention is focused on innovative geophysical methods for solving hydrogeological and environmental problems [6–10]. The geophysical methods for the subsurface exploration can contribute to the different phases of coastal environment characterization. Balia et al. [11] have applied a combination of geophysical techniques at the Muravera plain in southern Sardinia, Italy, which has been significantly affected by water salinization; Batayneh [12] used electrical resistivity methods for detecting subsurface fresh and saline water in the eastern Dead Sea coastal aquifers in Jordan; Bauer et al. [13] applied electrical resistivity tomography (ERT) to map the salinity distribution in the subsurface in the Okavango Delta, a large inland delta in

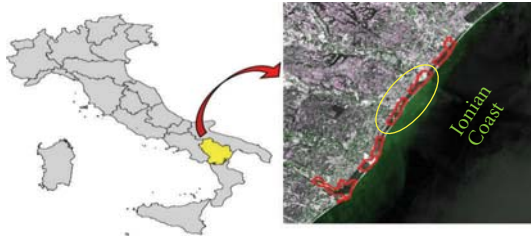


FIGURE 1: Location of the study area. The yellow ellipse highlights the natural reserve of Metapontum.

Botswana; while Koukadaki et al. [14] characterized the hydrogeology of a coastal aquifer using geophysical measurements and, in particular, electrical tomography. ERT, moreover, was applied to monitor seawater intrusion by Kruse et al. [15], Nowroozi et al. [16], Abdul Nassir et al. [17], and Sherif et al. [18]. Cimino et al. [19] carried out vertical electrical sounding in the coastal plain of Acquedolci (Northern Sicily- Italy) to assess seawater intrusion, while Khalil [20] applied a direct current resistivity geoelectric technique to delineate salt water intrusion from the Gulf of Suez. Moreover, Urich and Frohlich [21], Ebraheem et al. [22], and Choudhury and Saha [23] have performed geoelectrical surveys in different coastal area around the world.

In this paper we present the results of geoelectrical surveys, integrated with geochemical measurements, performed for the characterization of a coastal area along the Ionian side of the Basilicata region (Figure 1). This study area, located at the mouth of Bradano river (Metapontum,  $40^{\circ}22' N$ ,  $16^{\circ}51' E$ ), is mainly interested by a narrow shore (10–30 m) of fine sandy formations and has been affected by saltwater intrusion phenomena. This has caused the decline of the existing pine forest entailing significant ecological and environmental problems to the Metapontum Forest Reserve. Primary and secondary salinity of soil are linked to natural factors such as the climate, natural drainage patterns, topographic features, geological structure, distance to the sea, and by the indiscriminate exploitation of the soil and groundwater resources [1, 24, 25].

In order to manage rightly this kind of problem, it is necessary to have a thorough knowledge of the phenomenon, and the first objective of this study is to identify, through the use of different techniques and methodology, salt intake as the factor concurring or even determining the serious phenomenon of total decline and the deterioration of vegetation in the pine forest.

The geoelectrical investigations and chemical-physical analysis were carried out, to evaluate the seawater intrusion effect. In particular, geoelectrical surveys allowed to assess the extent and depth of the saltwater intrusion process, while the chemical-physical characterization was performed by considering some soil properties such as pH values, salt contents measured as the electric conductivity (ECe), exchangeable sodium, and cation exchange capacity. Moreover, this study aims to better delineate the saltwater intrusion front and to support the environmental protection and regeneration programs carried out by local and national

authorities for restoring the continuity of the woodland belt along the coast and consequently to obtain a reclassification of the landscape and protection of areas behind.

## 2. Study Area

The study area is located along the Ionian coastal plain, known as Metapontum plain. The area is made up of the regressive filling with marine sediments of a tectonic graben (Bradanic graben) during Pliocene to Pleistocene age. The area is bordered in the NE by the limestones of the Murgian foreland and in the SW by the clastic sediments of the Apennine chain. In the middle of the graben the full sedimentary sequence starts with sands, blue clays, covered by sands and gravels. The alluvial deposits in the estuarine environment are constituted of stratified sands to silty clays sediments. In this case, they are grey and very similar for aspect, but not for consistency, to the Pleistocene blue clays [4, 26, 27]. In particular, the Forest Reserve with an extent of about 240 hectares, situated in the north of the Ionian coastline between the mouth of rivers Bradano and Basento, is characterized by a superficial sandy substrate, and by clays and silts of river origin in the back dune zone (Figure 2).

The hydrogeology of the study area (Figure 3) is related to lithological and structural features of the same area, and they determine two types of aquifers.

An aquifer is constituted by marine terraces deposits and alluvial river valleys deposits, where the marine terraces aquifers show hydraulic conductivity from medium to high, equal or higher than the second type of aquifer constituted by coastal plain deposits.

The bottom of the this aquifer is a silty-clayey bed which lies under the sea level permitting the seawater intrusion, this phenomenon involves the coastal plain for a width of 1–1.5 km and it is less evident moving inwards where the altitude of the clayey bottom of the aquifer becomes progressively higher than the sea level [4].

The Metapontum coast is characterized by a strong erosive process. Marine erosion has really removed the dune behind the beach moving in the inland and causing the decline of the historical pinewood. Dunes and their vegetation are a natural defence against erosion by wind and sea and the variation of the line of the seashore is in close connection with the development of coastal dunes and their preservation [28]. Moreover, reduction of the coastal dune system in the study area facilitates the entry of salt water; dunes in fact, for their elevation and good infiltration capacity, give a sufficient freshwater recharge and a pressure above sea level, allowing hydrostatic control of saline intrusion [29].

Metapontum wooded strip is an artificial formation, planted in the first decade of the 50s in order to preserve the coast and the inland cultivated areas from salt sea wind. The forest is composed of Aleppo pine trees (*Pinus halepensis*) and domestic pine trees (*Pinus pinea*) prevalently. Secondary species are acacia saligna (*Acacia cianophylla*) and eucalyptus (*Eucalyptus globulus*, *E. camaldulensis*), besides other species that are typical of Mediterranean scrub as *Pistacia lentiscus*, *Juniperus macrocarpa* and *Juncos acutus*,

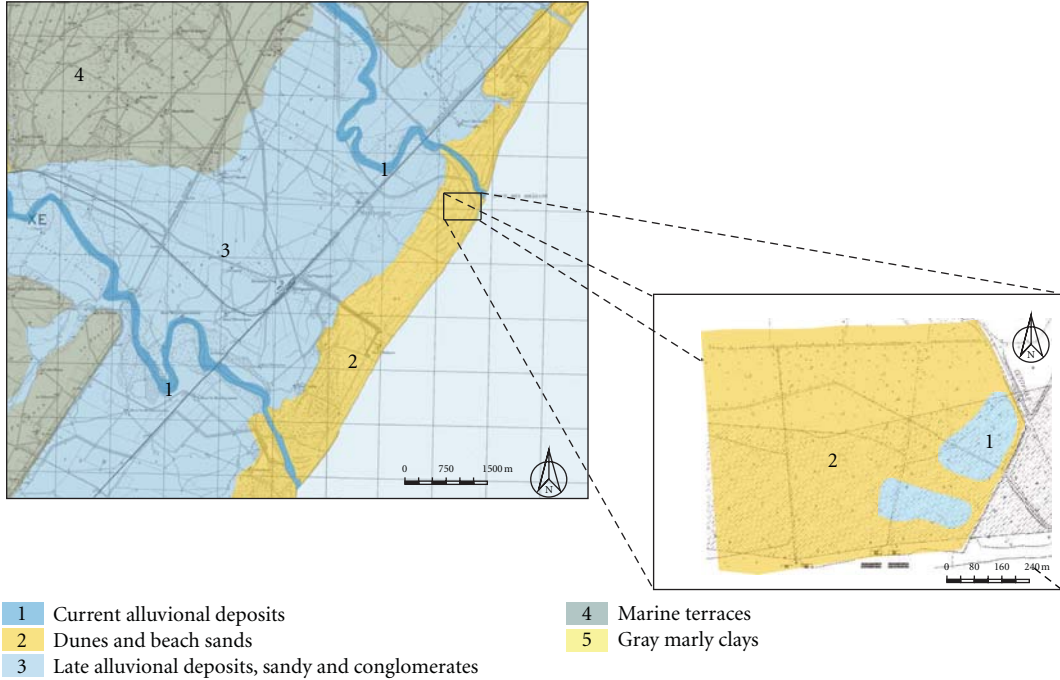


FIGURE 2: Geological map of the study area. (1) Current alluvial deposits; (2) dunes and beach sands; (3) late alluvial deposits sandy and conglomerates; (4) marine terraces; (5) gray marly clays.

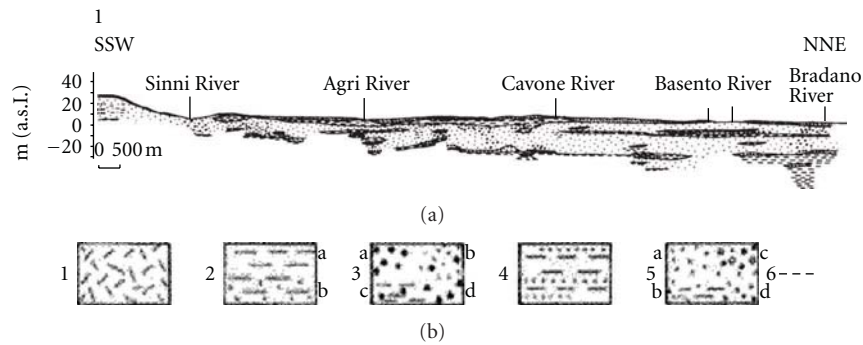


FIGURE 3: Schematic lithological section [4]. Legend: (1) soil; (2) clays or silty clays (yellow, brown, grey; (a) locally sandy clays (b); (3) pebbles (a) in a sandy (b) or clayey matrix (c); pebbles locally cemented (d); (4) grey sands with clayey strata; (5) grey or yellow sands and silty sands (a), locally clayey sands (b) or with gravels (c), locally sandstone strata (d); (6) piezometric level.

often mixed with the type of vegetation which prefers sandy soil (called “psammofila”). The rearrangement of soil was done with the realization of “baulature,” that is, elevation of soil in order to preserve tree roots from seawater intrusion.

On the basis of meteorological data, the climate of the area is semiarid with hot and dry summers; however, the evolution of the climate of the last period shows a trend to a reduction of annual precipitation and an increase in average temperatures [30].

### 3. Field Investigations and Sampling

In Figure 4 location of geoelectrical surveys and sampling points for chemical-physical analysis was indicated. The surveys have been performed during a geophysical campaigns

carried out in July, and in this time of year the investigated area, classified as climatic type semiarid, is characterized by drought.

**3.1. Geoelectrical Surveys.** Resistivity measurements were conducted as tomographies to determine variations with depth in soil resistivity.

The surface electrical resistivity tomographies are a useful tool in determining seawater intrusion in coastal areas for its capability to discriminate the large resistivity contrast between the presence of seawater that strongly reduces the resistivity values and saturated freshwater layers. Moreover, in order to evaluate if this contrast is significant and does not depend on geological layer, a validation of the geoelectrical

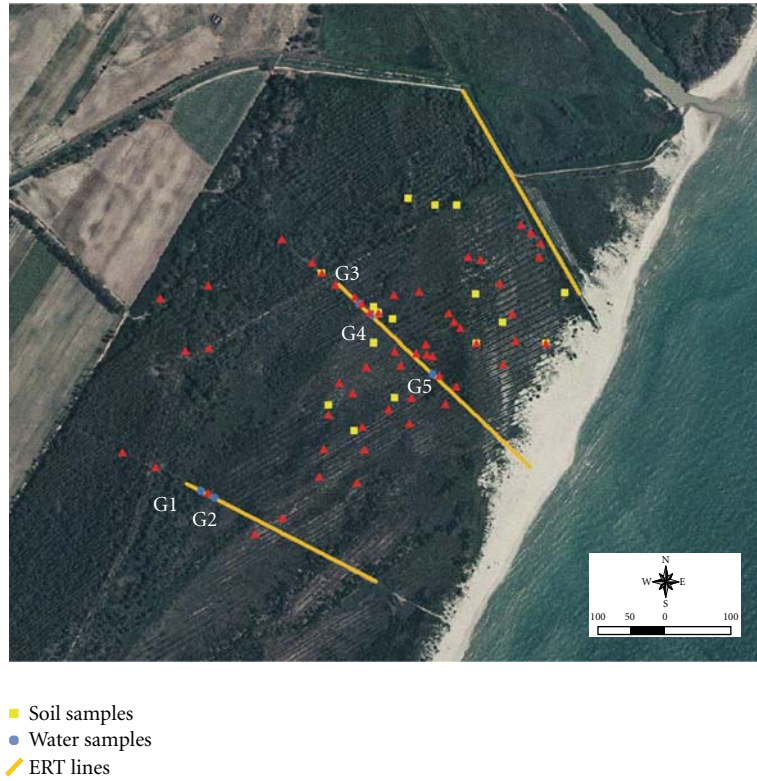


FIGURE 4: Location map of geophysical surveys and sampling points.

measurements with some chemical-physical analysis of soil samples has been performed.

Three electrical resistivity tomographies (ERT) were obtained using the georesistivity meter Syscal R2 (Iris Instruments) connected to a multielectrode system. We used a Wenner-Schlumberger configuration array with electrodes spacing on the surface of 10.00 meters. The electrical tomographies were all orthogonal to the coastline.

The Wenner-Schlumberger array provided horizontal and vertical resolution, and to obtain 2D resistivity models the data obtained were interpreted through the inversion algorithm, RES2DINV, proposed by Loke [31]. The measured values of apparent resistivity provide, in fact, a first preliminary image of the electrical subsurface structure denominated as the “pseudosection”. In a second step, the apparent resistivity measurements are transformed into true resistivity values using the rapid inversion algorithm of Loke and Barker [31].

The inversion routine is based on a smoothness-constrained least-squares method inversion algorithm that divides the subsurface into rectangular blocks, and the resistivity of the blocks is adjusted to minimize iteratively the difference between the computed and the measured apparent resistivity values; the root mean square (RMS) error gives a measure of this difference [31, 32].

**3.2. Soil and Water Sampling.** In addition, chemical and physical analyses on soil and water samples were performed in order to validate and integrate geophysical data. Undis-

turbed soil samples, collected from the surface in the first 40 cm of soil using Soil Sample Ring Kits (Eijkelkamp Equipment Netherlands), were taken for chemical analyses, using standard analytical procedures (Official Gazette of Italy No 248 of 21 October 1999). Soil samples were analyzed for pH (in water and in  $\text{CaCl}_2$ ), for cations ( $\text{Na}, \text{K}, \text{Ca}$ , and  $\text{Mg}$ ), for sulphates, chlorurs and nitrates, for organic matter and organic carbon, for cation exchange capacity, for an electrical conductivity of a saturated paste extract (ECe) or its inverse, electrical resistivity, and for texture. Groundwater samples were collected from few shallow holes across the area, since the groundwater table in the study area was high.

## 4. Results

The 2D resistivity results obtained by the inversion algorithm performed with the software RES2DINV are shown as images in Figure 5.

Electrical resistivity values are related to geological parameters of the subsurface and, in particular, resistivity values are controlled by the types of rocks and fluid. Then, the high-resolution electrical images are a powerful tool to identify conductive zones for the saltwater intrusion phenomena. Figure 5 shows the three 2D electrical images obtained in the study area related with depth and true resistivity of the subsoil investigated.

ERT 1 with direction NNW towards SE obtained on a rather flat regular surface, showed a first zone in the shallow part with values of 5–15  $\Omega\text{m}$  which could be associated with

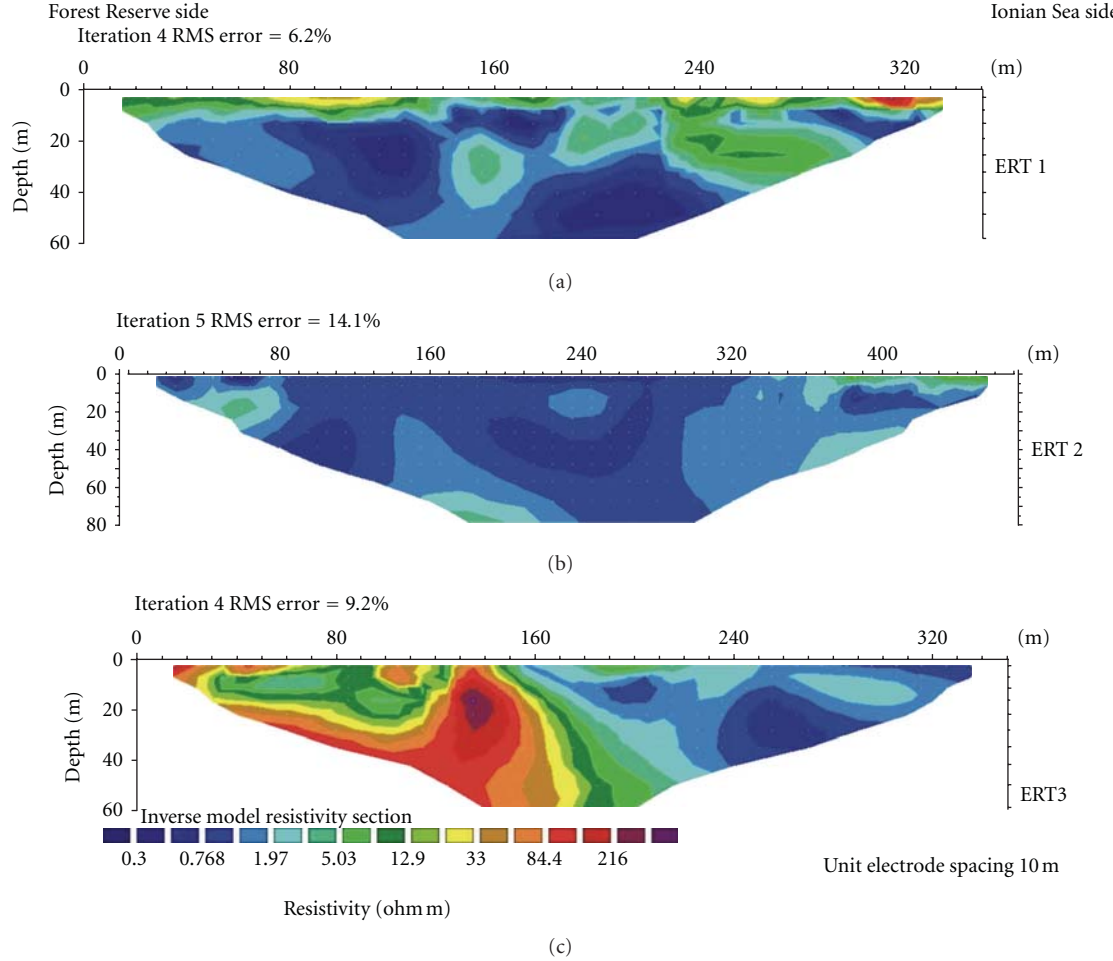


FIGURE 5: 2D electrical resistivity tomographies obtained in the investigated site. The position of each ERT is shown in Figure 3.

TABLE 1: Minimum and maximum values of chemical-physical data of soil samples collected in the study area.

Parameters	Minimum and Maximum Values
Na ( $\text{mg kg}^{-1}$ )	626–3425
K ( $\text{mg kg}^{-1}$ )	162–960
Ca ( $\text{mg kg}^{-1}$ )	917–2830
Mg ( $\text{mg kg}^{-1}$ )	203–905
Nitrogen ( $\text{g kg}^{-1}$ )	0.6–1.4
Organic carbon ( $\text{g kg}^{-1}$ )	4.9–21.5
Organic matter ( $\text{g kg}^{-1}$ )	8.4–37.1
pH ( $\text{H}_2\text{O}$ )	8.6–9.8
pH ( $\text{CaCl}_2$ )	7.9–8.9
Electrical conductivity (ECe) (Siemens $\text{m}^{-1}$ )	0.153–1.484
Electrical resistivity ( $\Omega\text{m}$ )	6.536–0.674
Cation exchange capacity (meq/100 gr)	7.4–17.2
Chlorurs ( $\text{mg kg}^{-1}$ )	162–5894
Nitrate ( $\text{mg kg}^{-1}$ )	<0.1
Sulphate ( $\text{mg kg}^{-1}$ )	15.3–441
Sand %	33.3–85.2
Silt %	7.1–35.7
Clay %	7.5–38.2

a layer filled with inert material, and a second one with lower resistivity values ( $\rho < 1.5 \Omega\text{m}$ ) reflecting saturated strata.

ERT 2 is nearly parallel to the direction of ERT 1, it runs from NW to SE. As shown in Figure 5, the geoelectrical image presents a lateral variation in resistivity distribution, with higher electrical resistivity values (about  $1\text{--}10 \Omega\text{m}$ ) towards SE in the first part of the section (between 0 and 110 m). Lower electrical resistivity values were observed towards sea side, and these values reduced are maybe due to saturated strata for a subsurface seawater flow zone.

ERT 3 in direction of WNW-SE shows a significant trend of resistivity, in fact, the resistivity section is characterized by two zones with different resistivity values: the first zone, towards the inland of the Forest Reserve and throughout the thickness of soil explored, shows moderate to high resistivity values  $10\text{--}220 \Omega\text{m}$ , while the second zone, towards the sea, shows very low resistivity values.

As expected, the 2D electrical resistivity tomographies show that resistivity values decrease in depth and from inland towards the Ionian Sea.

We have checked, one by one, the apparent resistivity values obtained during the field survey, and the topographic correction has been introduced. Only the apparent resistivity

TABLE 2: Electrical proprieties and pH values of groundwater samples.

Samples	pH	Electrical conductivity (ECe) Siemens m <sup>-1</sup> to 25°C	Electrical resistivity Ωm
G1	7.7	0.68	1.470
G2	7.7	0.81	1.234
G3	7.8	1.92	0.520
G4	7.3	2.92	0.342
G5	7.5	7.27	0.137
Sea water	8.2	5.66	0.176

measurements affected by a standard deviation lower than 5% have been considered. In a second step we have increased the number of iterations of the inversion software routine. After this procedure the RMS of the electrical imaging is lower than 15%. If we take into account the strong variability of the resistivity values from  $\sim 1000 \Omega\text{m}$  for sandy layers to  $\sim 1 \Omega\text{m}$  of fully saltwater saturated zones, this error can be considered acceptable.

We used the RES2DINV, that is, a well-assessed algorithm for 2D resistivity data inversion, and there is a large scientific literature in which the RMS of the 2D electrical imaging is greater than 10%. Electrical imaging of complex geological environments are generally affected by RMS greater than 15% [10, 33] and in many cases is not possible to reduce the RMS without introducing artifacts.

In literature, salt water resistivity values below  $1.0 \Omega\text{m}$  were reported, in fact, seawater has an average resistivity of  $0.2 \Omega\text{m}$  [16, 34], while the resistivity of a layer saturated by saline water and dissolved solids is in the range of 8 to  $50 \Omega\text{m}$  [13, 16, 35, 36]. Therefore, based on these values of resistivity of layers saturated by saline water and some dissolved solids reported in the literature, resistivity data obtained in this work from geoelectric investigations, highlight the presence of strata saturated with seawater.

In Tables 1 and 2 the results of laboratory analysis for the physical and chemical parameters of soil and groundwater samples were summarised. Laboratory analyses permit to suppose that high pH values are determined by the accumulation of sodium and magnesium on the soil exchange complex. In fact, in the study area, pH values (in  $\text{CaCl}_2$ ) have a range between 7.9 and 8.9 in soil samples, and between 7.3 and 7.8 in groundwater samples. A sample of sea water, instead, reported pH value of 8.2. Important differences were resulted in the conductivity (ECe) expressed in Siemens m<sup>-1</sup> or its inverse, electrical resistivity, expressed in Ohm m. The mean ECe value on soil samples was equal to  $0.613 \text{ Siemens m}^{-1}$ , corresponding to  $1.631 \Omega\text{m}$  with a range from  $0.153$  to  $1.484 \text{ Siemens m}^{-1}$ , equal to a range of resistivity from  $6.536$  to  $0.674 \Omega\text{m}$  while in water samples the mean ECe value was equal to  $2.720 \text{ Siemens m}^{-1}$ , corresponding to  $0.368 \Omega\text{m}$ , and with a range from  $0.68$  to  $7.27 \text{ Siemens m}^{-1}$ , equal to a range of resistivity from  $1.470$  to  $0.137 \Omega\text{m}$ .

On the other hand, in seawater samples ECe value was equal to  $5.660 \text{ Siemens m}^{-1}$ , corresponding to  $0.177 \Omega\text{m}$ . Furthermore, the major ions were  $\text{Na}^+$ ,  $\text{Ca}^{2+}$ , and  $\text{Cl}^-$ . Therefore, according to the classification NRCS [37], the area investigated presents from inland to coast, zones slightly saline, zones moderately saline, and zones close to highly

saline. The high concentration of soluble salts determines high osmotic pressure that makes very difficult to absorb water and nutrients from the roots of plants, creating the limiting factor to the diffusion and survival of forest species. The salinity distribution in the subsurface of study area is reflected by the vegetation cover, in fact, the zone with soil salinity is covered by salt-tolerant grasses [30]. On the basis of the geoelectrical measurements and of the chemical-physical analysis, the presence of zones with very low electrical resistivity values, can be associated to the intrusion of salt water into the subsoil. In the coastal environment, like the study area, hydraulic connection with seawater and inland gradient that move water to inland from seawater source, are such conditions as to cause seawater intrusion [2].

## 5. Conclusions

Geoelectrical surveys reveal the presence of two principal zones characterized by different resistivity values. The former is a strip back dune, closer to the sea, with a higher clay content and located at an altitude below sea level. It is submerged during the winter by water for a poor drainage, and it is characterized by lower resistivity values. The second zone is characterized by higher resistivity values and has a quite good vegetative cover for the best environmental conditions, greater distance from the sea, and elevation above sea level. In this area the spontaneous emergence of new plant pine is frequently observed for the fact that soil conditions are favourable as there is no seawater intrusion yet.

Results presented in this paper showed that the process of salt water is active on coastal Forest Reserve of Metapontum, and geoelectrical surveys have proved to be precious tools. Geoelectrical surveys have highlighted significant variations in subsurface resistivity associated with lithological characteristics of underground layers and variations in water saturation. In particular, these surveys have produced images of resistivity of the soil investigated, where the spatial distribution of brackish and saline water in the pine forest and resistivity variation with depth is very clear. These observations are also confirmed from laboratory analysis on soil and groundwater samples.

## Acknowledgments

The authors would like to thank the *Corpo Forestale dello Stato* for the availability and logistic support during the measures in the Reserve. The authors are also grateful

to Dr. Achille Palma, Metapontum Agrobios, for the soil chemical analyses. This paper was supported by MIUR in the framework of “Tecnologie per le Osservazioni della Terra e i Rischi Naturali -TeRN” project (PON 2004–2006; Obiettivo Realizzativo OR2).

## References

- [1] V. E. A. Post, “Fresh and saline groundwater interaction in coastal aquifers: is our technology ready for the problems ahead?” *Hydrogeology Journal*, vol. 13, no. 1, pp. 120–123, 2005.
- [2] C. P. Petalas and I. B. Diamantis, “Origin and distribution of saline groundwaters in the upper Miocene aquifer system, coastal Rhodope area, northeastern Greece,” *Hydrogeology Journal*, vol. 7, no. 3, pp. 305–316, 1999.
- [3] C. Petalas and N. Lambrakis, “Simulation of intense salinization phenomena in coastal aquifers—the case of the coastal aquifers of Thrace,” *Journal of Hydrology*, vol. 324, no. 1–4, pp. 51–64, 2006.
- [4] M. Polemio, P. P. Limoni, D. Mitolo, and F. Santaloia, “Characterisation of the Ionian-Lucanian coastal aquifer and seawater intrusion hazard,” in *Proceedings of the 17th Salt Water Intrusion Meeting*, pp. 422–434, Delft, The Netherlands, 2002.
- [5] M. A. Somay and U. Gemici, “Assessment of the salinization process at the coastal area with hydrogeochemical tools and geographical information systems (GIS): Selçuk plain, Izmir, Turkey,” *Water, Air, and Soil Pollution*, vol. 201, no. 1–4, pp. 55–74, 2009.
- [6] D. W. Steeples, “Engineering and environmental geophysics at the millennium,” *Geophysics*, vol. 66, pp. 31–35, 2001.
- [7] V. Lapenna, P. Lorenzo, A. Perrone, S. Piscitelli, E. Rizzo, and F. Sdao, “2D electrical resistivity imaging of some complex landslides in the Lucanian Apennine chain, southern Italy,” *Geophysics*, vol. 70, no. 3, pp. B11–B18, 2005.
- [8] S. Pantelis, M. Kouli, F. Vallianatos, A. Vafidis, and G. Stavroulakis, “Estimation of aquifer hydraulic parameters from surficial geophysical methods: a case study of Keritis Basin in Chania (Crete—Greece),” *Journal of Hydrology*, vol. 338, no. 1–2, pp. 122–131, 2007.
- [9] D. Chianese and V. Lapenna, “Magnetic probability tomography for environmental purposes: test measurements and field applications,” *Journal of Geophysics and Engineering*, vol. 4, no. 1, article 08, pp. 63–74, 2007.
- [10] V. Naudet, M. Lazzari, A. Perrone, A. Loperte, S. Piscitelli, and V. Lapenna, “Integrated geophysical and geomorphological approach to investigate the snowmelt-triggered landslide of Bosco Piccolo village (Basilicata, southern Italy),” *Engineering Geology*, vol. 98, no. 3–4, pp. 156–167, 2008.
- [11] R. Balia, E. Gavaudò, F. Arda, and G. Ghiglieri, “Geophysical approach to the environmental study of a coastal plain,” *Geophysics*, vol. 68, no. 5, pp. 1446–1459, 2003.
- [12] A. T. Batayneh, “Use of electrical resistivity methods for detecting subsurface fresh and saline water and delineating their interfacial configuration: a case study of the eastern Dead Sea coastal aquifers, Jordan,” *Hydrogeology Journal*, vol. 14, no. 7, pp. 1277–1283, 2006.
- [13] P. Bauer, R. Supper, S. Zimmermann, and W. Kinzelbach, “Geoelectrical imaging of groundwater salinization in the Okavango Delta, Botswana,” *Journal of Applied Geophysics*, vol. 60, no. 2, pp. 126–141, 2006.
- [14] M. A. Koukoudaki, G. P. Karatzas, M. P. Papadopoulou, and A. Vafidis, “Identification of the saline zone in a coastal aquifer using electrical tomography data and simulation,” *Water Resources Management*, vol. 21, no. 11, pp. 1881–1898, 2007.
- [15] S. E. Kruse, M. R. Brudzinski, and T. L. Geib, “Use of electrical and electromagnetic techniques to map seawater intrusion near the Cross-Florida Barge Canal,” *Environmental and Engineering Geoscience*, vol. 4, no. 3, pp. 331–340, 1998.
- [16] A. A. Nowroozi, S. B. Horrocks, and P. Henderson, “Saltwater intrusion into the freshwater aquifer in the eastern shore of Virginia: a reconnaissance electrical resistivity survey,” *Journal of Applied Geophysics*, vol. 42, no. 1, pp. 1–22, 1999.
- [17] S. S. Abdul Nassir, M. H. Loke, C. Y. Lee, and M. N. M. Nawawi, “Salt-water intrusion mapping by geoelectrical imaging surveys,” *Geophysical Prospecting*, vol. 48, no. 4, pp. 647–661, 2000.
- [18] M. Sheriff, A. El Mahmoudi, H. Garamoon, and A. Kacimov, “Geoelectrical and hydrogeochemical studies for delineating seawater intrusion in the outlet of Wadi Ham, UAE,” *Environmental Geology*, vol. 49, no. 4, pp. 536–551, 2006.
- [19] A. Cimino, C. Cosentino, A. Oieni, and L. Tranchina, “A geophysical and geochemical approach for seawater intrusion assessment in the Acquedolci coastal aquifer (Northern Sicily),” *Environmental Geology*, vol. 55, no. 7, pp. 1473–1482, 2008.
- [20] M. H. Khalil, “Geoelectric resistivity sounding for delineating salt water intrusion in the Abu Zenima area, west Sinai,” *Egypt Journal of Geophysics and Engineering*, vol. 3, pp. 243–251, 2006.
- [21] D. W. Urich and R. K. Frohlich, “Surface electrical resistivity in coastal groundwater exploration,” *Geoexploration*, vol. 26, no. 4, pp. 267–289, 1990.
- [22] A. A. M. Ebraheem, M. M. Senosy, and K. A. Dahab, “Geoelectrical and hydrogeochemical studies for delineating groundwater contamination due to salt-water intrusion in the northern part of the Nile Delta, Egypt,” *Ground Water*, vol. 35, no. 2, pp. 216–222, 1997.
- [23] K. Choudhury and D. K. Saha, “Integrated geophysical and chemical study of saline water intrusion,” *Ground Water*, vol. 42, no. 5, pp. 671–677, 2004.
- [24] G. Spilotro, F. Canora, F. Caporale, G. Leandro, and N. Vignola, “Hydrogeology and groundwater salinization in the ionian coastal plane of the Basilicata Region,” in *Proceedings of the 17th Salt Water Intrusion Meeting*, pp. 422–434, Delft, The Netherlands, 2002.
- [25] E. Amezketa, “An integrated methodology for assessing soil salinization, a pre-condition for land desertification,” *Journal of Arid Environments*, vol. 67, no. 4, pp. 594–606, 2006.
- [26] N. Ciaranfi, M. Maggiore, P. Pieri, L. Rapisardi, G. Ricchetti, and N. Walsh, “Considerazioni sulla neotettonica della Fossa bradanica,” in *Nuovi Contributi Alla Realizzazione Della Carta Neotettonica d’Italia*, vol. 251, pp. 73–96, C.N.R. Progetto Finalizzato Geodinamica, Napoli, Italy, 1979.
- [27] M. Tropeano, L. Sabato, and P. Pieri, “The Quaternary “Post-turbidite” sedimentation in the South-Apennines Foredeep (Bradanica Trough-Southern Italy),” *Italian Journal of Geosciences Bull*, vol. 1, pp. 449–454, 2001.
- [28] E. Valpreda and U. Simeoni, “Assessment of coastal erosion susceptibility at the national scale: the Italian case,” *Journal of Coastal Conservation*, vol. 9, no. 1, pp. 43–48, 2003.
- [29] B. M. S. Giambastiani, M. Antonellini, G. H. P. Oude Essink, and R. J. Stuurman, “Saltwater intrusion in the unconfined coastal aquifer of Ravenna (Italy): a numerical model,” *Journal of Hydrology*, vol. 340, no. 1–2, pp. 91–104, 2007.
- [30] A. Satriani, A. Loperte, T. Simoniello, M. D’Emilio, C. Belviso, and V. Lapenna, “A multidisciplinary approach for studying

- the forest reserve of Metapontum (southern Italy) affected by saltwater intrusion phenomena," *EGU Geophysical Research Abstracts*, vol. 9, 2007.
- [31] M. H. Loke and R. D. Barker, "Rapid least-squares inversion of apparent resistivity pseudosections by a quasi-Newton method," *Geophysical Prospecting*, vol. 44, no. 1, pp. 131–152, 1996.
  - [32] Y. Sasaki, "Resolution of resistivity tomography inferred from numerical simulation," *Geophysical Prospecting*, vol. 40, no. 4, pp. 453–463, 1992.
  - [33] A. Perrone, G. Zeni, S. Piscitelli et al., "Joint analysis of SAR interferometry and electrical resistivity tomography surveys for investigating ground deformation: the case-study of Satriano di Lucania (Potenza, Italy)," *Engineering Geology*, vol. 88, no. 3-4, pp. 260–273, 2006.
  - [34] D. S. Parasnis, *Principle of Applied Geophysics*, Chapman & Hall, London, UK, 1986.
  - [35] W. De Breuk and G. De Moor, "The water table aquifer in the eastern coastal area of Belgium," *Bulletin of the International Association of Scientific Hydrology*, vol. 14, pp. 137–155, 1969.
  - [36] A. A. R. Zohdy, P. Martin, and R. J. Bisdorf, "A study of seawater intrusion using direct-current soundings in the south-eastern part of the Oxnard Plain, California," Open-File Report 93-524, Geological Survey, 1993.
  - [37] Soil Survey Division Staff, *Soil Survey Manual USDA Agric Handbook 18*, U.S. Government Printing Office, Washington, DC, USA, 1993.

## Research Article

# Geoelectrical Tomography Investigating and Modeling of Fractures Network around Bittit Spring (Middle Atlas, Morocco)

**Kh. Qarqori,<sup>1</sup> M. Rouai,<sup>1</sup> F. Moreau,<sup>2</sup> G. Saracco,<sup>3</sup> O. Dauteuil,<sup>2</sup> D. Hermitte,<sup>3</sup> M. Boualoul,<sup>1</sup> and C. Le Carlier de Veslud<sup>2</sup>**

<sup>1</sup>Earth Sciences Department, Faculty of Sciences, Moulay Ismail University, 11201 Zitoune, Meknès 50000, Morocco

<sup>2</sup>Geosciences Rennes, Rennes 1 University, UMR CNRS 6118, Avenue GL Leclerc, Campus Beaulieu, Bat 15 CS74205, 35042 Rennes Cedex, France

<sup>3</sup>CNRS-CEREGE, Aix-Marseille University, UMR 6635 Europole de l'Arbois, BP 80, 13545 Aix en Provence, Cedex 4, France

Correspondence should be addressed to M. Rouai, mohamed.rouai@laposte.net

Received 30 June 2011; Accepted 16 September 2011

Academic Editor: Pantelis Soupios

Copyright © 2012 Kh. Qarqori et al. This is an open access article distributed under the Creative Commons Attribution License, which permits unrestricted use, distribution, and reproduction in any medium, provided the original work is properly cited.

Direct current Resistivity (DCR) method was carried out to characterize the hydrogeological connection between the Tabular Middle Atlas (TMA) and the Saïs Basin. The TMA is one of the most important aquifers in northern Morocco that supplies the deep aquifer of the Saïs Basin. Electrical resistivity tomography (ERT) survey was focused on the Bittit area that is one of the most important outlet discharges, and it is representative of the relations between the TMA and the Saïs Basin. The high resolution capabilities of the electrical tomography were used to define the geological draining features in the framework of water paths from the TMA to the karstic springs. The synthetic data were calculated for the similar model expected in field data inversion and inversion result of these synthetic data used as a guide for the interpretation of the inverse data resistivity sections. Joint interpretation of geophysical, geological, structural, and synthetic simulation data allowed identifying a conductive horizontal shallow layer overlying two subvertical families of fractures of NE-SW and NW-SE directions. This result leads to propose hydrological behaviour of water from the Tabular Middle Atlas and the Saïs Basin at the Bittit Spring, which takes into account for both horizontal flows through stratification joints or karst and through subvertical fractures.

## 1. Introduction

Water resources and management is one of the major environmental issues in Morocco. The climate changes (decrease of rainfalls) and the increase of water needs for human activities (farming, industry, individual needs) make critical the management of water resources. The precipitations are mainly located in mountains while water requirements are located in the plains: a good understanding of water transfer between these areas is absolutely necessary. The Middle Atlas is a mountain long of about 350 km from south-western to north-eastern Morocco, located between the Rif and High Atlas. The mountain has cold winters with persistent snow above 2000 m. The western border is well watered (from 1000 to 1500 mm annually) because of the meteorological perturbations coming from the Atlantic Ocean. The Tabular Middle Atlas (TMA) located at the NW border of the

Middle Atlas is made up of Liassic limestone and dolomite forming a complex karstic system locally highly fractured (Figure 1(a)). It is one of the most important reservoirs in northern Morocco because of the climatic context and of its structure. The water flows essentially along open fractures and karst cavities, with very low matrix permeability [1]. Although it represents a large groundwater potential, it is still badly exploited because of the lack of data about fracture network, aquifer geometry, and recharge area. It makes difficult to define optimally the potential areas of drilling. This reservoir is connected to large aquifer located in the Saïs plain, at north of the TMA. This aquifer can supply water to two large cities (Fez and Meknes) and small villages. The Liassic reservoir of TMA dips in the Saïs Basin under a thick Tertiary marly series, forming an important confined aquifer (Figures 1(a) and 1(b)). Groundwater circulation from TMA to the Saïs Basin is complex due to fracturing and

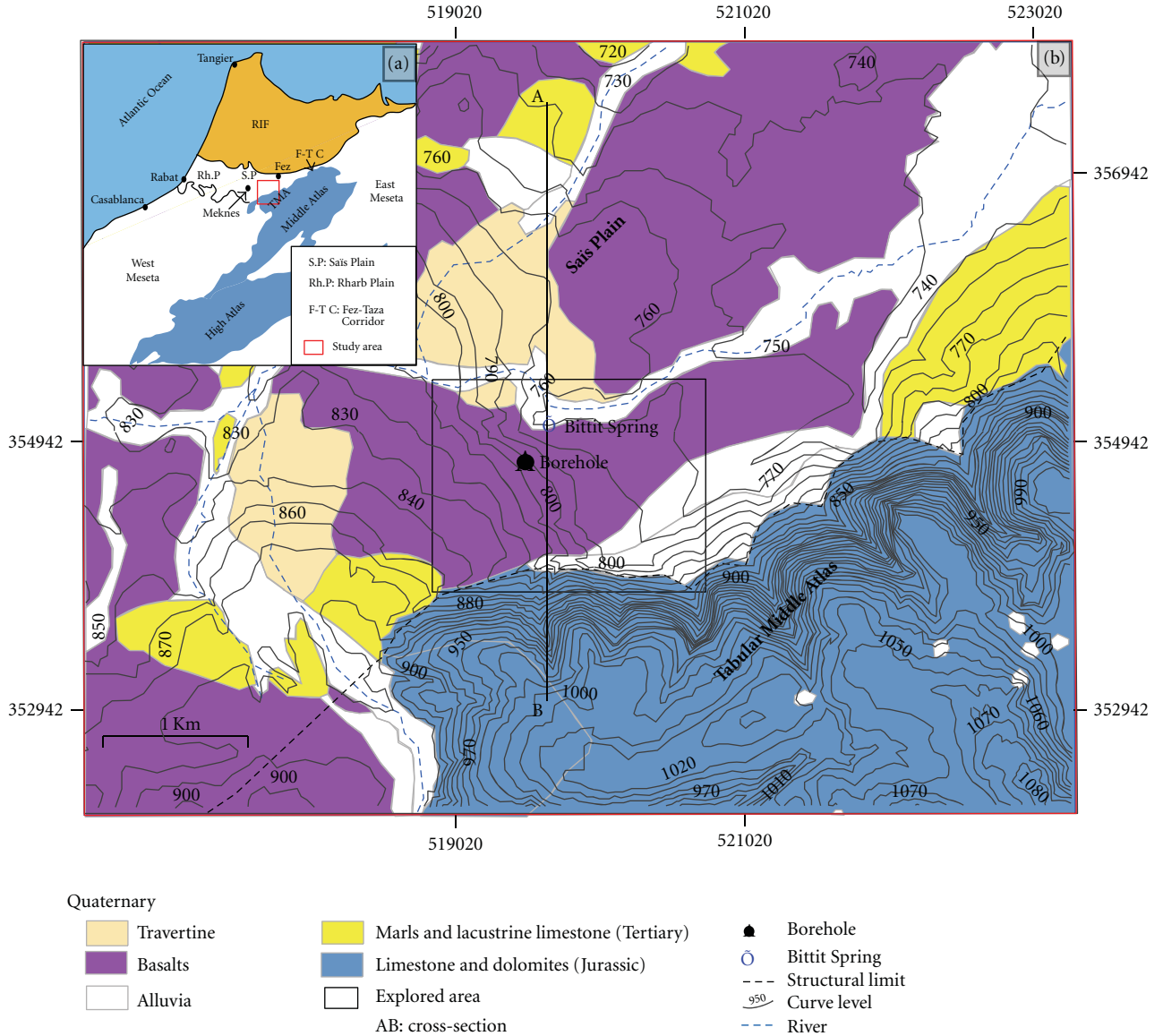


FIGURE 1: (a) Geographic location of study area. (b) Geological map of Bittit area with surveyed area in black rectangular.

to karstic Quaternary travertine overlying Lias carbonates. The geometry of the aquifer, water flow paths, and the complex underground karstic organization are misknown due to lack of high resolution geophysical survey. Therefore, a better understanding of hydrogeological behaviour of fracture and karst networks is fundamental for management and protection of water resources.

The goal of this study is to characterize the transition between the reservoir of the TMA where the water is accumulated and the Saïs Basin where the water is used. In this paper, we focus on the underground imaging and on mapping of fractures network in the Bittit Spring area that constitutes one important rising spring at the junction between the TMA and the Saïs Basin, with a great average annual flow of about 1600 l/s (Figure 1(b)). Therefore, it is considered as a representative area of the hydrogeological connections between the TMA and the Saïs plain. To high-

light these issues, we choose a geophysical imaging by electrical Resistivity Tomography (ERT), which is an important prospecting tool adapted to groundwater research. Recently, this technique has been largely applied in geophysical investigation of areas having complex geology [2, 3] it allows imaging the geometry of underground structures with high resolution and can detect the vertical and lateral electrical resistivity variations induced by rock properties and water content. After a complete description of the studied area, we described the ERT data acquisition and results. The field data are interpreted by using 2D inversion algorithm after topographic correction and a shape filtering. We performed a synthetic modelling in order to refine interpretations of the ERT. Finally, a 3D view was realized to check the geometrical compatibility between the various detected structures and then to define a model of draining hydraulic features.

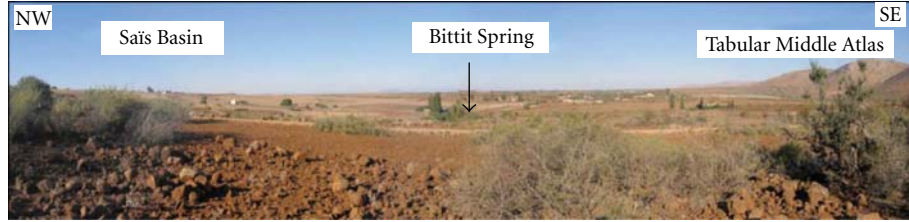


FIGURE 2: Panorama showing the Bittit spring on the Saïs basin and TMA junction.

## 2. Geological and Hydrological Settings

The Middle Atlas and the Rif dominate the landscape of Northern Morocco. The Middle Atlas is separated from the southern ridges of the Rif belt by the Saïs plain. Mesoenozoic sediments covering Paleozoic units mainly form this plain and the Middle Atlas. They are deformed during the Mesozoic extension and Cenozoic compression. At North of Middle Atlas, the Tabular Middle Atlas (TMA) corresponds to an elevated tabular structure fractured during the Cenozoic.

The TMA is a large karstic plateau whose elevation ranges between 1000 m and 2200 m. It is mostly made up of Liassic limestones and dolomites overlying clays and basalts of the Triassic and the Paleozoic formations. The Quaternary is represented by alkaline basalt lava flows coming from the Outgui volcano and going to the Saïs plain and by travertine frequently located at the emergences of springs at the junction with the Saïs Basin.

TMA is affected by major NE-SW flexures clearly visible except under basaltic flows and by an intense fracturing with main NE-SW and NW-SE directions. The discharge of TMA aquifer occurs essentially in a complex system of springs in its northern border at the junction with the Saïs Basin [4].

The Saïs plain is an asymmetrical E-W sedimentary basin of 2100 km<sup>2</sup> average total surface where elevation ranges between 500 m and 700 m. It is limited by the Pre-Rif ridges in the north, by TMA in the south, by the Rharb plain in the west and by the Fez-Taza corridor in the east. The Saïs Basin mainly consists of thick Miocene marls reaching 1 km near Fez, overlying, deep carbonate (limestones and dolomites) Lias aquifer and covered by the Plio-Quaternary lacustrine limestone and sandstone that constitute a water table aquifer of less importance. The recent quaternary is represented by basalt flows, alluvial cones, and travertine on the TMA edge [5].

The geophysical surveys carried out in this basin revealed thick Miocene marls at north, several flexures affecting Pliocene-Miocene deposits, and normal faults affecting the Liassic carbonates. The flexures result from the replay accidents of the Palaeozoic bedrock and are also influenced by the Rif tectonic [6]. Several boreholes and geophysical surveys show variations in thicknesses and depths of Lias that is the most important aquifer [7]. The Lias reservoir is affected by several faults generating discontinuous blocks which are either raised or collapsed; by consequence, this deep aquifer is discontinuous [5]. Two aquifers are present in the Saïs Basin: one shallower (<80 m) in the Pliocene-Quaternary

formations and a second deeper (up to 1000 m) in the Liassic carbonates. The monitoring of the deep aquifer in the Saïs Basin displays a regular decrease of the water level due to the drought and the overpumping [7].

The Liassic formations are the loci of the water storage and of the circulation both in the TMA and in the Saïs plain. However, groundwater circulations between these two structures are complex because faulting, karst connection, and dolomite geometry control it. Up to now, water flow paths and underground karsts organization remain unknown.

In order to characterize this transition between the TMA and the Saïs Basin, we investigated the Bittit Spring area located at 32 km southeast of Meknes, at the junction between the Tabular Middle Atlas and the Saïs Basin (Figure 2). The Bittit Spring is one of the most important in term of flowing with an average annual discharge of about 1600 l/s. Amraoui, 2005 [7] concluded that the hydrogeological system of Bittit has significant storage, sustained discharge during the year, and relative slow flow. However, the spring discharge decreases regularly as a result of a long drought.

We carried out a 100 m borehole close to the Bittit Spring to identify precisely the stratigraphy around the spring (Figure 3). This information will be used to interpret the DCR data. From bottom to top, the borehole showed 57 m of Triassic clays, 33 m of a succession of limestones and marls of Liassic, dolomites of middle Liassic, a large unconformity, and at least a travertine limestone covered by the basalt flow. However, this borehole cannot be generalized on the whole study area, because other boreholes show different lithological facies of Quaternary formations, the presence of Miocene marls, and different depths of the Lias carbonates location. The faulting is probably the main reason of these depth variations.

## 3. DCR Tomography Survey and Processing

**3.1. 2D Inversion of DCR Tomography Data.** Electrical prospecting methods are particularly well adapted to geoelectrical discontinuities, faults, and water investigation [8]. Among these methods, Electrical Resistivity Tomography (ERT) allows to conduct fast data acquisition and to obtain underground 2D images with high resolution suitable for fracture identification [9].

Determination of the underground geometrical structure with electrical methods depends on the resistivity contrasts of the underground rocks. Electrical resistivity of rocks varies according to several parameters like porosity, weathering and water content. Chapellier and Mari [10] assigned wide

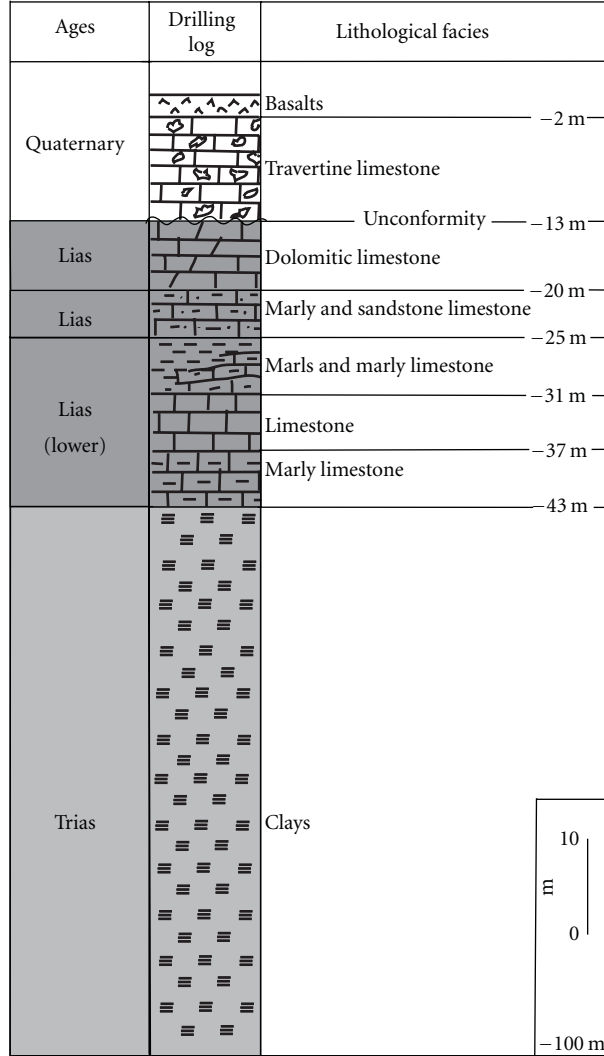


FIGURE 3: Bittit's borehole log (location on Figure 1).

ranges of electrical resistivity for various classes of rocks. In the absence of laboratory measurements of in situ samples, local vertical electrical soundings can be used to reduce the range of resistivity corresponding to the lithologies of our studied area. In the TMA, Benslimane [11] found ranges of about [25–250  $\Omega\text{m}$ ], [2000–5000  $\Omega\text{m}$ ], [500–1500  $\Omega\text{m}$ ], and [1–20  $\Omega\text{m}$ ], respectively corresponding to weathered basalts, limestones, fractured limestones, and to clays. Another study [12] was carried out in the west of the Sais Basin and determined other ranges of about [50–200  $\Omega\text{m}$ ] for travertine, [20–40  $\Omega\text{m}$ ] for the recent cover, [3–30  $\Omega\text{m}$ ] for marls, [100–400  $\Omega\text{m}$ ] for Liassic carbonates, and 30  $\Omega\text{m}$  for clays. The lithologies in the Bittit Spring area have then contrasted geoelectrical properties: limestone and dolomite have a relatively high electrical resistivity in regards to marls and altered basalt. These contrasting electrical properties should enable us to highlight the underground geometry of the Bittit Spring area with electrical prospecting methods.

Seven ERT profiles were carried out around the Bittit Spring (Figure 4). Apparent resistivity data were acquired by an ABEM Terrameter SAS1000 and a multielectrode LUND imaging system using a Wenner array configuration of 64 electrodes and 5 m spacing. It allows investigating a depth of about 50 m. The lengths of the profiles vary from 315 m to 395 m with a rollup of the cables. Geological map of the Bittit area provides major NE-SW and NW-SE fault direction that helped to define the direction of the profiles. Some profiles have also been crossed to obtain resistivity information in perpendicular directions.

2D inversion and topographic correction of the pseudosections were performed using the Res2DInv [13] software package. Outliers were removed, and topographic corrections were carried out with measurements of elevation and geographic coordinates for each electrode position through an inclinometer and a GPS. Finally, all the pseudosections were inverted by the least squares method with the same inversion parameters and with 5 iterations, giving root mean

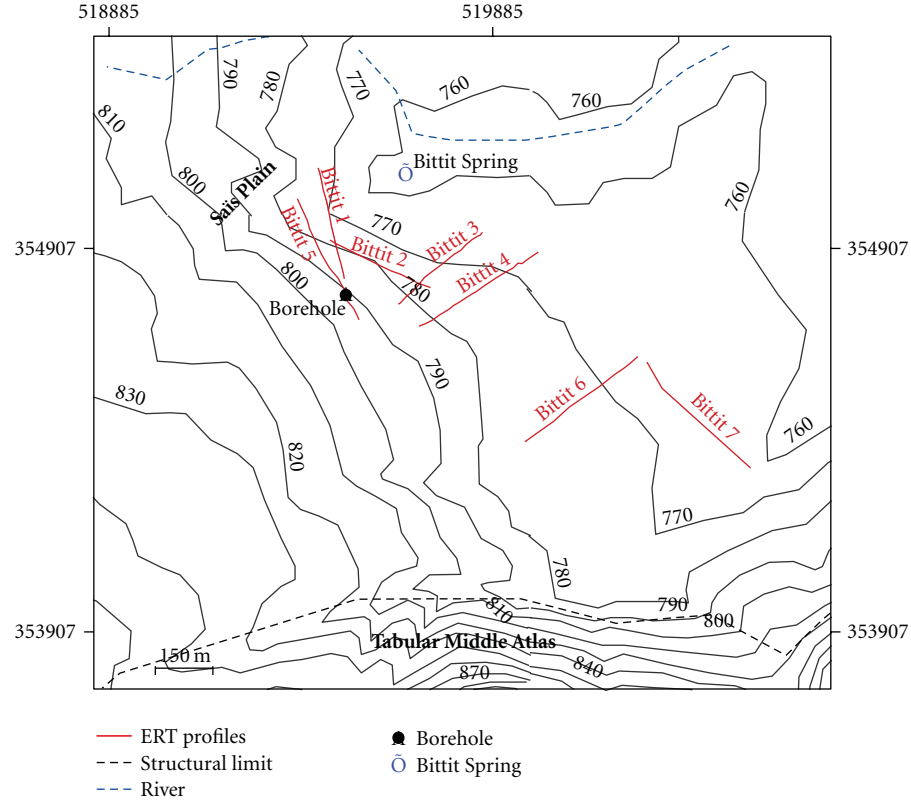


FIGURE 4: Positioning plan of electrical tomography profiles.

square value less than 6% between the data and the calculated pseudosections.

**3.2. ERT Inversion Results.** The inversion of the pseudosections data was performed using the Res2DInv software package. The resulting sections display various electrical resistivities ranging from less than  $10 \Omega\text{m}$  to more than  $1000 \Omega\text{m}$  (Figure 5). Observing the inversion results, we have classified the resistivity values into three ranges of resistivities: [10 to  $70 \Omega\text{m}$ ] represents the conducting structures, [ $70$  to  $215 \Omega\text{m}$ ] for the intermediate structures, and [ $\geq 215 \Omega\text{m}$ ] for the resistant structures.

The electrical sections on the NE-SW direction (Bittit 3, Bittit 4, and Bittit 6, resp. from the spring to the TMA) generally show the presence of horizontal structures, with three distinctive features. We observe first a very resistant layer ( $\sim 500 \Omega\text{m}$ ) on the summit part of Bittit 4 section, secondly a conducting layer ( $< 40 \Omega\text{m}$ ) which become increasingly deep and thick while going from TMA (depth of  $-10 \text{ m}$  on Bittit 6) towards the Bittit Spring (depth of  $-35 \text{ m}$  on Bittit 3), and thirdly a very resistant layer ( $> 215 \Omega\text{m}$ ) which appears from  $-15 \text{ m}$  depth on Bittit 6 section and dip while going towards the spring to reach a depth of about  $-30 \text{ m}$  to  $-40 \text{ m}$  on the Bittit 3 section. This resistant block is always limited by subvertical edges and is in contact with a layer with intermediate resistivity value.

Contrary to the NE-SW profiles, the electrical sections on the NW-SE direction (Bittit 1, Bittit 2, Bittit 5, and Bittit 7)

show the presence of vertical structures and heterogeneous and complex aspect. First, the Bittit 7 profile was carried out perpendicularly to the NE-SW profiles in order to verify the presence of the upper conducting layer and its extension towards the TMA. The result shows that this structure seems to be almost continuous from the TMA at the SE to the spring at the NW. We observe also a very resistant block ( $\sim 1000 \Omega\text{m}$ ) with a length of approximately  $80 \text{ m}$ , limited by conducting vertical structures on the Bittit 5 and Bittit 7 sections. It should be noticed a lack of some data due to the using the roll-up on profiles of Bittit 4, 5, 6, and 7, in a zone width of about  $55 \text{ m}$  and centered at  $x = 265 \text{ m}$  for Bittit 4, 5, 6 and  $x = 125 \text{ m}$  for Bittit 7, at depths between  $40 \text{ m}$  to  $47.5 \text{ m}$  from the ground surface. Therefore, the lateral extent of the resistive blocks and the resistivity value on these profiles must be taken with caution. Nevertheless, we can observe that these resistive blocks are individualised and dislocated by vertical conducting structures on Bittit 2, Bittit 5, and Bittit 7 sections and also by a heterogeneous distribution of the resistivities, especially on Bittit 1 and Bittit 5 sections.

To sum up, the main electrical structures consist of (1) a shallow subhorizontal conductive layer and (2) a deeper resistive layer, discontinuous due to subvertical conducting structures and heterogeneous resistivity media.

**3.3. Filtering (V/H FF).** The resistivity inversion provides a first image of the geometry of the underground that

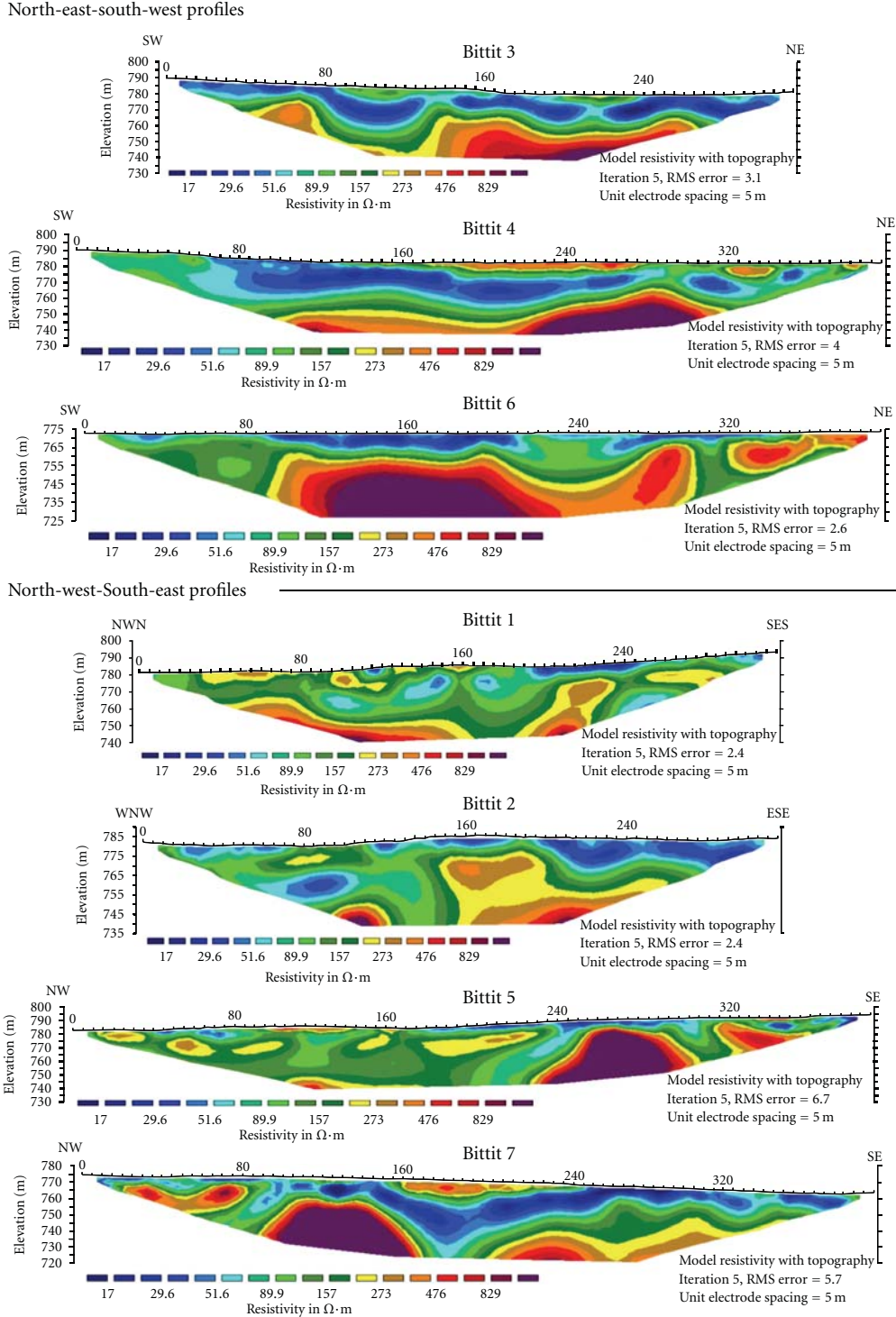


FIGURE 5: Inverse model resistivity sections. The same color scale has been used on each profile in order to compare all the results.

smoothes the edge of the geological contacts. In order to limit this effect and to define more precisely the limits of horizontal layers or to improve the detection of the subvertical features, we used the Res2DInv vertical-to-horizontal flatness filter ratio (V/H FF). This filter fixes a relative weight between a vertical flatness filter ( $f_z$ ) and a horizontal

flatness filter ( $f_x$ ) in order to take into account the a priori information about the shape of the geological structures if any. By default, the same factor is used for both. Thus, we selected a higher value for the ratio of the V/H FF in order to force the program to produce models that are vertically stretched.

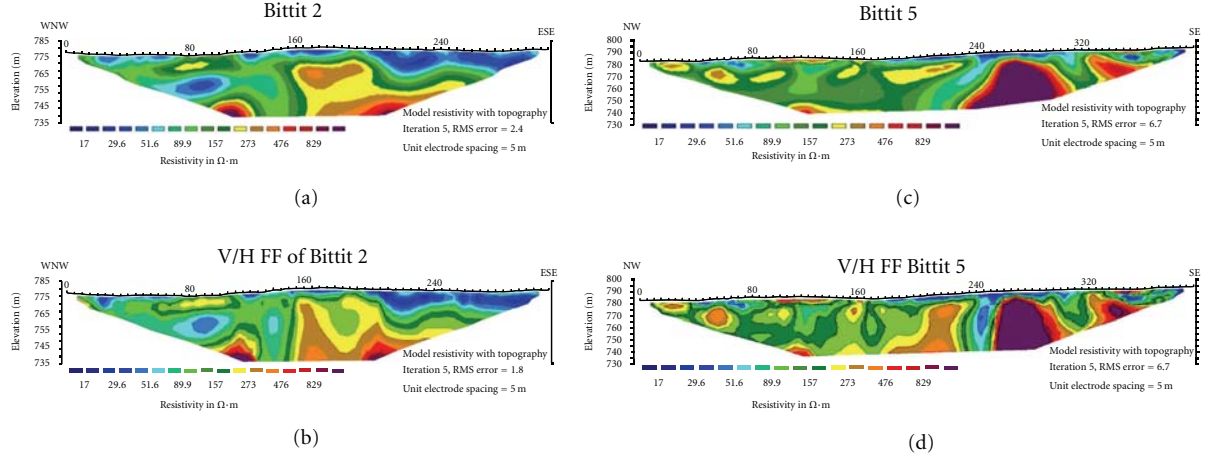


FIGURE 6: (a) and (c) Inverse models of Bittit 2 and Bittit 5 before V/H FF application. (b) and (d) Inverse models sections of Bittit 2 and Bittit 5 after V/H FF application with a ratio of 4, amplifying vertical structures.

We have applied this filter with a ratio of 4 for all profiles. In this paper, we show only the results for two of them, representative of the obtained results. Figure 6 shows structures with a higher apparent dip than that observed on the unfiltered sections. In some cases, new vertical structures appear (see Bittit 5 on Figure 6(d)) which were not clearly detected on the first inversion results or which were on the edges of the section and are likely to be confused with edge effects.

We have also applied this filter using a ratio of 0.6 in order to produce models with horizontally stretched structures. This filtering slightly decreases the response of some vertical structures which continue to appear with almost the same dip as in the unfiltered sections. It also removes some vertical structures in the case of Bittit 1, 4, and 6 which became completely horizontal. Then, the vertical structures that persist in both cases are interpreted as vertical geological features of our study area.

Although this filter does not allow a precise quantitative interpretation, for example, of the dip angle or of the structures extension, it enables us to validate the presence of subvertical structures that were finally used on the geological and hydrological interpretation.

#### 4. Synthetic Simulation

In order to illustrate how a particular geometrical resistivity structures is resolved in the ERT data inversion and then to improve the understanding of the inverted resistivity profiles, a synthetic simulation approach is proposed to model the electrical behaviour of complex structures. In this simulation, the Res2DMod software package [14] was used to compute the apparent resistivity pseudosection thanks to a geometrical model of different resistivity bodies. This method is based on finite difference modeling schemes [15]. The synthetic apparent resistivity data were then inverted with Res2DInv in order to verify how the software recovers the initial model. We used the same parameters than

field survey: Wenner array, 5 m electrode spacing and the maximum  $n$ -level is  $15a = 75$  m.

We present two examples related to the two main structural aspects observed on our data sets: one with horizontal layers characterised by the Bittit 4 section, the other one with a vertical structure surrounded by horizontal layers characterised by the Bittit 2 section. In both cases, the final model was constructed after several steps in order to fix the best values of some parameters like number of layers, depth, thicknesses, resistivities. Each time the simulation results were compared to surveyed sections. At the end, we choose the model that gives a resistivity pseudosection that correctly fit the data. We limit our investigation to simple structures and limited range of resistivities. As a consequence, only the major resistivity anomalies of the data sections are taken into account.

**4.1. The “Bittit 4” Model.** The inverted section of the Bittit 4 data shows almost tabular layers with contrasted resistivity values (Figure 5). The first step of this simulation was to determine the number of layers necessary to fit the best with the Bittit 4 pseudosection. The choice of three horizontal layers with contrasted resistivities was based on lithological informations of the study area. It was confirmed by numerical tests that additional layers did not improve the results. Thus, resistivity value of  $10 \Omega\text{m}$  corresponds to the electrical behaviour of soil when located at the surface and of saturated travertine at depth. Resistivity value of  $100 \Omega\text{m}$  corresponds to travertine or wet limestone. Resistivity value of  $1000 \Omega\text{m}$  represents Liassic carbonates and basalt lavas.

The model corresponding to the Bittit 4 profile consists of a travertine layer of about 28 m thick, locally overlain by thin superficial structures, alternating conductive and resistant materials in order to take into account the thin superficial resistivity anomalies observed on the Bittit 4 data section. We showed that this thickness value does not modify significantly the resulting pseudosection when variations of  $\pm 2$  m are considered. This travertine

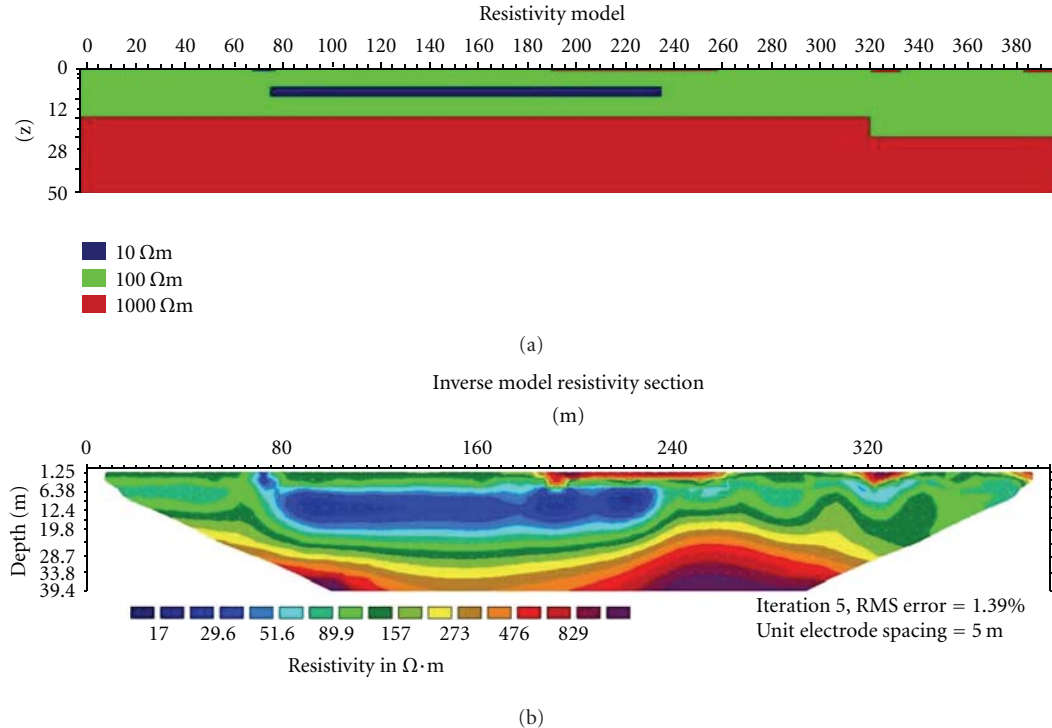


FIGURE 7: Synthetic modelling of horizontal structures corresponding to the “Bittit 4” model. (a) Input geometries and resistivities of the model; (b) image of the model obtained from inversion of synthetic data calculated for the model given in (a).

lies on the non-fractured Liassic limestone of high resistivity. As the computed apparent pseudosection does not fit well the low resistivity anomaly located approximately at 770 m of elevation, that is, 15 to 20 m depth (Figure 7), it was necessary to insert a low-resistivity layer that represents a travertine layer with higher water content.

Many depths have been tested to define the place of this very conductive zone in the travertine layer, from its basement to 10 m depth. Finally the depth of 12 m has appeared to give the best fit. Some thicknesses have also been tested and led to a 4 m thick layer.

The Res2DInv inversion of the synthetic data (Figure 7(b)) is globally in good agreement with the inversion of the original data pseudosection (Figure 5), even if some anomalies of small extension of the data are not well reproduced by the model, particularly on the border part of the profile. Nevertheless, this model confirms that the data can be explained by almost continuous horizontal layers, with resistivity values representative of each lithological formation observed in this area. It can also be noticed that the resistivity values and depth of the different layers are well recovered by the Res2DInv inversion, even if the interfaces between layers are smoothed. However, the geometrical interfaces are deformed by the inversion, probably because of edge effect. This must be taken into account in the interpretation of inverted resistivity profiles.

**4.2. The “Bittit 2” Model.** The inverted section of the Bittit 2 data shows more complex geometry than in the Bittit 4

profile, with subhorizontal layers intersected by one vertical conductive structure (Figure 5). We choose to model this particular pseudosection because it shows vertical conductive features of major interest in our study and because it is the less heterogeneous one with this kind of structure.

The choice of the number of layers and their resistivity is based on the results obtained for the Bittit 4 section. Their thicknesses were adjusted in order to fit the best with the Bittit 2 data. A vertical feature has been added to simulate a conductive zone such as a fractured structure (Figure 8). Different parameters were tested: the resistivity value, the width, the depth of the top of the fault, and its dip. A resistivity value of 40 Ωm for the fault zone has seemed to be the best value to model the data. Indeed, lower resistivity produced a high-conductivity zone at the base of the inverted model that is not representative of the real data, while greater resistivity values produced a resistant block. A first value of the width of the fault zone was determined from the result of the inverted section of the data and then adjusted by comparison between the model and the data. A variation less than  $\pm 4$  m does not significantly modify the results. The depth of top of the fault zone was set to 8 m, underlying the conductive superficial layer, almost continuous along the profile.

Finally, the “Bittit 2” model shows three layers increasingly resistive with depth like that in the Bittit 4 model. The vertical structure offsetting the deep resistant layer can be simulated by a vertical layer of 25 m width with resistivity of 40 Ωm starting from 8 m depth (Figure 8), interpreted as a fractured zone with high conductivity.

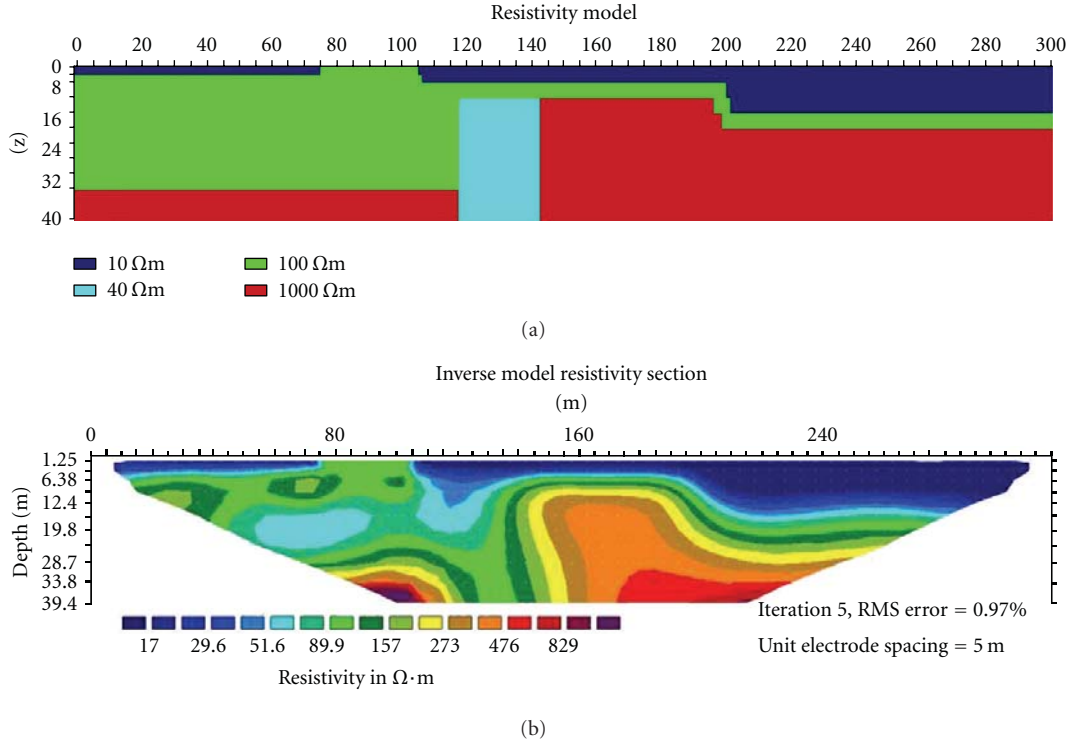


FIGURE 8: Synthetic modelling of horizontal layers and a single fracture corresponding to the “Bittit2” model. (a) Input geometries and resistivities of the model; (b) image of the model obtained from inversion of synthetic data calculated for the model given in (a).

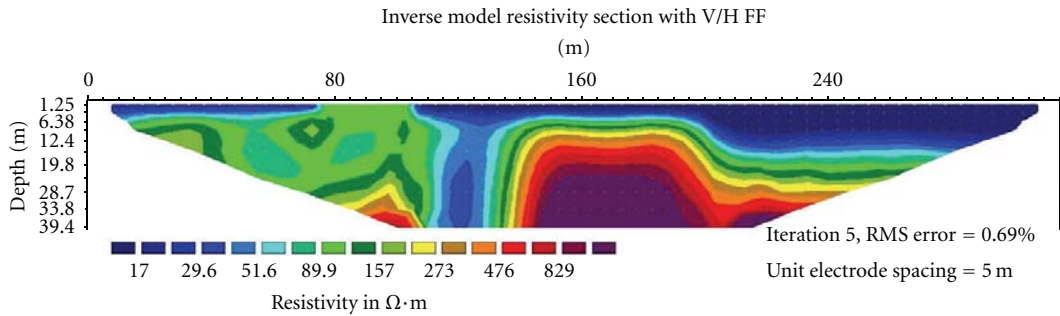


FIGURE 9: Vertical flatness filter applied on the inversion of the computed pseudosection of the Bittit 2 model.

The aim of these synthetic simulations was to constrain the interpretation of the results provided by Res2DInv. It must be kept in mind that different resistivity models can give very similar pseudosections. We made use of this synthetic simulation to also validate the usefulness of the V/HFF Res2DInv filter in the processing (Figure 9). The inversion of the pseudosection model corresponding to the Bittit 2 data, applying the V/HFF filter with a dumping factor of 4, shows that the geometry of the vertical fault zone is better determined, with a representation of the dip of the fault closer to the true vertical one.

Finally, we have seen that synthetic simulation allowed us to obtain the general geometric structures of the underground to better interpret our data set, even if some parameters like dip of vertical features can not be precisely

estimated and to check that resistivity anomalies observed on the inversion result are due to geological structures and not to inversion effects.

## 5. Interpretations and Discussion

The results obtained in this study confirm the efficiency of the electrical tomography in hydrogeological application and, in our case, to the location of the water paths between the TMA and the Bittit Spring area. Several resistivity features were observed that can be classified into two sets: horizontal layers located at shallow depth with low resistivity and more complex and contrasted resistivity pattern at depth. These features are interpreted either in terms of lithology or in terms of water content. The borehole associated to

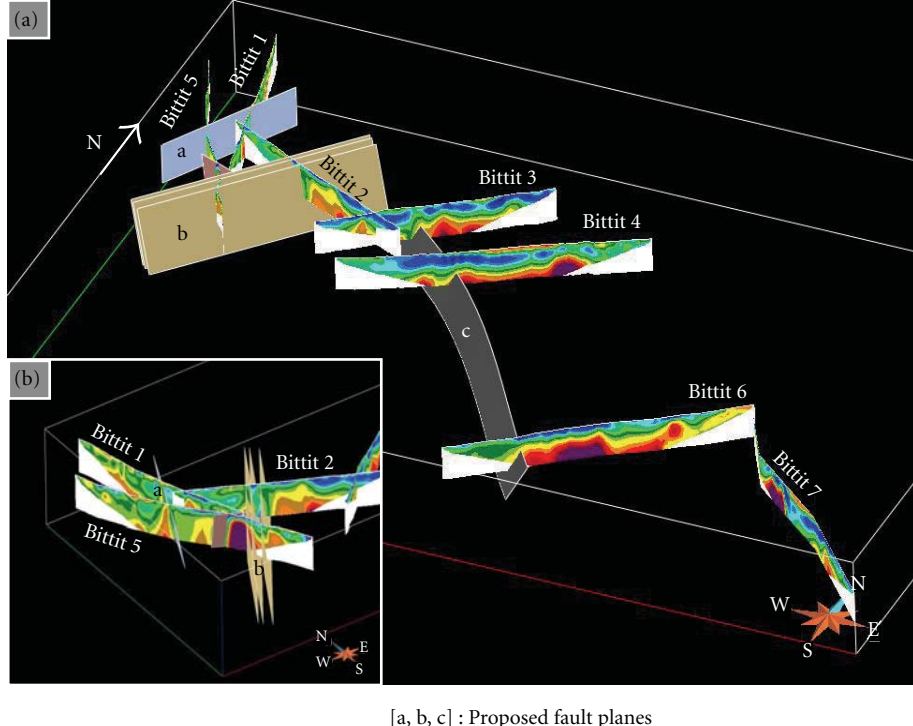


FIGURE 10: GOCAD 3D visualization of ERT Profiles sections and some interpolated fractures planes.

the electrical panel provides a strong constrain for our interpretation to determine the resistivity range for main lithologies. Variations inside each main facies were associated to changes in water saturation and/or porosity variations. Localised fracturing or a change in lithology properties induces these local variations. The deep parts ( $>15$  m) of the electrical sections display important lateral variation in resistivity over a short distance. These variations limit blocks with contrasted resistivity: this setup is interpreted as geological blocks limited by subvertical borders. These later structures are mainly located at depth and contrasts with shallow horizontal levels with low resistivity. By consequence, subvertical zones affecting the deep parts of the investigated area are sealed by the tabular units and are interpreted as fault zones. This observation is consistent with surface observations that show no significant faults at surface.

A simple structural map (Figure 11) was drawn based on correlations of different structures identified on the resistivity sections (shallow low-resistivity layers and lateral resistivity variations). The spatial consistency of the structures was first checked using the geomodeler GOCAD (Figure 10). In particular, we validated the fit of the resistivity units at the intersection between two resistivity sections, as for instance at the intersection between Bittit 1 and Bittit 2 profiles that revealed the presence of the conductive structure. The different inferred faults were modelled into GOCAD to better constrain the interpolation between the distant resistivity profiles (Figure 10).

To determine the water path, we reported on map (Figure 11) detected resistivity features with points for deep

lateral changes and with grey polygons for low-resistivity layer. This map reveals a large shallow layer of low resistivity that becomes thinner from the eastern part of the survey to the western part where it arises to the surface. It disappears on the north border, close to the Bittit Spring. The resistivity values are consistent with porous travertine filled by water. This interpretation fit to field observations that pointed out large amount of travertine in the area of the Bittit Spring. The subvertical faulted zones are organised into three trends: ENE-SWS, NW-SE, and E-W directions. These faulted features are deep and are never observed at surface. They often limit blocks with medium resistivity values. Taken into account the resistivity values, these faulted zones do not correspond to very active water paths. They form a network of uplifted and collapsed blocks. The NE-SW direction corresponds to a main trend that affects the TMA. The NW-SE and EW directions were observed on the outcrops of the northern border of the TMA (Figures 11 and 13).

To sum up, the ERT survey showed a subhorizontal conductive zone attributed to porous and saturated travertine that suggests a main drainage layer at shallow depth, mainly located at the south-east of the spring. Furthermore, vertical features seem not to be main water drains. Other geological argues lead to the same conclusions. One of the faults extracted from the Bittit 5 profile could supply the Bittit Spring by extrapolating the fault plane toward NE (Figures 11 and 12). However, the Bittit 5 profile is located on a hill, 50 m higher than the spring. If this fault was draining, water should emerge at the intersection between topography and the fault plane on the hill slope, but no source rises at this

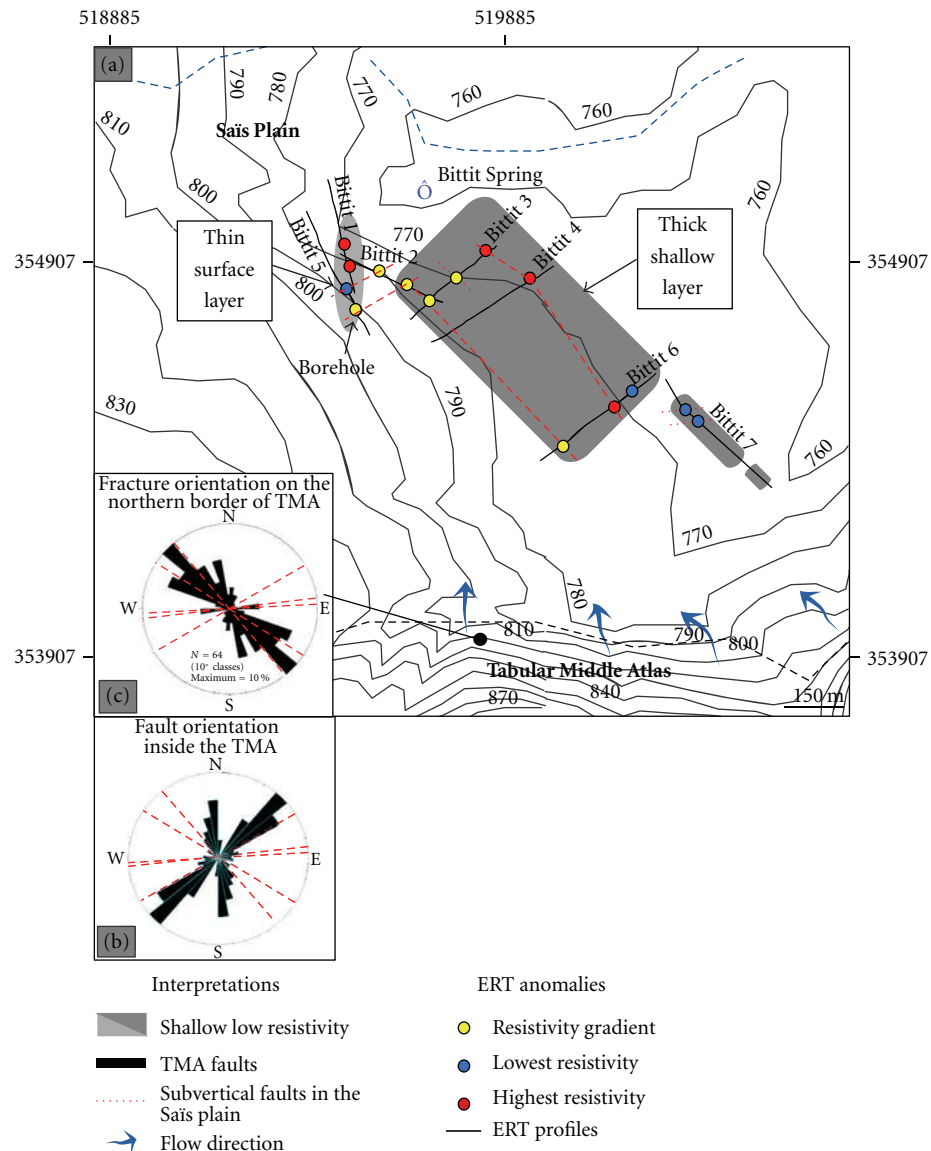


FIGURE 11: Map of resistivity anomalies detected from ERT, interpreted faults, and conductive zones (a). Note that the NW-SE fault set is also observed on the northern border of TMA (b), while the NE-SW was described inside the TMA and the Saïs plain (c).

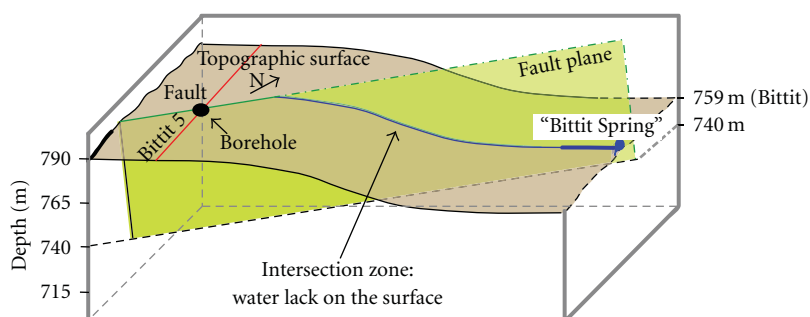


FIGURE 12: Diagram showing the extrapolation of a fault plane to the Bittit Spring; The extrapolation of fault plan seen on the pseudosection predicts a water emergent on the field if it is a draining fault. However, no spring is observed on the hill confirming that this fault is dry.

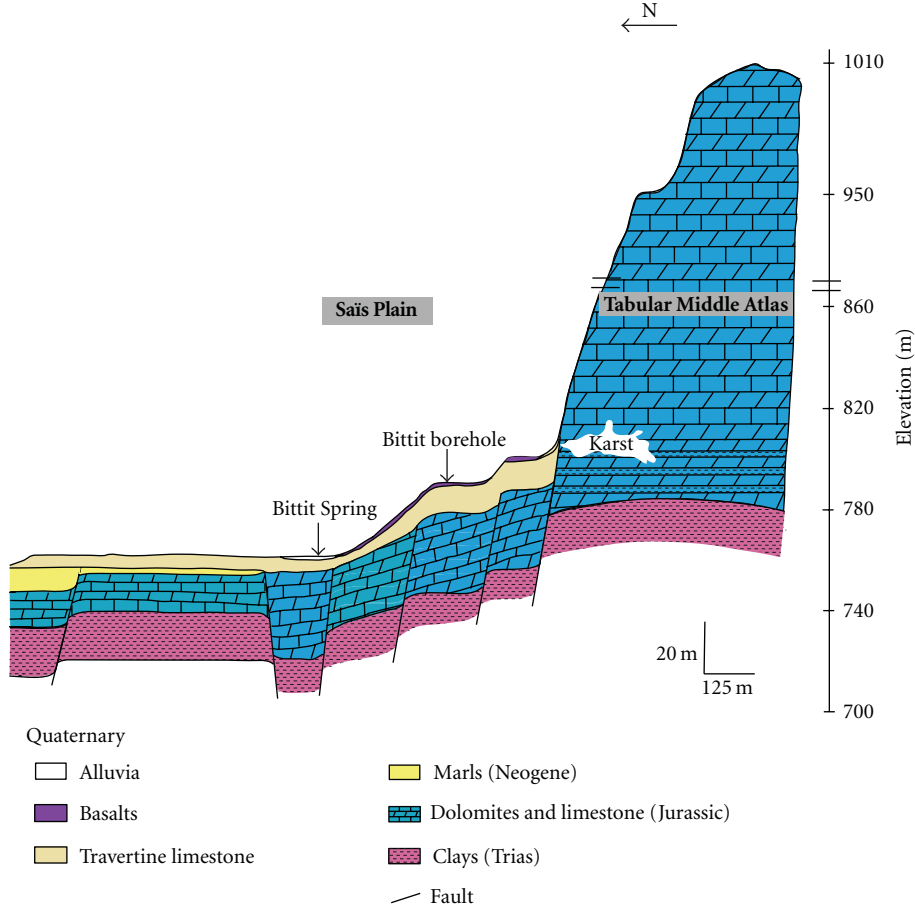


FIGURE 13: Interpretative schematic geological-cross section (AB).

point. It must be assumed that these subvertical faults are not draining features.

All these data confirm the geological evolution of the Bittit region and allow proposing a preliminary local hydrological model. The Bittit area is formed by Liassic basement at a depth around 20–40 m (Figure 13). This basement is affected by two sets of normal faults generated during two different tectonic events: One associated to a NE-SW to N-S extension and the second one to NW-SE extension. All these geological trends are seen on the electrical sections. These two tectonic phases were previously described in Morocco and belong to a main lower Triassic event [16–19].

From a hydrological point of view, we have observed water draining zones coming from the TMA to the Bittit Spring that seem to be essentially localized on a shallow subhorizontal level of porous travertine. Locally, no subvertical features seem to be major water paths. Unfortunately, the connection between the Liassic reservoir of the TMA and the deep aquifer of the Saïs plain could not be shown in this study because it seems to be deeper than the investigation depth of this ERT survey. However, it is likely that this connection is governed by complex hydrodynamic behaviour which takes into account both horizontal flow through stratification joints or karsts and flow through subvertical fractures or porous and permeable fracture zones.

## 6. Conclusion

This study aims to determine the water drains supplying the Bittit Spring, one the most important rising spring on the Saïs plain. It will constrain the hydrological connection from TMA to Saïs plain. We choose an electrical investigation taken into account for the expected investigation depth (some tens of meters) and the objects to detect (water flow). The obtained results confirm the efficiency of the electrical tomography in this kind of applications.

The TMA represents the water reservoir of the Saïs basin aquifer. One of the major questions concerns the hydraulic connections between these two systems: does it take place through vertical faults or within subhorizontal stratigraphic layers? In order to answer this question, we focused our study to the particular case of the Bittit spring, rising between the TMA and the Saïs plain.

The Electrical Resistivity Tomography investigation carried out in this area consists of seven profiles covering an area of 5 km<sup>2</sup>. The inversion of these pseudosections was performed using Res2DInv software. A Vertical to Horizontal flatness filter was applied to discriminate subvertical resistivity anomalies that can be associated to geological and hydrological features. A synthetic modelling of two of these pseudosections was performed to precise the main structural

aspects observed on the data sets, that is, horizontal conductive layers and vertical less conductive features. Then, a 3D view of the results allows proposing an interpretative map of the area, including subvertical features and conductive areas. It reveals the presence of horizontal drainage layer at shallow depth at SE between the TMA and the Bittit spring. The conductivity of this layer should correspond to porous and saturated travertine.

Two subvertical fault families with NE-SW and NW-SE trends respectively were identified and correspond to the known geological evolution of the region. This fractures network highlighted dislocation of the blocks of underground substratum. It was shown that the NE-SW faults can not be related to the spring and thus do not constitute draining features. These observations lead to suppose that the main water paths from the TMA to the Bittit spring are located inside a shallow horizontal layer of porous travertine. The dislocation of the deeper Liassic blocks should prevent water to flow continuously.

This electrical investigation does not allow identifying relations between the TMA and the deep aquifer of the Saïs plain, but it appears that water flow has a complex behavior taking into account all the water drain possibilities (fractures, karsts and stratification joints).

This study initiates a hydrogeophysical research in the Middle Atlas karst in order to improve water resources management and reducing aquifer vulnerability in the region.

## Acknowledgments

This work has been performed in the framework of the French-Moroccan scientific projects: EGIDE-AI Volubilis MA/07/169 and IRD-CORUS2-6153. The authors are very greatfull. They deeply thank the Agence du Bassin Hydraulique du Sebou (Fez) for their positive cooperation. They are also thankful to the Direction of Water, Ministry of Equipment (Meknes) who has executed the borehole drilling in the Bittit Spring area. They wish to thank all students and scientists who helped acquire the geophysical data.

## References

- [1] J. Martin, *Le Moyen Atlas Central Etude Géomorphologique*, Notes et mémoires du service géologique du Maroc, no. 258, Rabat, Morocco, 1981.
- [2] A. Perrone, A. Iannuzzi, V. Lapenna et al., "High-resolution electrical imaging of the Varco d'Izzo earthflow (southern Italy)," *Journal of Applied Geophysics*, vol. 56, no. 1, pp. 17–29, 2004.
- [3] E. Rizzo, A. Colella, V. Lapenna, and S. Piscitelli, "High-resolution images of the fault-controlled high agri valley basin (Southern Italy) with deep and shallow electrical resistivity tomographies," *Physics and Chemistry of the Earth*, vol. 29, no. 4–9, pp. 321–327, 2004.
- [4] A. Bentayeb and C. Leclerc, "Le Causse moyen atlasique," in *Ressources en Eaux du Maroc, Tome 3, Domaines Atlasiques et Sud-Atlasiques*, Notes et Mémoire du Service Géologique du Maroc no. 231, pp. 37–66, Rabat, Morocco, 1977.
- [5] J. Chamayou, M. Combe, B. Genetier, and C. Leclerc, "Le bassin de Meknès-Fès," in *Ressources en eaux du Maroc, Tome 2, Plaines et bassins du Maroc atlantique*, Service géologique du Maroc, A. Kabbaj and M. Combe, Eds., pp. 41–71, Rabat, Morocco, 1975.
- [6] M. Zizi, *Triassic-Jurassic Extensional Systems and their Neogene Reactivation in Northern Morocco: The Rides Prerifaines and Guercif Basin*, Notes et mémoires du service géologique du Maroc, no. 416, Rabat, Morocco, 2002.
- [7] F. Amraoui, *Contribution à la connaissance des aquifères karstiques. Cas du Lias de la plaine du Saïs et du Causse moyen atlasic tabulaire (Maroc)*, Ph.D. thesis, University Hassan II, Casablanca, Morocco, 2005.
- [8] M. H. Loke and R. D. Barker, "Least-squares deconvolution of apparent resistivity pseudosections," *Geophysics*, vol. 60, no. 6, pp. 1682–1690, 1995.
- [9] F. Nguyen, S. Garambois, D. Jongmans, E. Pirard, and M. H. Loke, "Image processing of 2D resistivity data for imaging faults," *Journal of Applied Geophysics*, vol. 57, no. 4, pp. 260–277, 2005.
- [10] D. Chapellier and J. L. Mari, "Principes de base," Cours [online] de géophysique, université de Lausanne & Institut français du pétrole, 2000.
- [11] A. Benslimane, *Etude hydrogéologique de Tigriga. Apport de la géoélectrique à la reconnaissance des potentialités hydriques dans les formations basaltiques subaffleurantes*, Ph.D. thesis, University Moulay Ismail, Meknes, Morocco, 2005.
- [12] A. Essahlaoui and A. Elouali, "Détermination de la structure géologique de la partie Sud de la plaine du Saïs (bassin de Meknès-Fès, Maroc) par la méthode géoélectrique," *Bulletin of Engineering Geology and the Environment*, vol. 62, pp. 155–166, 2002.
- [13] Geotomo software Malaysia, "Res2DInv (ver. 3.4), Copyright ©," 1995–2002, <http://www.geoelectrical.com>.
- [14] M. H. Loke, "Res2DMod (ver. 3.0) [software], Copyright ©," 1995–2008.
- [15] I. F. Louis, F. I. Louis, and A. Grambas, "Exploring for groundwater conditions in hardrock environments by resistivity imaging methods. Synthetic simulation approach and case study example," *Journal of Electrical and Electronics Engineering*, pp. 1–14, 2002.
- [16] L. Ait Brahim, P. Chotin, S. Hinaj et al., "Paleostress evolution in the Moroccan African margin from triassic to present," *Tectonophysics*, vol. 357, no. 1–4, pp. 187–205, 2002.
- [17] M. L. Arbolea, A. Teixell, M. Charroud, and M. Julivert, "A structural transect through the High and Middle Atlas of Morocco," *Journal of African Earth Sciences*, vol. 39, no. 3–5, pp. 319–327, 2004.
- [18] K. Bargach, P. Ruano, A. Chabli et al., "Recent tectonic deformations and stresses in the frontal part of the Rif Cordillera and the Saïss basin (Fes and Rabat regions, Morocco)," *Pure and Applied Geophysics*, vol. 161, no. 3, pp. 521–540, 2004.
- [19] F. Gomez, M. Barazangi, and M. Bensaïd, "Active tectonism in the intracontinental Middle Atlas Mountains of Morocco: synchronous crustal shortening and extension," *Journal of the Geological Society*, vol. 153, no. 3, pp. 389–402, 1996.

## Research Article

# Experimental Studies on the Changes in Resistivity and Its Anisotropy Using Electrical Resistivity Tomography

Tao Zhu, Jian-Guo Zhou, and Jin-Qi Hao

*Institute of Geophysics, China Earthquake Administration, Beijing 100081, China*

Correspondence should be addressed to Tao Zhu, [zxl\\_tao@yahoo.com.cn](mailto:zxl_tao@yahoo.com.cn)

Received 10 March 2011; Revised 10 July 2011; Accepted 8 August 2011

Academic Editor: Sabatino Piscitelli

Copyright © 2012 Tao Zhu et al. This is an open access article distributed under the Creative Commons Attribution License, which permits unrestricted use, distribution, and reproduction in any medium, provided the original work is properly cited.

Three measuring lines were arranged on one of free planes of magnetite cuboid samples. Apparent resistivity data were acquired by MIR-2007 resistivity meter when samples were under uniaxial compression of servocontrol YAW-5000F loading machine in laboratory. Then we constructed the residual resistivity images using electrical resistivity tomography (ERT) and plotted the diagrams of apparent resistivity anisotropy coefficient (ARAC)  $\lambda^*$  and the included angle  $\alpha$  between the major axis of apparent resistivity anisotropy ellipse and the axis of load with pressure and effective depth. Our results show that with increasing pressure, resistivity and the decreased (D region) and increased (I region) resistivity regions have complex behaviors, but when pressure is higher than a certain value, the average resistivity decrease and the area of D region expand gradually in all time with the increase of pressure, which may be significant to the monitoring and prediction of earthquake, volcanic activities, and large-scale geologic motions. The effects of pressure on  $\lambda^*$  and  $\alpha$  are not very outstanding for dry magnetite samples.

## 1. Introduction

The striking changes in electrical resistivity and its anisotropy were widely observed before earthquake, mine earthquake, volcanic activities, and geologic motions [1–12]. In order to address the change characteristics of resistivity and its anisotropy, many investigators conducted a plenty of experiments on rock samples under compression and during fracture, shear, and frictional sliding in lab [13–25] and theoretic studies [26–30]. Experimental results reported by Brace et al. [13] and Brace and Orange [14–16] in lab showed that striking changes in electrical resistivity were observed for a variety of igneous and sedimentary crystalline rocks when water-saturated crystalline rocks were stressed to fracture. Resistivity decreased by as much as an order of magnitude. Most of the change occurred at stresses above half the fracture stress. The electrical resistivity of hematite decreased gradually with increasing shock pressure to 440 kb and decreased discontinuously to less than  $1 \Omega \text{ cm}$  from several tens of  $\Omega \text{ cm}$  at pressure of 440–520 kb [18], and that of a saturated granite during frictional sliding showed clear variations premonitory to the occurrence of stick-slip: resistivity decreased by a few percent with increasing shear stress; the

minimum coincided with a sudden release of shear stress of a few bars, accompanied by an immediate return of resistivity [17]. Morrow and Brace [19] and Yamazaki [31, 32] reported that the electrical resistance of tuffs changed very largely, particularly for small strains and could be applied to earthquake prediction [1]. Studies on the changes in resistivity anisotropy were conducted by Chen et al. [33] firstly in lab. They used the water-saturated crystalline rock samples and arranged three measuring lines parallel to, perpendicular to, and intersecting at the angle of  $45^\circ$  with maximum principle stress axis on one of its free planes, and studied the relations between apparent resistivity anisotropy and pressure. Considering the effects of groundwater, An et al. studied the changes in resistivity and its anisotropy with pressure in the presence of feed water [34]. In order to recognize the expansion of fissure with stress, Chen et al. [22–25] studied the water-saturated granite samples and man-made samples under uniaxial compression, triaxial compression with low confining pressure, and frictional sliding. This previous work played very important role in recognizing and understanding the change behaviors of resistivity and its anisotropy with pressure, but they had to analyze the curves of resistivity and its anisotropy with pressure because of only a few electrodes

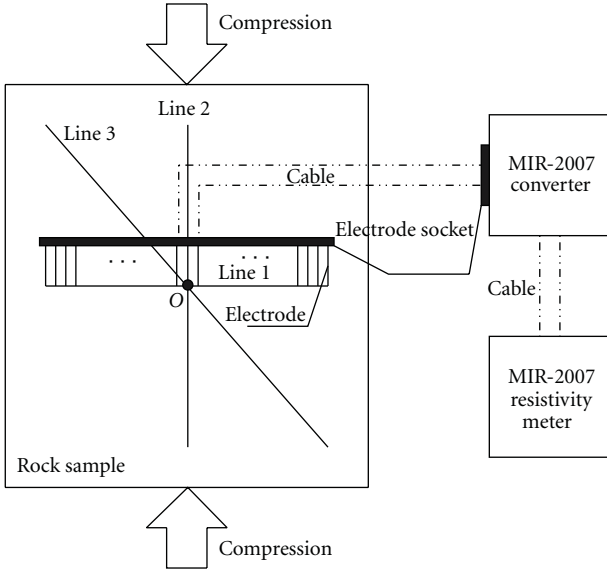
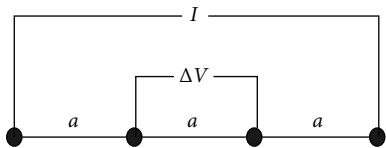


FIGURE 1: Sketch of test system.

FIGURE 2: Sketch of Wenner- $\alpha$  array.  $I$  indicates the intensity of current between two current electrodes  $A$  and  $B$ .  $\Delta V$  indicates the potential difference between two potential electrodes  $M$  and  $N$ .

designed on one measuring line. In order to study the changes in resistivity and its anisotropy with pressure, we use MIR-2007 resistivity meter to acquire apparent resistivity data of dry magnetite samples in lab. In resistivity measurements, 37–120 electrodes and 12–30 “ $n$ ” factors [35] and Wenner- $\alpha$  array are used, and 210–1205 apparent resistivity measurements are acquired. We construct the resistivity images at each pressure value using ERT and plot the diagrams of  $\lambda^*$  and  $\alpha$  at each effective depth. Then the changes in resistivity and its image and anisotropy with pressure and depth are studied. We find that when the pressure is higher than a certain pressure, average resistivity will decrease, and the area of D region will expand gradually, and most of  $\lambda^*$  and  $\alpha$  change slightly with the increase of pressure.

## 2. Experiments

**2.1. Samples.** Two cuboid magnetite samples used in this study were collected in Yinan, Shandong province, China. Physical properties and geometric dimensions of specimens were listed in Table 1.

They mainly consist of magnetite (larger than 60%), which leads to their good conductivity; so it is possible to conduct resistivity measurements easily. Their compression planes are the plane of  $31.8 \times 22.0$  cm for sample YN1 and of  $29.0 \times 26.0$  cm for sample YN2 in dimension.

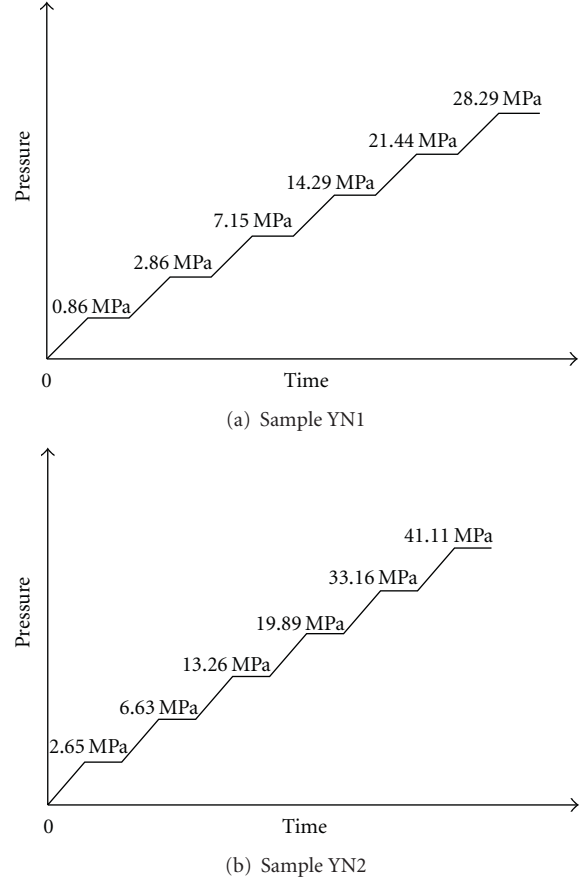


FIGURE 3: The loading curves of samples.

**2.2. Experimental System.** The experimental system used is shown in Figure 1. The uniaxial servocontrol YAW-5000F loading machine (<http://shijin.shuoyi.com/shtml/shijin/product/57fd78bf28f0244d.html>) manufactured by Jinnan Shijin Group Co. Ltd. was used for axial load. Three measuring lines are arranged on one of free planes. Line 1 and 2 are perpendicular and parallel to the axis of load, and Line 3 intersects this axis at the angle of  $45^\circ$  (Figure 1). Three measuring lines all intersect at the point  $O$  which almost locates the center of the free plane. Copper wires spot welded on the free planes are used as electrodes of resistivity measurements. The parameters of measuring lines of two samples are listed in Table 2. MIR-2007 resistivity meter used in this experiment was specially designed for resistivity measurement of rock sample in lab by Beijing Geological Instrument Factory (<http://bjdzyqc.shuoyi.com/shtml/bjdzyqc/index.htm>). The input impedance of the meter is about  $4104\text{ M}\Omega$ , and its accuracy of potential measurement is about 0.15%. Wenner- $\alpha$  array (Figure 2) was used in data acquisition.

**2.3. Loading Curves and Data Acquisition.** The samples were compressed by uniaxial load (Figure 1). Their loading curves are shown in Figure 3. Resistivity measurements were conducted along measuring lines one by one when pressure increased to 0, 0.86 MPa, 2.86 MPa, 7.15 MPa, 14.29 MPa, 21.44 MPa, and 28.29 MPa at uniform rate of  $1.43 \times 10^{-2}$  MPa/s for sample YN1 and to 0, 2.65 MPa, 6.63 MPa,

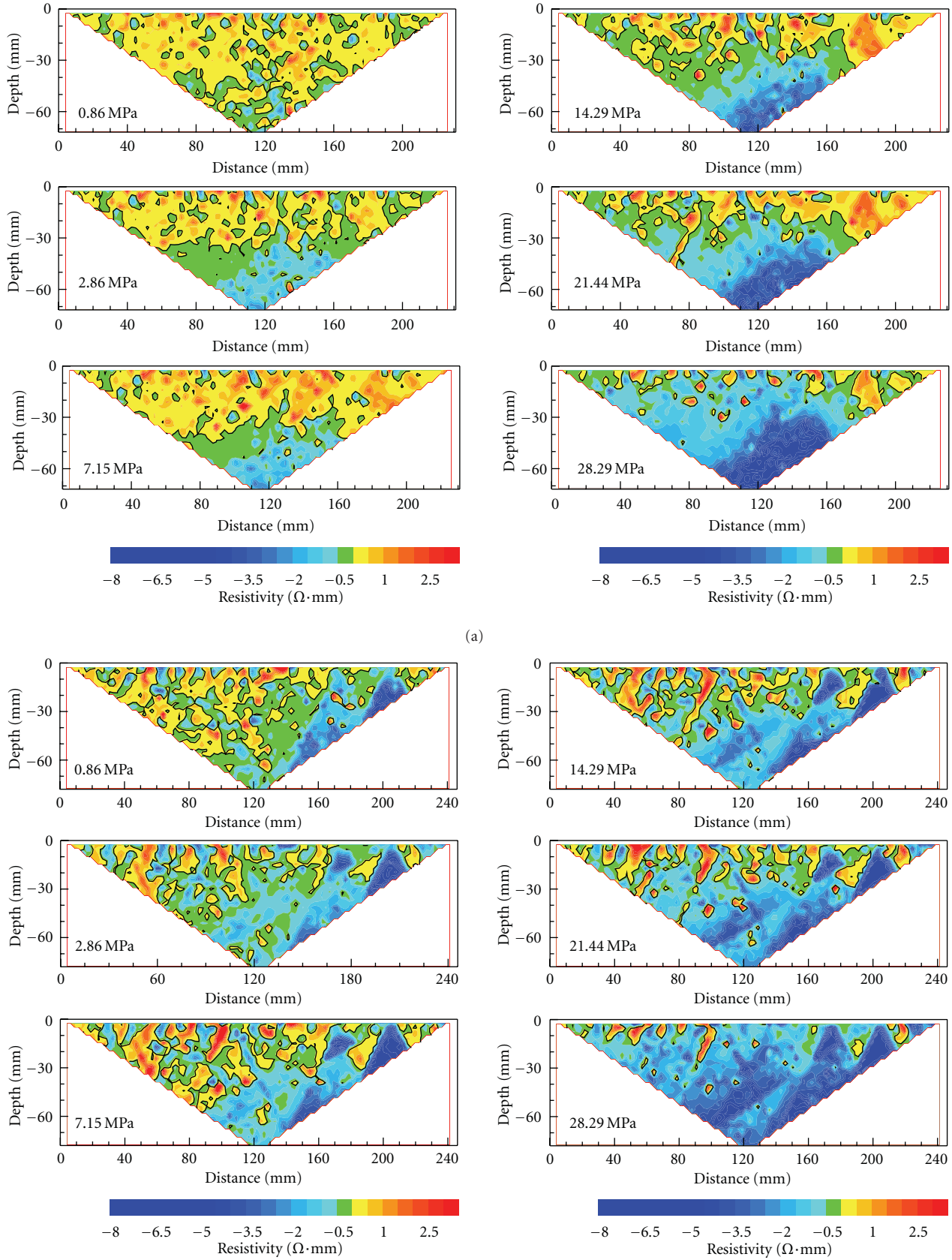


FIGURE 4: Continued.

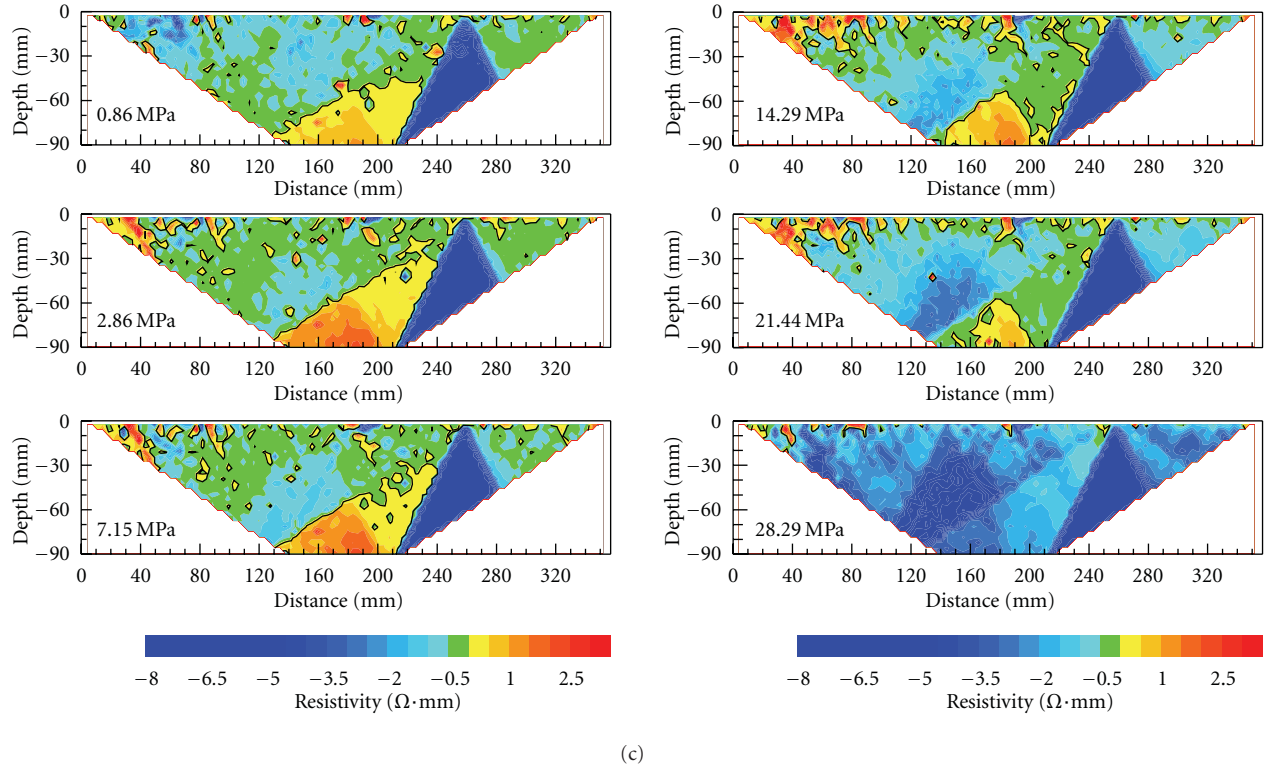


FIGURE 4: The residual resistivity images of sample YN1. (a) Line 1, (b) Line 2, and (c) Line 3.

TABLE 1: Physical properties and geometric dimensions of specimens.

Sample no.	Density (g/cm <sup>3</sup> )	Dimension (cm)	Modal analysis
YN1	5.04	34.0 × 31.8 × 22.0	64 Magnetite, 29 Quartz, 7 Feldspar
YN2	5.07	34.0 × 29.0 × 26.0	68 Magnetite, 27 Quartz, 5 Feldspar

TABLE 2: Parameters of measuring lines.

ML	NE	SE	NF
Sample YN1			
Line 1	78	3 mm	24
Line 2	83	3 mm	26
Line 3	120	3 mm	30
Sample YN2			
Line 1	37	5 mm	12
Line 2	52	5 mm	17
Line 3	66	5 mm	21

Note: ML, NE, SE, and NF indicate measuring line, number of electrode, spacing of electrode, and “n” factors, respectively.

13.26 MPa, 19.89 MPa, 33.16 MPa, and 41.11 MPa at  $2.65 \times 10^{-2}$  MPa/s for sample YN2 and remained constant at each value. It took about 3 hours for sample YN1 and 1.5 hours for sample YN2 for resistivity measurement at each pressure value. In the meantime, time-lapse strain was recorded. To our regret, the strain curves remained straight lines throughout the experiment. We thought that the pressure

was not enough high to lead to the measurable deformation recorded by our strain gauge.

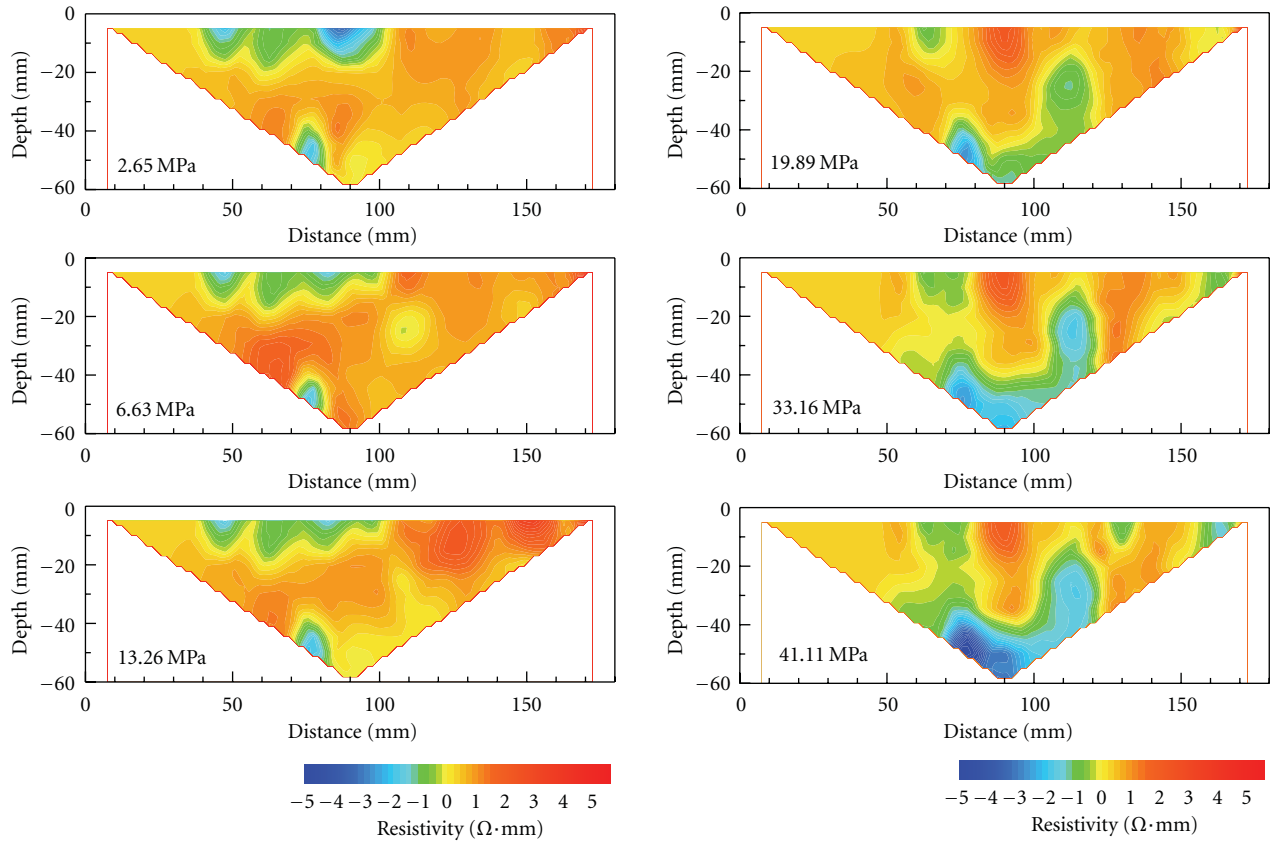
### 3. Results and Analysis

**3.1. Residual Apparent Resistivity Image (RARI).** Residual apparent resistivity values were calculated via

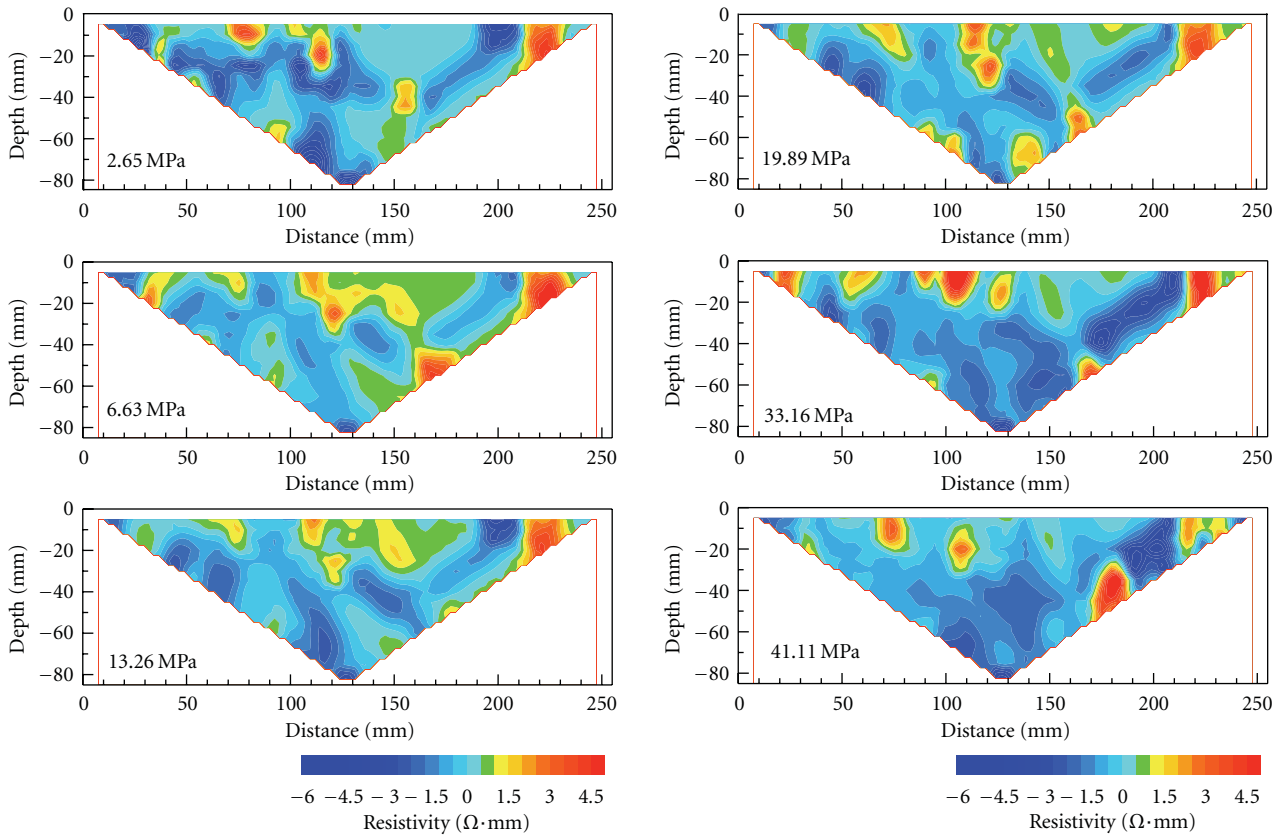
$$\rho_{NR} = \rho_N - \rho_0, \quad (1)$$

where  $\rho_{NR}$  and  $\rho_N$  represent the residual and measured apparent resistivity value at the pressure value of  $N$  MPa, and  $\rho_0$  indicates the apparent resistivity measurement at zero pressure.  $N$  takes 0.86 MPa, 2.86 MPa, 7.15 MPa, 14.29 MPa, 21.44 MPa, and 28.29 MPa for sample YN1 and 2.65 MPa, 6.63 MPa, 13.26 MPa, 19.89 MPa, 33.16 MPa, and 41.11 MPa for sample YN2.

As are shown in Figures 4 and 5, the RARIs along three measuring lines have different change behaviors with pressure when the pressure is smaller than 7.15 MPa for sample YN1 (Figure 4) and 6.63 MPa for sample YN2 (Figure 5). Figure 4 indicates that the RARIs could be divided simply into D (blue to green zone) and I (yellow to red zone) region.



(a)



(b)

FIGURE 5: Continued.

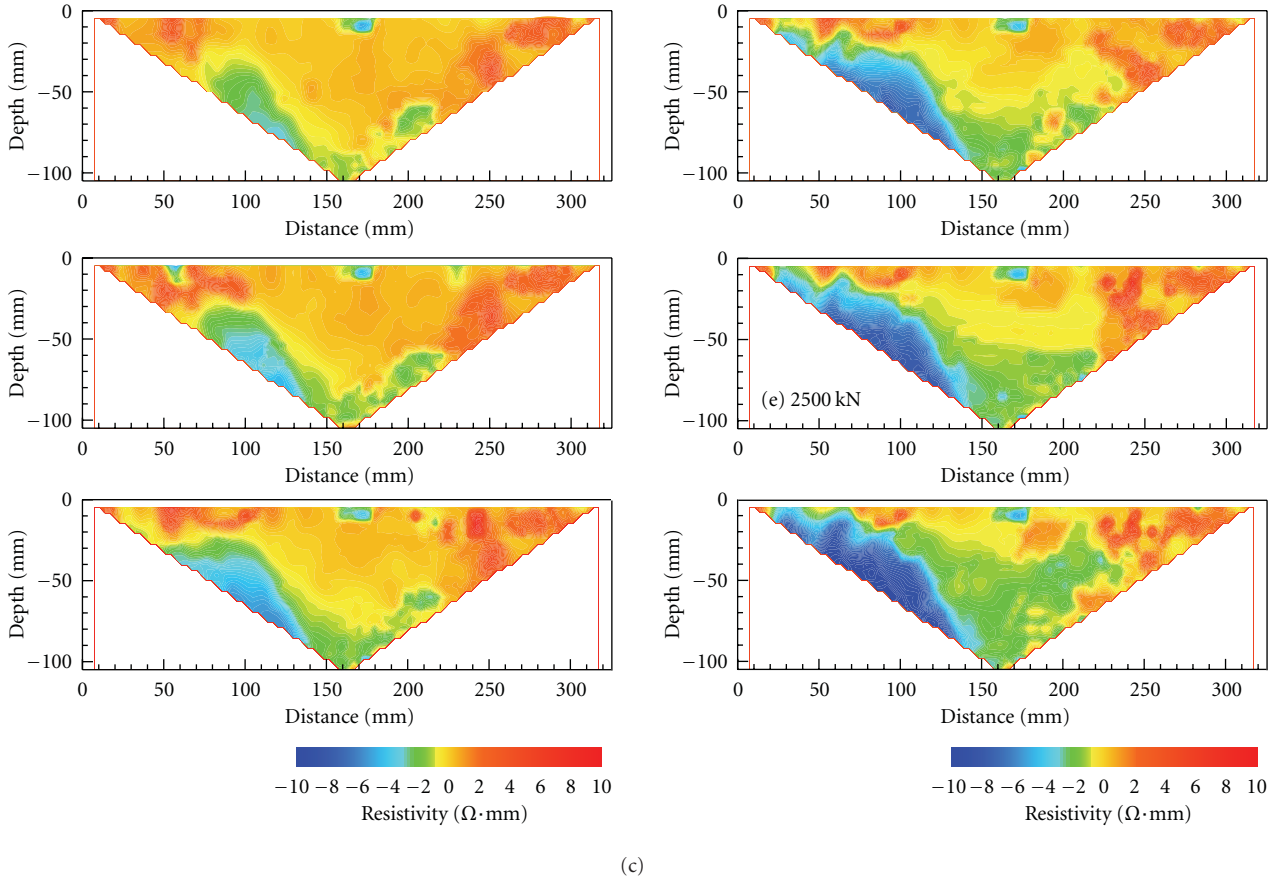


FIGURE 5: The residual resistivity images of sample YN2. (a) Line 1, (b) Line 2, and (c) Line 3.

With the increase of pressure, the average electrical resistivities of D region in Figure 4(a) increase (i.e., the average decreased magnitude becomes smaller) (compared the RARIs at 0.86 MPa and 2.86 MPa) firstly and then decrease (i.e., the average decreased magnitude becomes larger), (compared the RARIs at 2.86 MPa and 7.15 MPa), while those of I region in Figure 4(a) decrease firstly and then increase. The area of D region expands strikingly firstly and then almost remains constant, while that of I region reduces outstandingly firstly and then almost keeps constant. The electrical resistivities of D region in Figure 4(b) decrease in all time, and those of I region decrease firstly and then increase. The area of D region expands firstly and then reduces. The electrical resistivities of D and I region in Figure 4(c) both increase firstly and then decrease. The area of D region reduces firstly and then almost remains constant while that of I region increases firstly and then almost remains constant. With the increase of pressure from 2.65 MPa to 6.63 MPa, the electrical resistivities of D and I regions in Figures 5(a) and 5(b) all increase slightly. The area of D region expands slightly, and that of I region reduces slightly in Figure 5(a) while it is going in the opposite direction in Figure 5(b). The electrical resistivities of D and I region in Figure 5(c) both decrease slightly. The area of D region expands slightly while that of I region reduces slightly. When the pressure is larger than 7.15 MPa

for sample YN1 (Figure 4) and 6.63 MPa for sample YN2 (Figure 5), the electrical resistivities of D regions in Figures 4 and 5 all decrease gradually while those of I regions probably have complex change behaviors with the increase of pressure. For instance, they decrease firstly (As shown in the RARIs at 6.63 MPa and 13.26 MPa in Figure 5(a)), then increase (As shown in the RARIs at 13.26 MPa and 19.89 MPa in Figure 5(a)) and decrease gradually, at last (As shown in the RARIs at 19.89 MPa, 33.16 MPa, and 41.11 MPa in Figure 5(a)). However, the areas of D regions in Figures 4 and 5 all expand gradually and those of I regions are in opposite direction.

Our results show, as the previous investigators [14–19] reported, that electrical resistivities of rocks have complex behaviors with the increase of pressure. However, due to only two electrodes used in (volume) resistivity measurements, insufficient resistivity measurements could be used to construct resistivity image, and only the curves of resistivity versus pressure could be used to study the changes in resistivity with pressure in these previous studies. In this paper, 37–120 electrodes and 12–30 “*n*” factors are used, and then 210–2205 resistivity measurements are acquired, which allow us to construct resistivity images easily we have the chance to study the changes in resistivity and its image with pressure in laboratory. Our results indicate that when pressure increases to a certain value, with the increase of pressure, the electrical

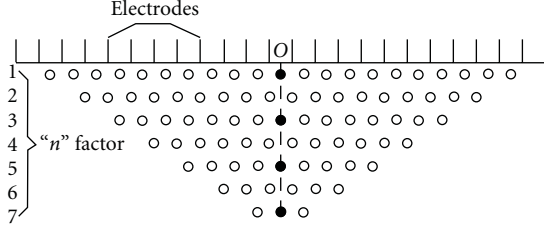


FIGURE 6: The illustration of extracting apparent resistivity set for Wenner- $\alpha$  array. In the studies on apparent resistivity anisotropy at point O, we need the apparent resistivity data arranged along the vertical dash line. According to the characteristics of Wenner- $\alpha$  array, the apparent resistivity measurements could be extracted every one “n” factor. That is, the apparent resistivity measurements just corresponding to odd “n” factors and on the vertical dash line will be extracted out. Black solid circles represent the extracted data.

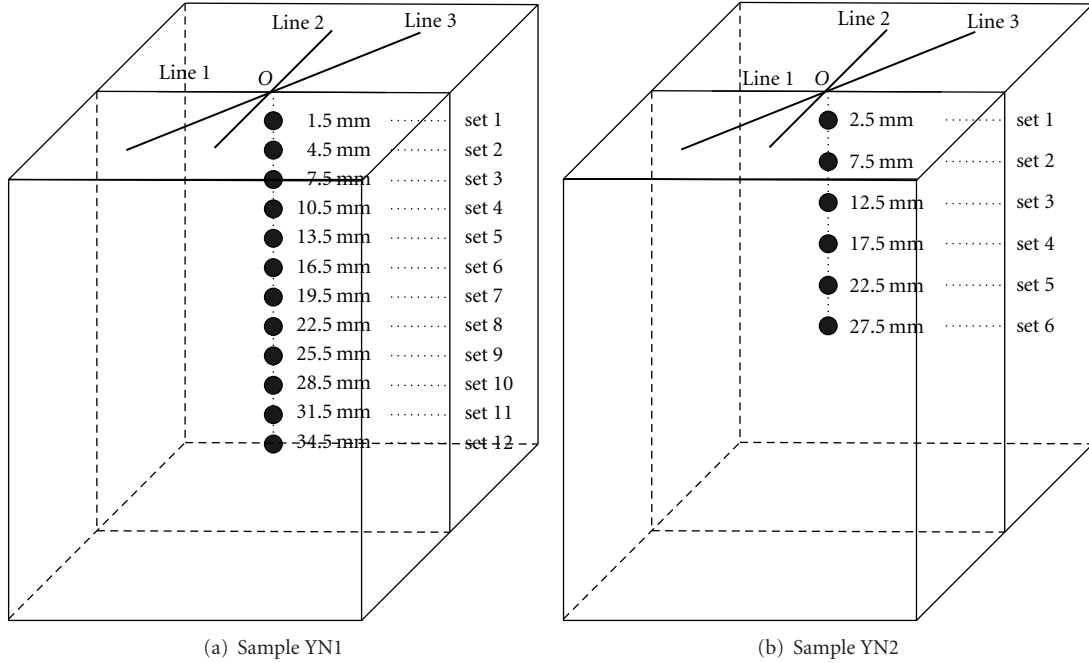


FIGURE 7: The diagram of apparent resistivity sets corresponding to effective depths. Because the effective depth of Wenner- $\alpha$  array was evaluated to be about 0.5 time of electrode spacing [36, 37], the 12 apparent resistivity sets were corresponding to the effective depths of about 1.5 mm, 4.5 mm, 7.5 mm, 10.5 mm, 13.5 mm, 16.5 mm, 19.5 mm, 22.5 mm, 25.5 mm, 28.5 mm, 31.5 mm, and 34.5 mm for sample YN1, and 6 ones were corresponding to the effective depths of about 2.5 mm, 7.5 mm, 12.5 mm, 17.5 mm, 22.5 mm, and 27.5 mm for sample YN2 according to Figure 6.

resistivities will decrease, and the area of D region will expand gradually in all time, which may be significant to the monitoring and prediction of earthquake, volcanic activities, and large-scale geologic motions.

### 3.2. Apparent Resistivity Anisotropy

**3.2.1. Data Extraction.** Studies on resistivity anisotropy require that resistivity measurements are conducted along at least two measuring lines arranged in different directions and that they must intersect at a point. For example, Mao et al. [7, 8] used the resistivity data measured along E-W and N-S trending measuring lines in studying the changes in the degree of earth resistivity anisotropy during the course of earthquake preparation. Chen et al. [22–25] designed

four measuring lines in studying the changes of apparent resistivity anisotropy in lab. In this paper, we arranged three measuring lines intersecting at point O (Figure 1), which allowed us to study the changes in apparent resistivity anisotropy at point O with pressure and depth. According to the used minimum “n” factor and the characteristics of Wenner- $\alpha$  array in resistivity measurements, we could extract 12 apparent resistivity sets (Figure 6 illustrates how to extract the apparent resistivity set.) which are corresponding to 12 effective depths (Figure 7(a)) for sample YN1 and 6 apparent resistivity sets which are corresponding to 6 effective depths (Figure 7(b)) for sample YN2. It must be noted that one apparent resistivity set contains three apparent resistivity values.

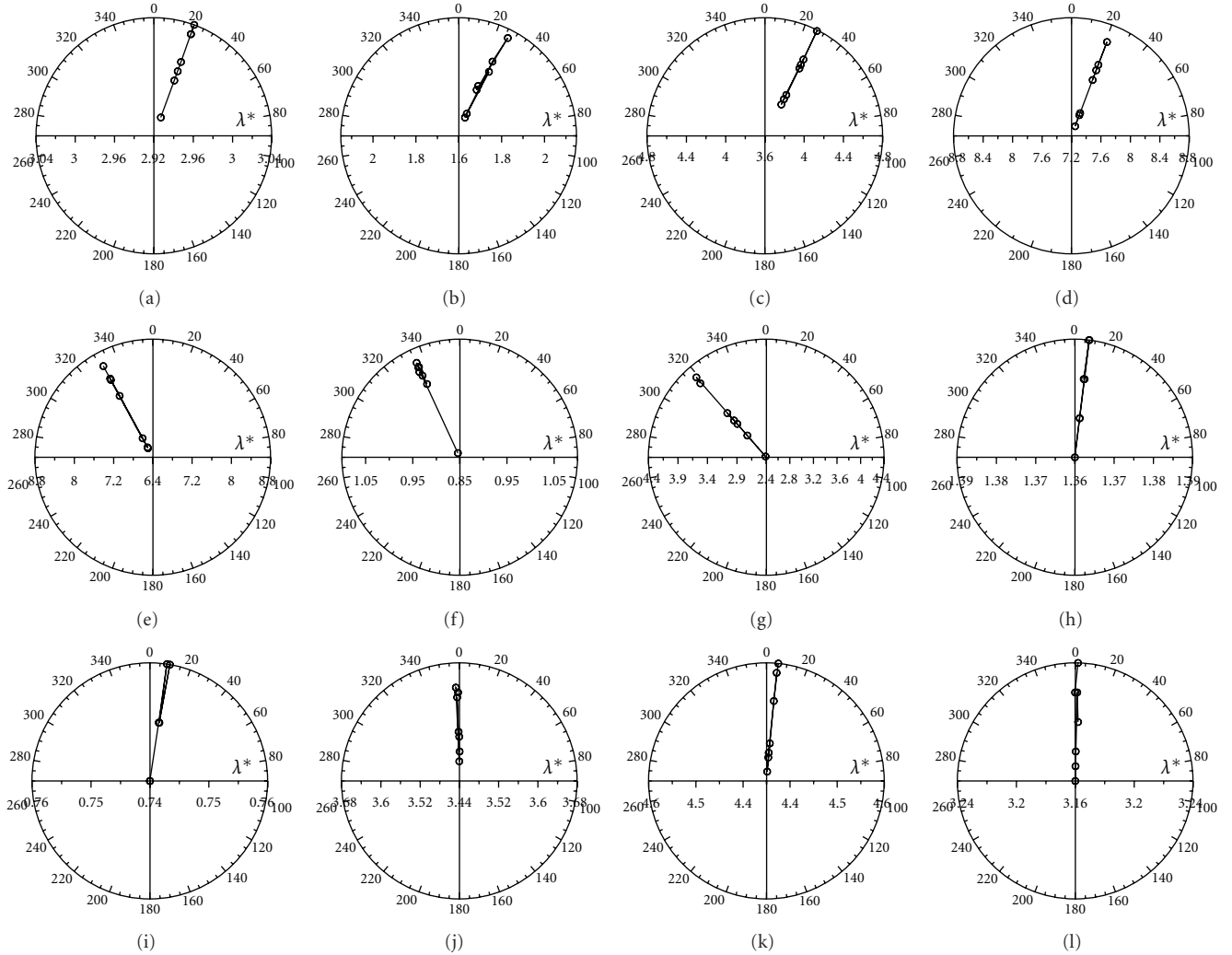


FIGURE 8: The diagrams of  $\lambda^*$  and  $\alpha$  with pressure for sample YN1. (a)–(l) represent the diagrams at the effective depths of 1.5 mm, 4.5 mm, 7.5 mm, 10.5 mm, 13.5 mm, 16.5 mm, 19.5 mm, 22.5 mm, 25.5 mm, 28.5 mm, 31.5 mm, and 34.5 mm.

**3.2.2. Apparent Resistivity Anisotropy Coefficient (ARAC).** Chen et al. [25, 33] presented the formula to calculate ARAC  $\lambda^*$

$$\begin{aligned} \lambda^{*2} &= \frac{2\sqrt{m^2 + Q^2}}{l - \sqrt{m^2 + Q^2}}, \\ l &= \rho_{s1}^{-2} + \rho_{s2}^{-2}, \\ m &= \rho_{s1}^{-2} - \rho_{s2}^{-2}, \\ Q &= 2\rho_{s3}^{-2} - l, \end{aligned} \quad (2)$$

where  $\rho_{s1}$ ,  $\rho_{s2}$ , and  $\rho_{s3}$  represent the apparent resistivities measured along three measuring lines perpendicular to, parallel to, and intersecting at the angle of  $45^\circ$  with the axis of load.

Seen from the curves of  $\lambda^*$  and  $\alpha$  with pressure and depth for sample YN1 (Figure 8), the absolute differences between the minimum and the maximum  $\lambda^*$  at 10.5 mm (Figure 8(d)), 13.5 mm (Figure 8(e)), and 19.5 mm

(Figure 8(g)) effective depths are about 1.6, 2.0, and 2.0, while those at the rest depths are all smaller than 0.5. The maximum change of  $\alpha$ , only about  $7^\circ$ , occurs at 4.5 mm depth. For sample YN2, the absolute difference between the minimum and the maximum  $\lambda^*$  at 17.5 mm (Figure 9(d)) is about 4.0, while those at the rest depths are all smaller than 1.0. The maximum change of  $\alpha$ , about  $80^\circ$ , occurs at 22.5 mm depth, but those at the rest depths are all smaller than  $5^\circ$ . These results indicate that the effects of pressure on  $\lambda^*$  and  $\alpha$  are not very striking for dry magnetite samples.

#### 4. Discussions and Conclusions

In the previous studies, the volume resistivity changes with pressure were actually studied [14–19]. It was impossible to construct resistivity image because of insufficient data; the curves of resistivity versus pressure were analyzed. In the present paper, resistivity measurements are conducted in the case of designed 37–120 electrodes and 12–30 “ $n$ ” factors, and 210–2205 resistivity values acquired are sufficient to

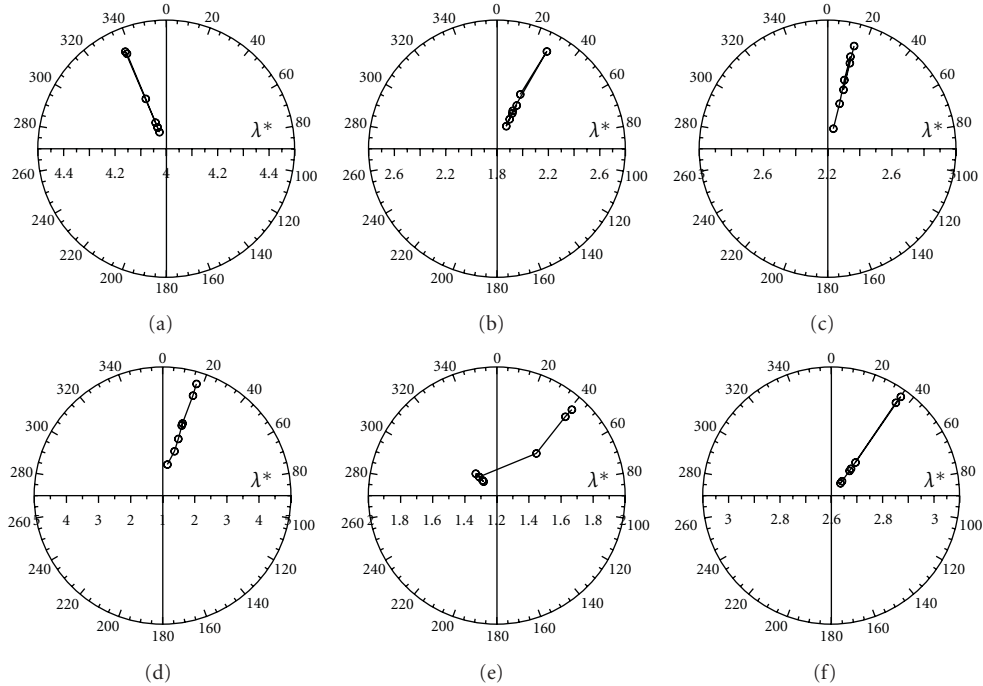


FIGURE 9: The diagrams of  $\lambda^*$  and  $\alpha$  with pressure for sample YN2. (a)–(f) represent the diagrams at the effective depths of 2.5 mm, 7.5 mm, 12.5 mm, 17.5 mm, 22.5 mm, and 27.5 mm effective depths.

allow us to use ERT to construct resistivity images which may contain much aplenty information than curves. Thus we can study the changes in not only resistivity but also in the areas of D and I region with pressure. Our results indicate that resistivity and the areas of D and I region have complex behaviors with increasing pressure when pressure is lower than a certain value such as 7.15 MPa for sample YN1 and 6.63 MPa for sample YN2 in this paper, but when pressure is higher than this value, their behaviors become very simple with increasing pressure. For instance, when pressure is higher than 7.15 MPa for sample YN1 and 6.63 MPa for sample YN2, the average resistivity of D region will decrease, and its area will expand gradually in all time with the increase of pressure. These changes were ever observed in situ by Feng et al. [9] prior to Tangshan ML 5.0 and 4.4, which probably indicate that our experimental results may be helpful and significant to the monitoring and prediction of earthquake, even for volcanic activities and large-scale geologic motions.

In the previous studies, the changes in apparent resistivity anisotropy at one or two depths with pressure were studied [22–25, 33, 34] because of at most eight electrodes and two “ $n$ ” factors used in resistivity measurements, which lead to the difficulty in the studies on its changes with depth. In this paper, as described above, at least 78 electrodes and 24 “ $n$ ” factors for sample YN1 and 37 electrodes and 12 “ $n$ ” factors for sample YN2 (Table 2) and Wenner- $\alpha$  array were used in resistivity measurements, which allow us to calculate  $\lambda^*$  and  $\alpha$  at 6 or 12 effective depths (Figure 7) and give us the chance to study their changes with pressure at more depths. Our results indicate that  $\lambda^*$  and  $\alpha$  do not change outstandingly with the increase of pressure at a certain depth. However,

the striking changes in apparent resistivity anisotropy were observed before earthquake [7, 8, 38]. We thought that we did not use water-saturated samples while the underground rocks are often in saturation because of the presence of rich groundwater. Therefore, water-saturated samples would be considered in our future study.

### Acknowledgments

The authors thank two anonymous reviewers and the editor Sabatino Piscitelli for their constructive suggestions for this paper. This research was supported by the Special Project for the Fundamental R&D of the Institute (DQJB07B09).

### References

- [1] Y. Yamazaki, “Electrical conductivity of strained rocks, 5, residual strains associated with large earthquakes as observed by a resistivity variometer,” *Bulletin of the Earthquake Research Institute, University of Tokyo*, vol. 47, p. 99, 1969.
- [2] D. Fitterman and T. Madden, “Resistivity observations during creep events at meleny Ranch, California,” *Journal of Geophysical Research*, vol. 82, no. 33, pp. 5401–5408, 1977.
- [3] W. Stopinski and R. Teisseyre, “Preliminary rock resistivity variations related to mining tremors,” *Acta Geophysica Polonica*, vol. 30, no. 4, pp. 293–320, 1982.
- [4] D. B. Jackson, J. Kauahikaua, and C. J. Zablocki, “Resistivity monitoring of an active volcano using the controlled- source electromagnetic technique: Kilauea, Hawaii,” *Journal of Geophysical Research*, vol. 90, no. 14, pp. 12–555, 1985.
- [5] J. R. Kayal and B. Banerjee, “Anomalous behaviour of precursor resistivity in Shillong area, Northeast India,” *Geophysical Journal*, vol. 94, no. 1, pp. 97–103, 1988.

- [6] T. Yukutake, T. Yoshino, H. Utada, H. Watanabe, Y. Hamano, and T. Shimomura, “Changes in the electrical resistivity of the central cone, Miharayama, of Oshima Volcano observed by a direct current method,” *Journal of Geomagnetism & Geoelectricity*, vol. 42, no. 3, pp. 151–169, 1990.
- [7] T. Mao, T. Wang, J. Yao, J. Lu, and H. Zhang, “The variations of the degree of ground resistivity anisotropy during the tangshan earthquake,” *Acta Seismologica Sinica*, vol. 8, no. 4, pp. 621–627, 1995.
- [8] T. Mao, G. Xu, S. Fan, M. Zhao, and J. Sun, “Dynamic evolution patterns of the degree of ground resistivity anisotropy and the seismogenic process,” *Acta Seismologica Sinica*, vol. 12, no. 2, pp. 199–206, 1999.
- [9] R. Feng, J. Hao, and J. Zhou, “Resistivity tomography in earthquake monitoring,” *Chinese Journal of Geophysics*, vol. 44, no. 6, pp. 819–830, 2001.
- [10] Z. Feng, J. Yang, W. Mei, J. Geng, X. Wang, and Y. Liu, “Preliminary study on characteristics of seismic precursor of earth resistivity anisotropy degree in east China,” *Acta Seismologica Sinica*, vol. 17, no. 2, pp. 244–250, 2004.
- [11] H. Utada, “Interpretation of time changes in the apparent resistivity observed prior to the 1986 eruption of Izu-Oshima volcano, Japan,” *Journal of Volcanology and Geothermal Research*, vol. 126, no. 1-2, pp. 97–107, 2003.
- [12] J. An, P. Zhou, M. Ma, F. Chen, Y. Dong, and P. Zhong, “Experiments on exploring and monitoring landslip-mass using geoelectric resistivity observations,” *Acta Seismologica Sinica*, vol. 21, no. 3, pp. 258–266, 2008.
- [13] W. F. Brace, A. S. Orange, and T. M. Madden, “The effect of pressure on the electrical resistivity of water-saturated crystalline rocks,” *Journal of Geophysical Research*, vol. 70, no. 22, pp. 5669–5678, 1965.
- [14] W. F. Brace and A. S. Orange, “Electrical resistivity changes in saturated rock under stress,” *Science*, vol. 153, no. 3743, pp. 1525–1526, 1966.
- [15] W. F. Brace and A. S. Orange, “Electrical resistivity changes in saturated rocks during fracture and frictional sliding,” *Journal of Geophysical Research*, vol. 73, no. 4, pp. 1433–1444, 1968.
- [16] W. F. Brace and A. S. Orange, “Further studies of the effects of pressure on electrical resistivity of rocks,” *Journal of Geophysical Research*, vol. 73, no. 16, pp. 5407–5420, 1968.
- [17] C. Y. Wang, R. E. Goodman, P. N. Sundaram, and H. F. Morrison, “Electrical resistivity of granite in frictional sliding: application to earthquake prediction,” *Geophysical Research Letters*, vol. 2, no. 12, pp. 525–528, 1975.
- [18] K. Kondo, T. Mashimo, and A. Sawaoka, “Electrical resistivity and phase transformation of hematite under shock compression,” *Journal of Geophysical Research*, vol. 85, no. 2, pp. 977–982, 1980.
- [19] C. Morrow and W. F. Brace, “Electrical resistivity changes in tuffs due to stress,” *Journal of Geophysical Research*, vol. 86, no. 4, pp. 2929–2934, 1981.
- [20] C. Pearson, J. Murphy, and R. Hermes, “Acoustic and resistivity measurements on rock samples containing tetrahydrofuran hydrates: laboratory analogues to natural gas hydrate deposits,” *Journal of Geophysical Research*, vol. 91, no. 14, pp. 14132–14138, 1986.
- [21] K. Skagius and I. Neretnieks, “Diffusivity measurements and electrical resistivity measurements in rock samples under mechanical stress,” *Water Resources Research*, vol. 22, no. 4, pp. 570–580, 1986.
- [22] F. Chen, J. Xiu, J. An, C. Liao, and D. Chen, “Detecting rupture precursors and determining the main fracture spread direction of rock with dynamic rock resistivity change anisotropy,” *Acta Seismologica Sinica*, vol. 13, no. 2, pp. 234–237, 2000.
- [23] F. Chen, J. Xiu, J. An, C. Liao, and D. Chen, “Research on dependence of resistivity changing anisotropy on microcracks extending in rock with experiment,” *Acta Seismologica Sinica*, vol. 13, no. 3, pp. 331–341, 2000.
- [24] F. Chen, C. Liao, and J. An, “Directional characteristic of resistivity changes in rock of original resistivity anisotropy,” *Chinese Journal of Geophysics*, vol. 46, no. 2, pp. 381–395, 2003.
- [25] F. Chen, C. Liao, and J. An, “Amplitude and anisotropy of apparent resistivity change in big models during shear and frictional slipping,” *Chinese Journal of Geophysics*, vol. 46, no. 5, pp. 954–965, 2003.
- [26] D. Fitterman, “Theoretical resistivity variations along stressed strike-slip faults,” *Journal of Geophysical Research*, vol. 81, no. 26, pp. 4909–4915, 1976.
- [27] D. L. Johnson and H. J. Manning, “Theory of pressure dependent resistivity in crystalline rocks,” *Journal of Geophysical Research*, vol. 91, no. 11, pp. 11611–11617, 1986.
- [28] K. Teisseire, “Anisotropy of electric resistivity related to crack process before fracturing,” *Acta Geophysica Polonica*, vol. 37, no. 2, pp. 185–192, 1989.
- [29] K. Teisseire, “Simulation of anisotropic changes of resistivity in primarily anisotropic rocks under load,” *Acta Geophysica Polonica*, vol. 41, no. 3, pp. 316–333, 1991.
- [30] K. Teisseire, “Modeling of crack induced resistivity changes—applications to earthquake studies,” *Publications Institute of Geophysics, Polish Academy of Sciences, Series A*, vol. 24, no. 274, pp. 1–63, 1997.
- [31] Y. Yamazaki, “Electrical conductivity of strained rocks, 1, Laboratory experiments on sedimentary rocks,” *Bulletin of the Earthquake Research Institute, University of Tokyo*, vol. 43, p. 783, 1965.
- [32] Y. Yamazaki, “Electrical conductivity of strained rocks, 2, Further experiments on sedimentary rocks,” *Bulletin of the Earthquake Research Institute, University of Tokyo*, vol. 44, p. 1553, 1966.
- [33] D. Chen, F. Chen, and L. Wang, “Studies on resistivity of rock samples under uniaxial pressure-anisotropy of resistivity,” *Acta Geophysica Sinica*, vol. 26, pp. 784–792, 1983 (Chinese).
- [34] J. An, J. Xiu, F. Chen, and D. Chen, “Anisotropy studies of rock resistivity changes under uniaxial pressure and water replenishment,” *Earthquake Research in China*, vol. 12, no. 3, pp. 300–306, 1996 (Chinese).
- [35] I. Diaferia, M. Barchi, M. Loddo, D. Schiavone, and A. Siniscalchi, “Detailed imaging of tectonic structures by multiscale Earth resistivity tomographies: the Colfiorito normal faults (central Italy),” *Geophysical Research Letters*, vol. 33, no. 9, Article ID L09305, 2006.
- [36] A. Roy and A. Apparao, “Depth of investigation in direct current methods,” *Geophysics*, vol. 36, no. 5, pp. 943–957, 1971.
- [37] L. S. Edwards, “A modified pseudosection for resistivity and IP,” *Geophysics*, vol. 42, no. 5, pp. 1020–1036, 1977.
- [38] F. Qian, Y. Zhao, and Y. Huang, “Calculation of the parameters of georesistivity anisotropy and case history of earthquake precursors,” *Acta Seismologica Sinica*, vol. 9, no. 4, pp. 617–627, 1999.